Techniques and Applications in Rapid Spiral Magnetic Resonance Imaging

---

A

Dissertation

Presented to

the faculty of the School of Engineering and Applied Science

University of Virginia

---

in partial fulfillment

of the requirements for the degree

Doctor of Philosophy

by

Zhixing Wang

May 2023

APPROVAL SHEET

This

Dissertation

is submitted in partial fulfillment of the requirements
for the degree of

Doctor of Philosophy

Author: Zhixing Wang

This Dissertation has been read and approved by the examing committee:

Advisor: Craig H. Meyer

Advisor:

Committee Member: John P. Mugler III

Committee Member: Christopher M. Kramer

Committee Member: Frederick H. Epstein

Committee Member: Adrienne E. Campbell-Washburn

Committee Member:

Committee Member:

Accepted for the School of Engineering and Applied Science:

Jennifer L. West, School of Engineering and Applied Science

May 2023

Abstract

Magnetic Resonance Imaging (MRI) is a valuable tool for medical diagnosis, because of the excellent soft tissue contrast and the absence of ionizing radiation. However, MRI is a slow imaging modality. For areas of the body that can be immobilized (e.g., brain), a total examination time of 30 ~ 60 minutes will be performed, which largely reduces patient comfort and cooperation. For areas of the body subject to physiological motion (e.g., breathing motion), any involuntary movements during a scan will degrade the image quality. Thus, a major challenge for MRI is to reduce the long scan time while obtaining images with clinically acceptable quality.

Rapid MRI involves a rich collection of techniques that improve the speed of MRI data acquisition (e.g., non-Cartesian trajectories, parallel imaging). Speed improvements are desirable in many clinical applications. This dissertation will cover two applications: T_2-weighted imaging and imaging of cardiac function. The overall goal of this dissertation is to provide rapid data acquisition approaches using spiral k-space trajectories with advanced image reconstruction methods, as well as strategies for compensation of system imperfections (e.g., B_0 inhomogeneity).

A new approach to 2D turbo spin-echo imaging using annular spiral rings with a retraced in/out trajectory, dubbed “SPRING-RIO TSE”, was developed for fast T_2-weighted brain imaging at 3T. A detailed procedure of spiral rings implementation was presented, as well as effective correction methods for gradient infidelity and B_0 inhomogeneity. Volunteer data showed that the proposed method achieves high-quality 2D T_2-weighted brain imaging with a higher scan efficiency (0:45 min/14 slices versus 1:31 min/14 slices), improved image contrast, and reduced specific absorption rate (SAR) (~ 86% reduction) compared to conventional 2D Cartesian TSE.

For scanning at 0.55 T and 1.5 T, strategies of sequence modifications were implemented

in SPRING-RIO TSE for compensation of concomitant gradient terms at the echo time and across echo spacings, along with reconstruction-based corrections to simultaneously compensate for the residual concomitant- and B_0-field induced phase accruals along the readout. Volunteer data showed that after full correction, SPRING-RIO TSE achieves high image quality with improved SNR efficiency (15% ~ 20% increase) and reduced RF SAR (~ 50% reduction) compared to standard Cartesian TSE, presenting potential benefits, especially in regaining SNR at low-field. The compensation principles can be extended to correct for other trajectory types that are time-varying and asymmetric along the echo train in TSE-based imaging.

A 3D spiral-in/out SPACE pulse sequence that incorporates variable-flip-angle refocusing RF pulses with an echo-reordering strategy, concomitant gradient compensation, and variable-density undersampling, was proposed for 1 mm^3 isotropic whole brain T_2-weighted imaging at 0.55 T. Volunteer data showed increased apparent SNR values when using spiral SPACE over Cartesian SPACE (17.1$\pm$2.3% gain) for similar scan times, providing a potential to mitigate the intrinsic lower SNR of 0.55 T via the improved SNR efficiency of prolonged spiral sampling.

In cardiac imaging, both spiral-out and -in/out bSSFP pulse sequences were developed for accelerated ungated, free-breathing real-time cine at 1.5 T. Volunteer data showed that the two spiral cine techniques showed clinically diagnostic images (score > 3). Compared to standard cine, there were significant differences in global image quality and edge sharpness for spiral techniques, while there was significant difference in image contrast for the spiral-out cine but no significant difference for the spiral-in/out cine. There was good agreement in left ventricular ejection fraction for both the spiral-out cine (-1.6$\pm$3.1%) and spiral-in/out cine (-1.5$\pm$2.8%) against standard cine.

We demonstrated all proposed techniques lead to improved sampling efficiency and scan comfort, and provide promising alternatives to standard Cartesian acquisition counterparts.

Acknowledgement

I leave this part as the last step towards completion, because it helps evoke great memories of my last five years studying at the University of Virginia. Looking back, I realized more than any time that this dissertation could not have been done without the support and encouragement of those around me.

Of course, I owe my deepest gratitude to my advisor, Dr. Craig Meyer, for accepting me as a student and supervising me through the Ph.D. program. I still remember the day when I first met him in person during the ISMRM meeting in Singapore, 2016, though he might not (most likely did not) know me at that time. Craig is the kindest person I have ever met. He has generously given me the freedom to pursue my research directions, as well as the means to guide me how to "fish". I know he is very busy, but he always has the patience to answer all my questions in many aspects from research to skiing, though I am a snowboarder. His enthusiasm in research and humility is truly inspiring. I feel very lucky to have such a nice person in my life.

I have been fortunate to have had the great honor to work closely with Dr. John Mugler, who has been kindly serving as my committee chair since my oral qualifying exam. John is the expert on most of the content of this dissertation, and his rich knowledge about MR physics and enthusiasm on technique development has strongly influenced my research as well as my attitude towards research. Having discussions with him is always enjoyable, though he looks very serious; indeed, he is very serious about every technical detail. I thank John for his encouragement, sense of dry humor, and also for being a great role model.

I would also like to thank my other advisory committee members, Drs. Christopher Kramer, Frederick Epstein, Adrienne Campbell, for helping shape the dissertation project. Special thanks

to Dr. Adrienne Campbell for granting me a precious opportunity to conduct research at NHLBI, NIH this summer, and for always being interested in my work. It is super joyful to explore the "SPACE" with her together, though the three-month intern is short. I must also thank Dr. Michael Salerno for serving as the committee in my candidacy exam and for his help in guiding the clinical partition of this work.

I am extremely grateful to my former advisors, Drs. Yiping Du and Jianhui Zhong, during my master study at Zhejiang University. They were the first ones who introduced me to the principles of MRI, and it was at that point I started to cultivate a strong interest in MR physics.

My appreciation also goes to my colleagues at the University of Virginia. Many thanks go to Drs. Xue Feng and Steven Allen in Meyer lab, for all of their countless support, valuable discussion, and help getting me up. I would also like to acknowledge the older generation of graduate students, Drs. Yang Yang, Ruixi Zhou in Salerno lab, Drs. Changyu Sun, Xiaoying Cai, Mohammad Abdishektaei in Epstein lab, and Dr. Kun Qing in Mugler lab, for setting a fine example for us. I am also deeply grateful to have my fellow graduate students, Helen Sporkin, Yekaterina Gilbo, Quan Dou, Samarth Singh, Yanjun Xie, Sheng Chen, Kang Yan, and Yu Wang, to be an essential part of my life at UVA. In particular, I want to thank a close friend, Dr. Junyu Wang, who left UVA, went to Stanford, and mercilessly ended our roommate-ship much earlier than expected, for promising me to be present online on my defense day even at his 2 AM local time in China, though he did not make it.

Outside of UVA, I would like to express my gratitude to Drs. Rajiv Ramasawmy and Ahsan Javed for their invaluable support in helping develop my project at NIH, as well as for taking time to show me around the campus and city of Bethesda. Specifically, from Rajiv, I learnt that bringing a donut to the scanner and making it happy is necessary for not being crushed.

Many new and old friends, notably Xiaozhi Cao, Mingliang Chen, Yajun Shi, Liangyun Zhang, Lantao Liu, Pan Qian, Nan Yang, Jack Whitewolf, and Zhixiong Wang, made life more fulfilling outside of the lab during this Ph.D. journey. I thank you all so much for the constant reminder of where my home is. I am also deeply grateful to William Zierden, Abigail Duff, and Rosie Tomiak for being my language buddies in Charlottesville, as they made me feel like Virginia is my second home.

I would like to express my special appreciation to Miss Tiantian Xu, who has been an essential part of my life and has accompanied me in every precious moment since college. I thank her for her support, encouragement, and the passion for life that inspired me in many aspects of my own life.

Most importantly, I could not have done any of this without the unconditional love from my family, my mom Minming He, dad Tuanjiang Wang. My parents have been extremely supportive of my decisions all the time, and to them I dedicate this dissertation.

I would like to end with a quote from Jack Kerouac's book *The Dharm Bums* – 'O ever youthful, O ever weeping'. I miss you - UVA, Charlottesville, and Virginia!

University of Virginia ZHIXING WANG

December 2022

Table of Contents

List of Figures

List of Tables

Chapter 1: Introduction

1.1 Significance

It has been more than forty years since the first human Magnetic Resonance Imaging (MRI) scanner was created, and now MRI is becoming a powerful and valuable imaging tool for medical diagnosis, because it offers excellent and multiple soft tissue contrast by changing the imaging protocols flexibly and does not use ionizing radiation in contrast to other widely used imaging techniques, such as X-ray or computerized tomography (CT).

According to the official datasets released from the National Health Service, England, however, the total usage of MRI in clinical practice is still much lower than other imaging modalities.[1] Figure 1-1 shows that within the total imaging activities in England from July 2021 to July 2022, X-ray has the highest number of procedures (on average 1.7 million) per month, followed by ultrasound which has 0.8 million procedures, and MRI has the lowest imaging tests of 0.3 million. The long total scan time per procedure is one of the major reasons, which ranges from thirty minutes to two hours for a complete MRI test. The high examination cost per hour is another concern for the more widespread use of MRI, due to its intrinsic expensive machine cost and the related high maintenance burden.

Furthermore, there are several drawbacks when the imaging speed of a conventional clinical MRI practice is slow. Two scenarios are described as follows:

1. Scanning parts of the body that are immobilized (e.g., brain, knee) may take several minutes for a typical T_1-weighted (T_1w) or T_2-weighted (T_2W) examination, resulting in a total examination time of 30 ~ 60 min for only one part of the body, which makes

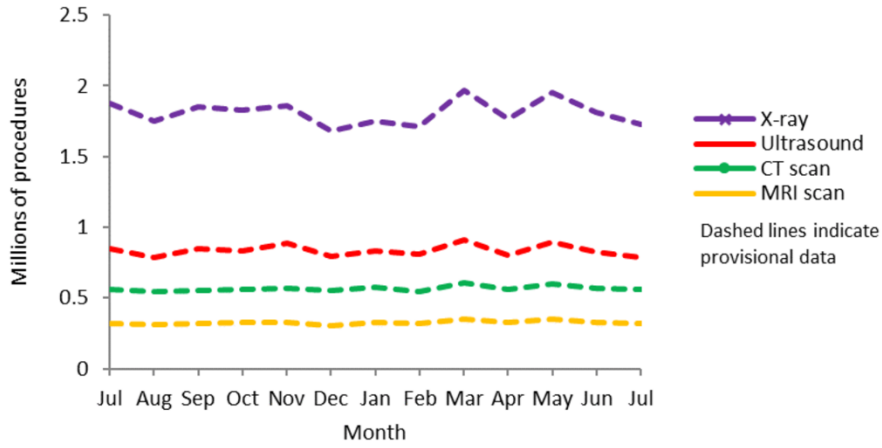

Figure 1-1. NHS imaging activities in England from July 2021 to July 2022.

the procedure especially hard for children and patients who experience a claustrophobic reaction during the scan.

2. Scanning parts of the body that are subject to physiological motion (e.g., breathing motion, cardiac motion) presents more challenges, since any involuntary movements during a scan will degrade the image quality, resulting in additional requirements such as electrocardiogram (ECG) gating and/or several breath-holds, which largely reduce patient comfort and cooperation.

In conclusion, there is a strong demand to develop rapid MRI techniques that speed up MR scanning while maintaining clinically acceptable image quality, such as techniques that involve rapid pulse sequence development (e.g., non-Cartesian imaging[2-3], simultaneous multi-slice[4]), advanced image reconstruction (e.g., parallel imaging[5-6], compressed sensing[7]), and deep learning approaches (e.g., Noise2Noise[8]).

1.2 Specific aims

This dissertation work addresses three specific aims, and these aims cover both methodological analysis and experimental implementations of phantom and in vivo studies. The

main objectives of this dissertation will focus on developing turbo-spin-echo (TSE) sequences for fast T_2-weighted neuroimaging and balanced steady-state free precession (bSSFP) sequences for real-time cardiac imaging, as well as exploiting strategies for compensation of system imperfections, such as B_0 inhomogeneities and concomitant gradients.

Specific Aim 1 is to design and implement both 2D and 3D TSE imaging using spiral trajectories with improved SNR/scan efficiency, as alternatives to Cartesian counterparts for rapid T_2-weighted imaging. This aim includes the following: 1a: Introduce the k-space sampling strategy of annular rings with retraced in/out (RIO) segments into a 2D TSE signal model. 1b: Design 3D variable-flip-angle TSE with spiral-in/out readouts and echo-reordering.

Specific Aim 2 is to develop correction methods in spiral imaging for system imperfections. This aim includes the following: 2a: Describe approaches to correct for k-space trajectory infidelity and B_0 inhomogeneity effects. 2b: Introduce strategies of compensation for concomitant gradients over echo spacings and during the readouts via gradient waveform modifications and image reconstruction.

Specific Aim 3 is to implement real-time cardiac MRI using accelerated spiral-based bSSFP sequences under ungated, free-breathing condition. This aim includes the following: 3a: Design and optimize spiral-out and spiral-in/out bSSFP sequences for real-time imaging. 3b: Implement reconstruction methods and compare the performance in highly accelerated cardiac MRI.

1.3 Dissertation outline

The remainder of this dissertation is organized as follows:

Chapter 2 gives a brief introduction to the background knowledge that is relevant to this dissertation. It first covers T_2-weighted imaging and cardiac cine imaging used in routine clinical practice. Second, an overview of techniques in rapid MRI acquisitions, including spiral k-space scanning, turbo-spin-echo imaging, and balanced steady-state free precession imaging, will be given. This is then followed by details regarding system imperfections such as gradient infidelity, B_0 inhomogeneity, and concomitant gradients. Finally, opportunities and challenges in low-field systems will be described.

Chapter 3 introduces 2D TSE imaging using annular spiral rings with a retraced in/out trajectory (abbreviated "SPRING-RIO TSE") for rapid T_2-weighted imaging at 3 T, which includes the k-space sampling strategy of annular rings with retraced in/out (RIO) segments, methods for correcting for k-space trajectory infidelity and B_0 inhomogeneity effects, and validation in simulations, phantom and in vivo scans.

The sequence developed in Chapter 3 suffers from concomitant field effects at lower main field strengths. Chapter 4 develop strategies for concomitant field compensation for SPRING-RIO TSE imaging at 0.55 T and 1.5 T, which includes strategies of gradient waveform modifications for compensating the Maxwell gradient effects at the echo time and over echo spacings, image reconstruction-based compensation to correct for residual phase errors along the readout, and validation in simulations, phantom and in vivo scans.

Chapter 5 covers variable-flip-angle 3D spiral-in/out TSE imaging using echo-reordering and concomitant gradient compensation at 0.55 T, which includes pulse sequence design of variable-flip-angle generation and concomitant gradient compensation, image reconstruction to correct for system imperfections, and validation in phantom and in vivo scans.

Chapter 6 is focused on developing high spatiotemporal real-time cardiac MRI using accelerated spiral bSSFP sequences at 1.5 T, which includes the implementation of two optimized spiral-based bSSFP sequences along with three reconstruction methods (view-sharing, compressed sensing, and low-rank plus sparse), and validation in simulations and in vivo scans with whole heart coverage short-axis views.

Chapter 7 summarizes the contributions of this dissertation and provides an outlook for future work.

1.4 References

1. England, N.H.S. and Improvement, N.H.S., 2022. Diagnostic imaging dataset statistical release.
2. Pipe JG. Motion correction with PROPELLER MRI: application to head motion and free-breathing cardiac imaging. *Magn Reson Med*. 1999; 42:963-969.
3. Meyer CH, Hu BS, Nishimura DG, Macovski A. Fast spiral coronary artery imaging. *Magn Reson Med*. 1992; 28:202-213.
4. Barth M, Breuer F, Koopmans PJ, et al. Simultaneous Multislice (SMS) imaging techniques. *Magn Reson Med*. 2016; 75:63-81.
5. Pruessmann KP, Weiger M, Scheidegger MB, Boesiger P. SENSE: Sensitivity encoding for fast MRI. *Magn Reson Med*. 1999;42:952–962.
6. Griswold MA, Jakob PM, Heidemann RM, Nittka M, Jellus V, Wang J, Kiefer B, Haase A. Generalized auto-calibrating partially parallel acquisitions (GRAPPA). *Magn Reson Med*. 2002;47:1202–1210.
7. Lustig M, Donoho D, Pauly JM. Sparse MRI: The application of compressed sensing for rapid MR imaging. *Magn Reson Med*. 2007;58: 1182–1195.
8. Kang S, Yie S, Lee J. Noise2Noise: Improved by Trainable Wavelet Coefficients for PET Denoising. *Electronics*. 2021; 10(13):1529.

Chapter 2: Background

2.1 Basic imaging

2.1.1 T_2-weighted imaging

T_2W imaging is one of the basic pulse sequences for clinical MRI practice. The sequence weighting highlights differences in the T_2 relaxation time of tissues (also known as "spin-spin" relaxation).[1] Each tissue has an inherent T_2 value, yet external factors (e.g., B_0 inhomogeneity) can decrease the T_2 relaxation time which results in T_2^* weighting. Thus, spin-echo based imaging, the standard method that acquires images with T_2 weighting instead of T_2^* weighting, uses refocusing pulses to help mitigate the extraneous influences on the T_2 relaxation time. These types of sequences normally have protocols with a long TR as well as a long TE.

2.1.2 Cardiac cine imaging

Cardiac magnetic resonance (CMR), which acquires a series of MR images to capture evolving cardiac phenomena, is becoming more popular in clinical practice for assessment of heart diseases.[2] One application of CMR is cardiac cine imaging, which often acquires images during a breath-hold using ECG-gated bSSFP pulse sequences with segmented Cartesian readouts.[3] Figure 2-1 shows the routine procedure of how standard Cartesian cine techniques produce images with high spatiotemporal resolution and good image quality by filling k-space line-by-line. Cardiac function can then be assessed qualitatively and quantitatively (e.g., left ventricular ejection fraction) by analyzing the motion of the ventricular walls during systole and diastole. Another promising cine technique that does not require ECG gating and breath-holding is using real-time snapshot imaging, but it may suffer from low spatial and/or temporal resolution.

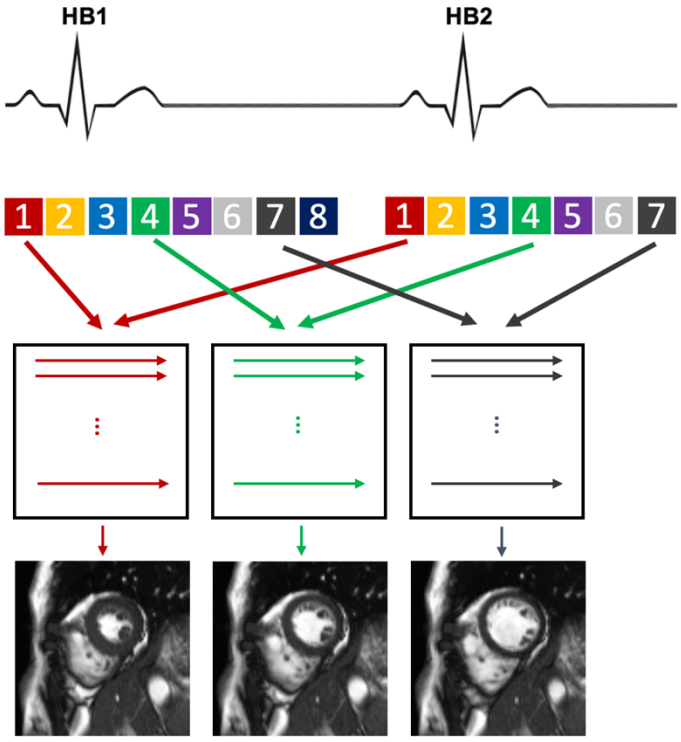

Figure 2-1. Standard cine imaging with segmented Cartesian readouts, ECG-triggering, and retrospective binning.

2.2 Rapid acquisitions

2.2.1 Spiral imaging

MRI signals are not acquired directly in the image domain but in spatial frequency space (also known as k-space). A conventional Cartesian trajectory fills k-space line by line in each excitation, providing robustness to system imperfections but with relatively low scan efficiency, because RF pulses and pre/post-encoding gradients occupy a certain amount of time and thus the ratio of signal acquisition to the total imaging time is small. Spiral scanning, one type of acquisitions that use non-Cartesian trajectories, acquires more data points per excitation and has been widely used in fast imaging due to its high scan efficiency.[4] Figure 2-2 shows one example of conventional spiral-out gradient waveforms and its corresponding trajectory, of which the trajectory starts from the beginning and keeps turning in k-space while sampling areas farther away from the origin (black

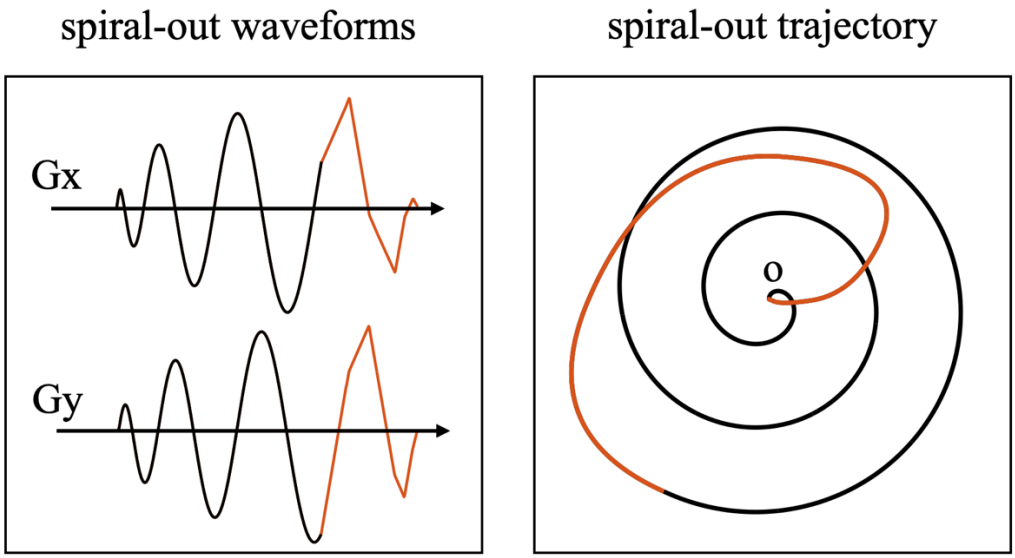

Figure 2-2. One example of spiral-out gradient waveforms and the corresponding trajectory.

line), followed by a rewinder (red line) that brings it back to the origin. In addition to being fast, spiral imaging offers other desirable properties (e.g., insensitivity to motion-related artifacts), but it may also present several challenges for compensating system imperfections, such as gradient infidelity, B_0 inhomogeneities, and concomitant fields, resulting in image blurring and signal loss. The next sections will cover these effects in more detail.

2.2.2 Turbo-spin-echo imaging

The advent of fast sequences based on turbo-spin-echo (TSE)[5,6] acquisitions enabled T_2-weighted imaging to be performed in a clinically feasible scan time, and these sequences have become the workhorse for spin-echo-based imaging. The Cartesian TSE sequence is one of the standard methods for fast T_2-weighted imaging, where multiple lines are sampled per excitation, as shown in Figure 2-3. Compared to the conventional single-echo spin-echo imaging, the total scan time can be reduced by the number of echoes acquired in one excitation, which is also known as the echo train length (ETL). Other image contrast can be achieved by adding a magnetization-prepared

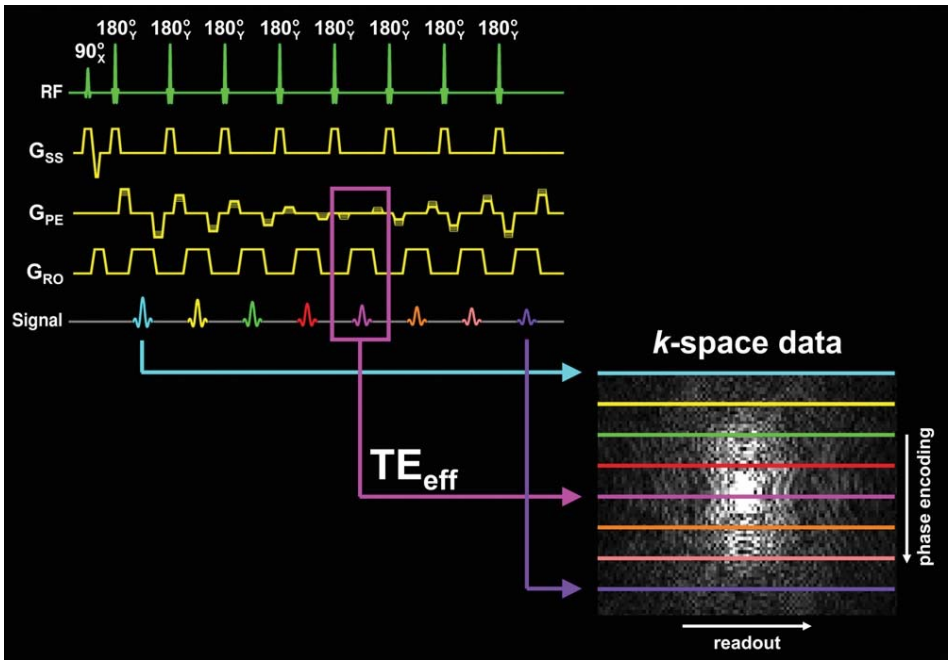

Figure 2-3. The timing diagram for 2D TSE imaging. (Adapted from Ref.6, Fig.1).

module before the TSE acquisition window. For example, an inversion recovery pulse can be placed at the beginning, and by adjusting the inversion time (TI) between the inversion recovery pulse and the first excitation pulse of the TSE part, fluid-attenuated T_2-weighted images[7] can be generated. Figure 2-4 shows examples of images with different weightings acquired from TSE-based imaging.[8]

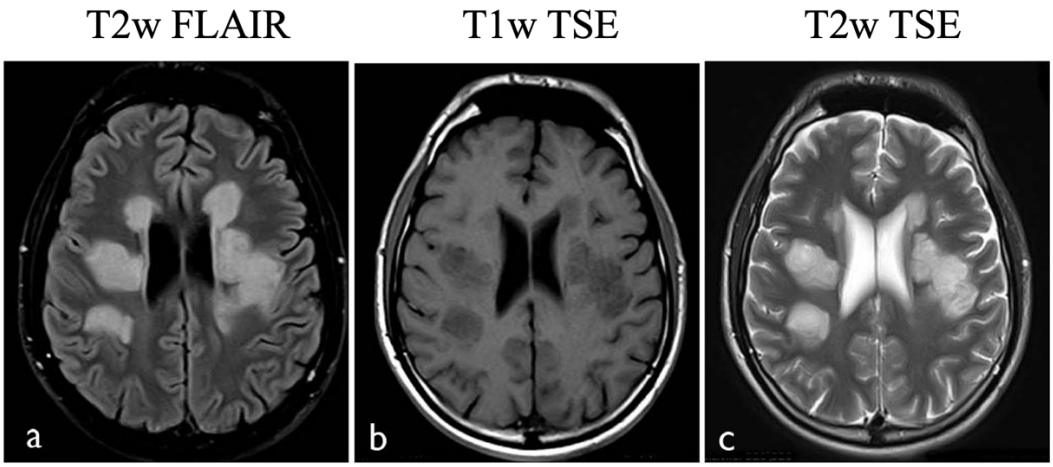

Figure 2-4. Examples of T_2W FLAIR, T_1W and T_2W brain images using TSE acquisition. (Adapted from Ref.8, Fig.1).

2.2.3 Balanced steady-state free precession imaging

Steady-state free precession (SSFP) sequences show great potential in fast imaging because of the short repetition time which allows for very high scan efficiency. In addition, balanced SSFP imaging, one member of the SSFP family tree, has demonstrated unique capability in cardiac MRI due to its flow insensitivity and excellent image contrast between the blood pool and myocardium[9], as can be seen in Figure 2-5 showing the comparison of cardiac images from the spoiled gradient-echo (left) and bSSFP sequences (right).

Figure 2-6 shows a simplified sequence diagram, which involves a dummy cycle to reach the steady-state, followed by continuous data acquisition. The directions of RF series are alternating between -x and x, and the flip angle of the first excitation RF pulse equals half of the following RFs. A major challenge with bSSFP imaging is banding artifacts induced by the spatially dependent off-resonance effects (e.g., B_0 field inhomogeneity). This problem can be alleviated but may not be completely corrected via good shimming and/or using a short TR.

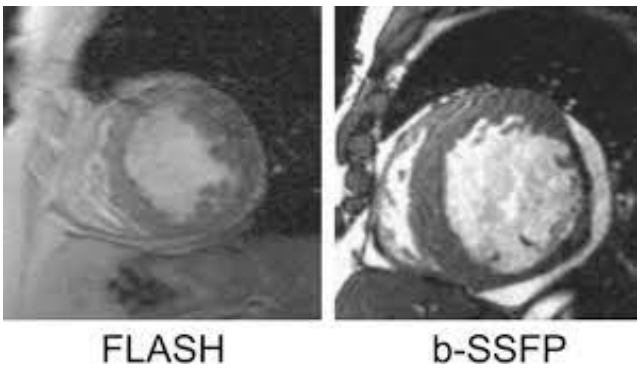

Figure 2-5. Comparison of cardiac images from the spoiled gradient-echo (left) and bSSFP sequences (right). (Adapted from Ref. 9, Figure 12).

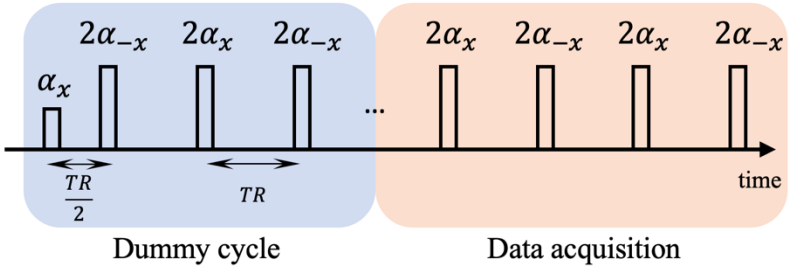

Figure 2-6. Timing diagram of the bSSFP sequence.

2.3 System imperfections

2.3.1 Gradient infidelity

Non-Cartesian trajectories rely strongly on the gradient fidelity, and any deviation of the actual k-space trajectory from the nominal trajectory may be detrimental to image quality, in terms of image blurring, distortion, and edge artifacts. In reality, the gradient response of the gradient systems may vary, resulting in the anisotropic delay of three main axes (x, y, z). In addition, any time-varying gradient fields from the encoding gradients will induce inevitable eddy currents that may distort the trajectory and thus degrade the image. One simple way to resolve this problem is to measure the actual trajectory given one specific imaging orientation and the current set of sequence protocols using Duyn's method[10], as can be seen in Figure 2-7, where two symmetric off-center thin slices are excited for each physical axis that contributes the trajectory. The calibration can be performed in a phantom, but this method is impractical, because any change in trajectory generation will need to be recalibrated and is very time-consuming, normally taking 30 ~ 60 mins. Therefore, researchers have developed several methods to estimate and predict the actual trajectory. This section will briefly describe the basics of two widely used trajectory correction methods.

The first method, a model-based trajectory estimation named the Tan-Meyer method[11], can be expressed as:

$$\widetilde{\boldsymbol{k}}(t) = \int_0^t s(\tau) \otimes H(\tau)\, d\tau \approx A \int_0^t G_d(\tau) d\tau + B \int_0^t K_d(\tau) d\tau, \qquad (2\text{-}1)$$

where $\widetilde{\boldsymbol{k}}(t)$ is the estimated k-space trajectory, $s(\tau)$ is the slew rate, $H(\tau)$ is the impulse response function. $\boldsymbol{G_d}$ is the gradient waveform, and $\boldsymbol{K_d}$ is the k-space trajectory on one physical axis with a gradient delay. *A* and *B* are constant values based on the gradient system of the scanner and are independent of the image orientation and sequence parameters. Thus, any arbitrary trajectory can

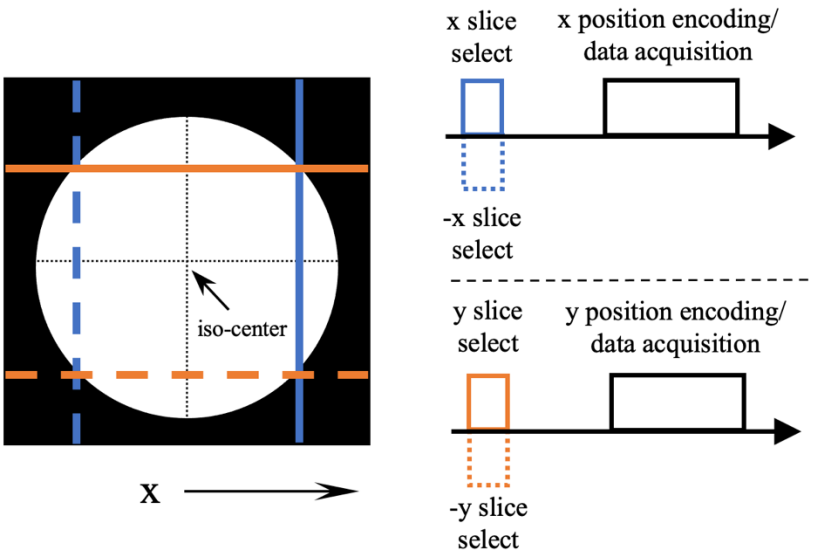

Figure 2-7. Schematic diagram of the protocol for measurement of actual k-space trajectories.

be estimated once we obtain parameters *A* and *B* from a separate calibration in a phantom scan. The calibration involves the actual trajectory ($\boldsymbol{K_a}$) acquisition, followed by the delay model ($\boldsymbol{K_d}$) estimation via 2D search for minimum root mean square error (RMSE) between the bench images from theoretical trajectories with different delays and the goal images from the actual trajectories, and a final step of the eddy current model $\boldsymbol{K_e}$ estimation through least square fit from the residual error ($\boldsymbol{K_a} - \boldsymbol{K_d}$).

Another trajectory correction method is using the gradient impulse response function (GIRF), which is under the assumption of a linear and time-invariant gradient system.[12] The actual gradient waveforms considering all the system imperfections can be predicted via the convolution of the theoretical gradient waveforms with the GIRF, as the equation shown below:

$$o(t) = \int_{-\infty}^{+\infty} i(\tau)\, h(t-\tau) d\tau \overset{FT}{\leftrightarrow} O(\omega) = I(\omega) \cdot H(\omega), \qquad (2\text{-}2)$$

where i, o, h are the time domain input, output, and gradient impulse response, and I, H, O are the corresponding Fourier transforms, respectively. The gradient transfer function $H(\omega)$ can be measured via one-time calibration in a phantom experiment. This can be done by generating a

series of triangular gradients and measuring their actual waveforms, followed by the calculation shown below:

$$H(\omega) = \frac{\sum_j I_j^*(\omega) \cdot O_j(\omega)}{\sum_j |I_j(\omega)|^2 + \sigma}, \tag{2-3}$$

where j is the jth triangle, and σ is a measure of the noise level.

2.3.2 B_0 field inhomogeneities

B_0 field inhomogeneity is one main source that contributes to off-resonance effects. Figure 2-8 shows examples of blurred brain images from spiral TSE at 3 T. The signal equation that incorporates local field inhomogeneities can be expressed as:

$$s(t) = \int m(r) e^{-j2\pi k(t) r} e^{-j\Delta\omega(r) t}\, dr, \tag{2-4}$$

where $\Delta\omega(r)$ is the local off-resonance frequency from B_0 field inhomogeneities. Various methods have been developed to correct for this issue, including but not limited to conjugate phase reconstruction (CPR)[13-19], iterative image reconstruction[20-21], and deep learning-based methods[22]. In this section, we will focus on CPR correction, a common approach for image reconstruction in non-Cartesian MRI which does not require iterations or prior knowledge of training data. The reconstruction can be expressed as follows:

$$m(r) = \int s(t) W(t) e^{j2\pi k(t) r} e^{j\Delta\omega(r) t}\, dt, \tag{2-5}$$

where W(t) is the density compensation function.

There have been many different techniques proposed based on CPR deblurring methods, and most of these methods are based on knowledge of an accurate field map, which can be derived from an additional 2-TE gradient recalled echo scan[13-15] or can be estimated directly or partially from the image itself using the techniques termed "automatic[16,17]" or "semiautomatic

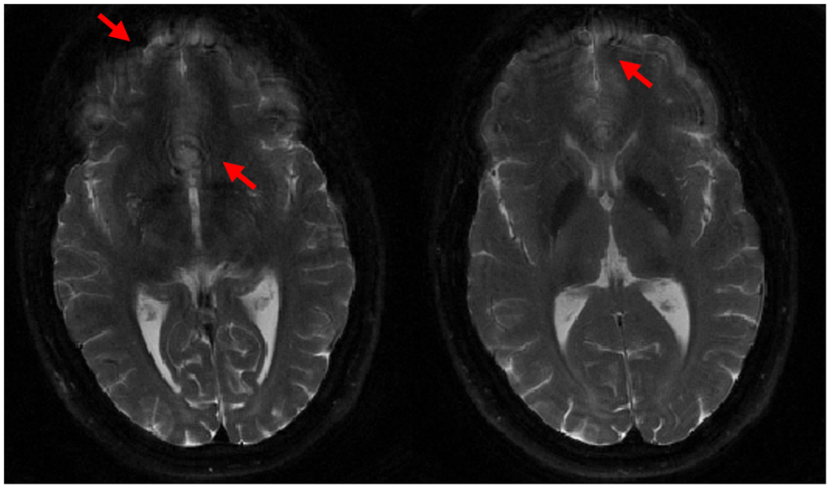

Figure 2-8. Blurred images from spiral TSE at 3 T due to B_0 inhomogeneity effects.

deblurring[18,19]" by enforcing the constraint to the objective function. In addition, in order to accelerate the reconstruction process, fast CPR methods that are based on either time- or frequency- approximation have been developed. For example, multifrequency interpolation reconstruction (MFI)[15], one of the frequency approximation methods, reconstructs images at a few demodulation frequencies and combines them through a linear combination of the component images with the interpolation coefficients $c_i(\Delta\omega)$ derived from the following equation below:

$$e^{j\Delta\omega t} \approx \sum_{i=0}^{L} c_i(\Delta\omega) e^{j\Delta\omega_i t}, \tag{2-6}$$

where $\Delta\omega_i$ is ith quantized demodulation frequency, L is the total number of frequency segments.

However, the main challenge of CPR deblurring is that it may become less effective in some regions where the local inhomogeneity changes rapidly (e.g., air-tissue boundaries), because it violates the assumption that the main field off-resonance frequency varies slowly in space. In this case, other correction methods (e.g., iterative reconstruction) that do not rely on this condition have demonstrated better performance over CPR methods.

2.3.3 Concomitant gradient fields

Concomitant fields, also known as Maxwell fields, created simultaneously with spatially varying gradient fields, are another important source of off-resonance effects.[23,24] The presence of concomitant magnetic fields causes undesired phase accumulation that may contaminate the measured k-space data, thus resulting in artifacts in MR imaging. The mathematical description of Maxwell fields B_c can be estimated based on the following equation, omitting the third and higher order terms,

$$B_c(g_x, g_y, g_z, x, y, z) = \left(\frac{g_z^2}{8B_0}\right)(x^2 + y^2) + \left(\frac{g_x^2+g_y^2}{2B_0}\right)z^2 - \left(\frac{g_x g_z}{2B_0}\right)xz - \left(\frac{g_y g_z}{2B_0}\right)yz, \qquad (2\text{-}7)$$

where x, y, and z are the laboratory coordinates, and B_0, g_x, g_y, and g_z are the static field and the readout gradients in the laboratory system, respectively. The first two terms are self-squared terms, and the last two are quadratic cross-terms. Considering the presence of both B_0 field inhomogeneities and concomitant gradient fields and ignoring relaxation, the received MR signal from Equation 2-4 can be modified as follows:

$$s(t) = \int m(\boldsymbol{r})\, e^{-i2\pi \boldsymbol{k}(t)\boldsymbol{r}}\, e^{-i(\Delta\omega(\boldsymbol{r})t + \phi_c(\Delta\omega_c(\boldsymbol{r}),t)}\, d\boldsymbol{r}, \qquad (2\text{-}8)$$

where $\phi_c(\Delta\omega_c(\boldsymbol{r}), t)$ represents the phase accrual due to concomitant fields B_c. If concomitant fields are not properly accounted for in pulse sequence design and/or image reconstruction, the induced unwanted phase accrual may lead to severe signal dropouts, image blurring, or ghosting artifacts in a variety of imaging methods, including but not limited to TSE imaging[24], spiral imaging[25], and echo-planar imaging (EPI)[26,27].

Several strategies of concomitant gradient compensation have been developed to eliminate or minimize the associated image degradation. For example, Zhou et al.[24] has proposed approaches

for reducing the phase errors produced by the concomitant field in Cartesian TSE, which includes gradient waveform symmetrization and reshaping, quadratic nulling, and gradient de-rating. Other methods, such as adding a linear gradient in the slice-selection direction[26] before the readout train and/or phase correction during image reconstruction, have been well described to correct for EPI images with ghosting, image distortion, and blurring.

2.4 Low-field systems

It has been several decades that MRI systems have trended toward higher main magnetic field strengths (e.g., 3 T, 7 T, or even 10.5 T) to maximize signal to noise ratio (SNR) and/or achieve high spatial/temporal resolution while minimizing the total scan time. However, the high cost of the high-field system itself and its related expenses such as the installation cost and maintenance cost limit its wide-spread use, especially in low-income countries. Therefore, low-field systems (< 1 T) equipped with modern hardware have recently regained increasing interest[28,29], primarily because of their low cost and accessibility. In this section, we will briefly describe the opportunities and challenges in technological development using low-field MRI scanners.

2.4.1 Opportunities

One key benefit of low-field systems is a more homogeneous main magnetic field, when compared to most clinically used 1.5 T and 3 T scanners. This characteristic favors sampling-efficient pulse sequences, such as bSSFP, MR fingerprinting, and spiral imaging, to mitigate the need for artifact reduction from B_0 inhomogeneity and improve SNR efficiency. Second, a shorter T_1 and a longer T_2/T_2^*, allow for longer readouts and longer echo trains, which may benefit pulse sequence development for fast acquisition (e.g., TSE). Third, reduced susceptibility gradients alleviate the concern of air-tissue boundary artifacts, enabling superior image quality in some areas, such as the

lung and the brain near the cranial sinus. Last but not at least, a reduced RF specific absorption rate (SAR) provides promise in MRI-guided procedures. For example, Campbell-Washburn et al.[28] successfully performed MRI-guided right heart catheterization on a high-performance 0.55 T scanner and demonstrated the safety of RF-induced heating in conductive devices (e.g., guidewires, catheters).

2.4.2 Challenges

In reality, nothing is perfect. Low-field systems still face several limitations. One primary issue is the inherent low SNR due to a low field strength. The problem will become more severe when performing SNR-limited application such as diffusion imaging. However, several methods have been developed to mitigate SNR loss at low-fields, including the use of SNR efficient sampling strategies and deep learning-based noise reduction[30]. For instance, bSSFP imaging with prolonged spiral readouts has demonstrated an SNR increase compared to the Cartesian counterpart.[31]

Concomitant field induced phase error is another main concern at low-field systems. As described in the previous section, Equation 2-7 indicates that concomitant fields scale with the gradient amplitude and off-center distance but inversely with the field strength, which becomes further exaggerated at low magnetic field strengths (< 1.5 T) and when using readouts with high gradient amplitudes (> 20 mT/m). In Chapters 4 and 5, we will present strategies in detail for compensation of concomitant fields in spiral TSE imaging at 0.55 T in order to generate images with minimal artifacts.

2.5 References

1. Bloch F. Nuclear induction. *Phys Rev*. 1946; 70:460-474,1946.
2. Pennell, DJ. Cardiovascular magnetic resonance. *Circulation*. 2010;121(5), 692-705.

3. Carr JC, Simonetti O, Bundy J, Li D, Pereles S, Finn JP. Cine MR angiography of the heart with segmented true fast imaging with steady-state precession. *Radiology*. 2001;219:828–834.

4. Meyer CH, Hu BS, Nishimura DG, Macovski A. Fast spiral coronary artery imaging. *Magn Reson Med*. 1992; 28:202-213.

5. Hennig J, Nauerth A, Friedburg H. RARE imaging: a fast imaging method for clinical MR. *Magn Reson Med*. 1986; 3:823-833.

6. Mugler JP 3rd. Optimized three-dimensional fast-spin-echo MRI. *J Magn Reson Imaging*. 2014;39(4):745-767. doi:10.1002/jmri.24542

7. Hajnal JV, Bryant DJ, Kasuboski L, et al. Use of Fluid Attenuated Inversion Recovery (FLAIR) pulse sequences in MRI of the brain. *J Comput Assist Tomogr*. 1992; 16:841-844.

8. Grasso D, Borreggine C, Castorani G, et al. Balò's concentric sclerosis in a case of cocaine-levamisole abuse. *SAGE Open Medical Case Reports*. 2020;8.

9. Scheffler, K., Lehnhardt, S. Principles and applications of balanced SSFP techniques. *European radiology*. 2003;13(11), 2409-2418.

10. Duyn JH, Yang Y, Frank JA, van der Veen JW. Simple correction method for k-space trajectory deviations in MRI. *J Magn Reson*. 1998; 132:150 –153.

11. Tan H, Meyer CH. Estimation of k-space trajectories in spiral MRI. *Magn Reson Med*. 2009; 61:1396–1404.

12. Vannesjo SJ, Haeberlin M, Kasper L, Pavan M, Wilm BJ, Barmet C, Pruessmann KP. Gradient system characterization by impulse response measurements with a dynamic field camera. *Magn Reson Med*. 2013; 69: 583–593.

13. Noll DC, Meyer CH, Pauly JM, Nishimura DG, Macovski A. A homogeneity correction method for magnetic resonance imaging with time-varying gradients. *IEEE Trans Med Imaging*. 1991; 10:629–637.

14. Irarrazabal P, Meyer CH, Nishimura DG, Macovski A. Inhomogeneity correction using an estimated linear field map. *Magn Reson Med*. 1996; 35:278–282.

15. Man LC, Pauly JM, Macovski A. Multifrequency interpolation for fast off-resonance correction. *Magn Reson Med*. 1997; 37:785–792.

16. Noll DC, Pauly JM, Meyer CH, Nishimura DG, Macovski A. Deblurring for non-2D fourier transform magnetic resonance imaging. *Magn Reson Med*. 1992; 25:319–333.

17. Man LC, Pauly JM, Macovski A. Improved automatic off-resonance correction without a field map in spiral imaging. *Magn Reson Med*. 1997; 37:906–913.

18. Chen W, Meyer CH. Semiautomatic off-resonance correction in spiral imaging. *Magn Reson Med*. 2008; 59:1212–1219.

19. Allen SP, Feng X, Fielden SW, Meyer CH. Correcting image blur in spiral, retraced in/out (RIO) acquisitions using a maximized energy objective. *Magn Reson Med*. 2019; 81:1806–1817.

20. Sutton BP, Noll DC, Fessler JA. Fast, iterative image reconstruction for MRI in the presence of field inhomogeneities. *IEEE Trans Med Imaging*. 2003; 22:178–188.

21. Wang D, Zwart NR, Pipe JG. Joint water-fat separation and deblurring for spiral imaging. *Magn Reson Med*. 2018; 79: 3218- 3228.

22. Lim Y, Bliesener Y, Narayanan S, Nayak KS. Deblurring for spiral real-time MRI using convolutional neural networks. *Magn Reson Med*. 2020;84:3438–3452.

23. Bernstein MA, Zhou XJ, Polzin JA, King KF, Ganin A, Pelc NJ, Glover GH. Concomitant gradient terms in phase contrast MR: analysis and correction. *Magn Reson Med*. 1998; 39:300–308.

24. Zhou XJ, Tan SG, Bernstein MA. Artifacts induced by concomitant magnetic field in fast spin echo imaging. *Magn Reson Med*. 1998;40:582–591.

25. King KF, Ganin A, Zhou XJ, Bernstein MA. Effect of Maxwell fields in spiral scans. Concomitant gradient field effects in spiral scans. *Magn Reson Med*. 1999;41:103–112.

26. Zhou XJ, Du YP, Bernstein MA, Reynolds HG, Maier JK, Polzin JA. Concomitant magnetic field induced artifacts in axial echo planar imaging. *Magn Reson Med*. 1998; 39:596–605.

27. Du YP, Joe Zhou X, Bernstein MA. Correction of concomitant magnetic field-induced image artifacts in nonaxial echo-planar imaging. *Magn Reson Med*. 2002;48(3):509–15.

28. Campbell-Washburn AE, Ramasawmy R, Restivo MC, et al. Opportunities in interventional and diagnostic imaging by using high-performance low-field-strength MRI. Radiology. 2019;293:384–393.

29. Arnold TC, Freeman CW, Litt B, Stein JM. Low-field MRI: Clinical promise and challenges. *J Magn Reson Imaging*. 2022;10.1002/jmri.28408.

30. Koonjoo N, Zhu B, Bagnall GC, Bhutto D, Rosen MS. Boosting the signal-to-noise of low-field MRI with deep learning image reconstruction. *Scientific reports*. 2021 Apr 15;11(1):1-6.

31. Restivo MC, Ramasawmy R, Bandettini WP, Herzka DA, Campbell-Washburn AE. Efficient spiral in-out and EPI balanced steady-state free precession cine imaging using a high-performance 0.55T MRI. *Magn Reson Med*. 2020;84:2364–2375.

Chapter 3: SPRING-RIO TSE: 2D T_2-weighted turbo spin-echo brain imaging using SPiral RINGs with Retraced In/Out trajectories

3.1 Introduction

As described in the background section, T_2-weighted pulse sequences are widely used for clinical neuroimaging because of their high sensitivity for many neurological disorders. Turbo-spin-echo (TSE) pulse sequences, also known as fast-spin-echo (FSE), are commercial implementations of the Rapid Acquisition with Relaxation Enhancement (RARE) technique[1], and have replaced conventional spin-echo (SE) technique for T_2-weighted imaging, due to their faster acquisition times. Therefore, 2D and 3D TSE have become the workhorse pulse sequences for T_2-weighted imaging in the routine clinical MR neuro exam.[2,3]

Although 2D Cartesian TSE sequence is one of the standard methods for T_2-weighted imaging, the high specific absorption rate (SAR) induced by a large number of refocusing RF pulses limits its use at high magnetic fields. The long RF pulse train may produce T_2-decay blurring[4,5] and may also alter the image contrast compared to the conventional SE[6]. Another limitation of Cartesian TSE is a relatively long scan time attributed to the low sampling efficiency, typically taking minutes for images with sub-millimeter spatial resolution, which may induce motion artifacts from patient motion.

Compared to Cartesian sampling, spiral imaging[7] covers k-space more efficiently via a higher average k-space velocity, thereby reducing total scan time and/or improving SNR. Spiral imaging also has the advantage of reduced sensitivity to motion artifacts, and flow artifacts are

often minimal and isotropic. Spiral acquisitions have been incorporated into a 2D TSE signal generation module via two strategies: an interleaved, rotated spiral-arm segmentation and an annular ring segmentation. The first strategy, as proposed by Li et al.[8], shows that this spiral-based TSE technique offers advantages over conventional Cartesian TSE in terms of SNR efficiency, improved image contrast, and reduced SAR. However, this method requires a double-encoding strategy and a signal-demodulation method to mitigate swirl-like artifacts due to T_2-decay induced signal variation, extending the scan time. The annular ring strategy[9-13] splits long spiral trajectories into several annular segments, with the benefit of reduced T_2-decay artifacts by converting the T_2-dependent signal modulation into a k-space apodizing filter. This method was first implemented in abdominal imaging within one breath-hold[9] and single-shot brain imaging[10], showing a promising potential for fast T_2-weighted imaging.

Previously, we described a 2D spiral-ring (abbreviated 'SPRING') TSE technique[11] which was adapted from the method proposed by Block et al.[9] for dual-contrast T_2-weighted imaging at 1.5 T using a spiral ring segmentation and a shared-view acquisition. The results demonstrated that ring segmentation leads to a smoothed T_2-dependent weighting of signal amplitudes across k-space and thus benign artifact behavior. One key advantage of this annular-ring segmentation, compared to the interleaved, rotated spiral-arm segmentation, is that there is no need for the double-encoding strategy, thus resulting in a shorter scan time. However, there are still challenges associated with this technique, such as residual T_2-decay blurring and off-resonance induced signal loss. In addition, early echoes are typically discarded to achieve the desired T_2-weighting, resulting in a reduced scan efficiency. Furthermore, the annular-ring sampling strategy has not been fully explored for brain imaging via either a single-shot excitation or multi-shot acquisitions.

In this chapter, a new approach to 2D TSE imaging using annular spiral rings with a retraced in/out trajectory, dubbed 'SPRING-RIO TSE[12]', is proposed to address these aforementioned challenges. First, we introduce the sampling strategy of annular rings with retraced in/out (RIO)[12-14] segments and demonstrate potential advantages of this approach via simulations. Second, we describe methods for correcting for k-space trajectory infidelity and off-resonance effects. Finally, we validate the feasibility of the proposed technique and compare its performance to that of SPRING TSE and Cartesian TSE in phantom and in vivo scans.

3.2 Technique

3.2.1 Pulse sequence

SPRING TSE[9,11] has high acquisition efficiency, but is prone to off-resonance induced artifacts and signal loss because the center of k-space is not aligned with the spin echo, and the phase change does not grow linearly with k-space radius due to the interspersed refocusing RF pulses. Furthermore, although the k-space apodizing filter introduced by annular-ring acquisition can mitigate the T_2-decay artifacts by smoothing the signal modulation along the echo train, this filter inevitably leads to an apparent spatial resolution loss.

To mitigate image artifacts and blurring, and to further improve the sampling efficiency, the SPRING-RIO TSE pulse sequence is proposed as follows. The pulse sequence timing diagram depicted in Figure 3-1 shows the sampling strategy, which includes fat saturation to suppress lipid signals, field map acquisition, and TSE data acquisition using annular spiral rings. Short spiral-out arms were placed in the interval between the excitation and the first refocusing RF pulses for field map acquisition, with a 1 ms interval between the odd and even shots, to allow for a range of ±500 Hz off-resonance. The TSE data was then collected by a series of spiral rings, including a self-

retraced spiral in-out ring for the center of k-space, and spiral-out rings at the end of the echo train paired with time-reversed, spiral-in rings with opposite gradient polarity at the beginning of the echo train, to acquire the outer portion of k-space. Examples of retraced spiral trajectories are shown at the bottom of Figure 3-1. The inner portion of k-space was sampled along the path X – O – X in a single echo spacing (ESP), while the outer k-space was sampled twice via the path Z – Y by the earlier spiral-in rings and the path Y – Z by the later spiral-out rings. A given ring of k-space values was sampled by two trajectories, $\boldsymbol{k_{j,p}}(t)$ and $\boldsymbol{k_{j,q}}(t)$, for which the subscripts j, p and j, q stand for the same j^{th} k-space ring coverage but acquired at two different echoes p and q, by the respective spiral-out rings and the spiral-in rings. T_p and T_q refer to the time interval between the excitation RF pulse and the center of the readout window at p^{th} and q^{th} echoes, respectively. Because of symmetry of the retracing about TE,

$$T_p + T_q = 2\,TE, \tag{3-1}$$

where $0 \le p \le L-1,\ -L+1 \le q \le 0,$ and L is the total number of spiral-out rings.

For $t \in [-\frac{T}{2}, \frac{T}{2}]$, $\boldsymbol{k_{j,p}}(t)$ and $\boldsymbol{k_{j,q}}(t)$ can be written as:

$$\boldsymbol{k_{j,p}}(t) = \boldsymbol{k_{j,q}}(-t) = -\boldsymbol{k_{j,q}}(t), \tag{3-2}$$

where T is the readout time, and $\boldsymbol{k_{j,p}}(t)$ and $\boldsymbol{k_{j,q}}(t)$ are constrained to be antisymmetric and mirrored at time points symmetric about the spin echo. The central self-retraced spiral in-out segment can be considered as the special case when $p = q = 0$.

3.2.2 Gradient design

In a typical TSE acquisition module, the gradient-induced dephasing within each echo spacing should be constant, and non-zero, to preserve the Carr-Purcell-Meiboom-Gill (CPMG) condition[15].

For our design, a constant non-zero zeroth order gradient moment is provided by crusher gradients surrounding the refocusing RF pulses. The zeroth order gradient moments of the spiral readout gradients were nulled in each echo spacing by surrounding them with prephaser gradients that move out from the origin of k-space to the beginning of the segment, and rephaser gradients that move back to the origin from the end of the segment. The prephaser and rephaser lobes were designed to be played simultaneously with the crusher gradients. To obtain submillimeter in-plane spatial resolution, an interleaved multi-shot acquisition was used to interleave the spiral ring gradients over several repetition times to cover all of k-space. A constant density spiral trajectory design was used, based on the algorithm of Meyer et al.[7,16], to obtain minimum-time spiral readouts constrained by gradient slew rate and amplitude limits.

The spiral gradient waveforms for multi-shot SPRING-RIO TSE were designed using the following 6-step procedure.

1. a single, very long spiral-out arm was generated with desired imaging properties, such as FOV, spatial resolution and number of shots;
2. this spiral arm was split into L segments of equal time duration;
3. the gradient polarity of a copy of the 1st segment was inverted, and this segment was then time-reversed and placed in front of the original 1st segment to generate a self-retraced spiral-in-out annular ring, which was played at the effective echo time (TE_{eff});
4. the remaining 2nd to L segments were placed consecutively at the subsequent TSE echoes (following TE_{eff});
5. the gradient polarities of copies of the 2nd to L segments were inverted, and these segments were then time-reversed and placed consecutively, in reverse order, at the TSE echoes preceding TE_{eff};

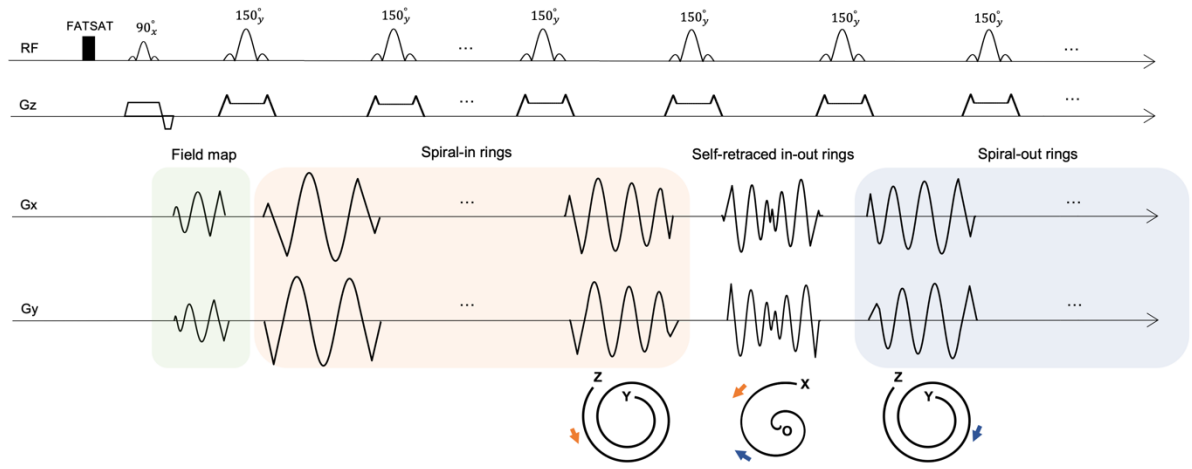

Figure 3-1. Pulse sequence timing diagram showing that the X point in the inner self-retraced in-out rings is sampled twice in k-space, and the neighboring Y point is sampled in both the preceding spiral-in ring and the following spiral-out ring. For each shot, the number of spiral-in rings (including the first half of the central spiral-in/out ring) is equal to that of spiral-out rings (including the latter half of the central spiral-in/out ring), which was set to 7, with a total of 15 shots per measurement. The refocusing RF pulse angles are set to 150° for reduced SAR.

6. the waveforms generated as described in steps 1-5 were rotated N times to obtain a total of $N * (2 * L - 1)$ spiral ring waveforms.

For multi-shot SPRING TSE, L gradient segments were generated using steps 1 and 2 above. Then, the L segments were placed sequentially at the TSE echoes, starting with the 1st segment played at TE_{eff}. Finally, the waveforms were rotated N times to obtain a total of $N * L$ spiral ring waveforms.

The selection of L depends on the in-plane spatial resolution, FOV, the readout acquisition time, and the total scan time. For example, for a given FOV, spatial resolution, and the total scan time, SPRING-RIO TSE with a longer readout window per ring requires a smaller value of L, and vice versa. Sequences with a larger L will reduce the sensitivity to B_0 inhomogeneities but increase the RF SAR. The TE_{eff} may also affect the selection of L for SPRING-RIO TSE, because $L \times ESP \approx TE_{eff}$, if L fully retraced spiral-in rings are placed in the early echoes. Empirically, sequences with a longer ESP and a smaller L will produce a shorter TE_{eff} compared to that with

a shorter ESP and a larger L, since the former one saves certain amounts of time, such as the time used for the refocusing RF. Here, $L = 7$ and $N = 15$ were chosen for both multi-shot SPRING TSE and SPRING-RIO TSE.

3.2.3 K-space trajectory fidelity

As described in Chapter 2, in non-Cartesian readout sequences such as spiral imaging, eddy currents and anisotropic delays of the gradient system generally affect the fidelity of the k-space trajectory and cause image blurring and/or artifacts[17] if not corrected. In this section, we applied a model-based method[18,19], which has been studied for spiral-out and spiral-in/out sequences, to estimate the actual trajectory for each annular spiral ring. The modified k-space trajectory estimation model as introduced by Feng et al.[20] is:

$$\widetilde{\boldsymbol{k}}(t) \approx (1 + A)\boldsymbol{k_d}(t) + B \int_0^t \boldsymbol{k_d}(\tau) d\tau, \tag{3-3}$$

where $\widetilde{\boldsymbol{k}}(t)$ is the estimated k-space trajectory, $\boldsymbol{k_d}(t)$ is the k-space trajectory on one physical axis with a gradient delay ΔT, and A and B are assumed to be constant values and independent of the image orientation and spiral parameters. To determine the values of the optimal delay time ΔT, A, and B on each physical axis, a set of trajectory measurements was performed on the scanner using Duyn's method[20], followed by a least-squares fit with the model given in Equation 3-3.

To evaluate the effects of the k-space trajectory estimation model, we measured the actual k-space trajectory in phantom experiments for SPRING TSE and SPRING-RIO TSE sequences. Both the estimated k-space trajectories themselves and the images reconstructed with these trajectories were compared to the theoretical trajectories and the corresponding images.

3.3 Simulations

All simulations were implemented in MATLAB (R2020b software; MathWorks, Natick, MA). To demonstrate the benefits of the RIO trajectory design of SPRING-RIO TSE, we simulated its response to system nonidealities, T_2-decay effects and B_0 off-resonance effects, and compared the results to those of SPRING TSE. A few properties of these two k-space trajectories must be defined (see below) before simulations. Assuming T_2^*-decay effects during each readout are negligible when compared to T_2-decay effects along the echo train, the received MR signal for the j^{th} k-space ring acquired at the echo time T_p can be modeled as below:

$$s_{j,\mathrm{p}}(t) = \int m(\boldsymbol{r})\, e^{-i2\pi \boldsymbol{k}_{j,\mathbf{p}}(t)\boldsymbol{r}}\, e^{-i\omega(\boldsymbol{r})t}\, e^{\frac{-T_p}{T_2}} d\boldsymbol{r}, \tag{3-4}$$

where $m(\boldsymbol{r})$ is the object's complex-valued magnetization and $\omega(\boldsymbol{r})$ is the spatially varying resonant frequency of the object. Equation 3-4 describes the signal for SPRING TSE during one ring acquisition. It is shown in Appendix A that, for $t \in [-\frac{T}{2}, \frac{T}{2}]$, the signal resulting from averaging the data from a retraced in-out trajectory of SPRING-RIO TSE can be written as:

$$s(t) = \int m(\boldsymbol{r})\, e^{-i2\pi \boldsymbol{k}_{j,\boldsymbol{p}}(t)\boldsymbol{r}} e^{\frac{-TE}{T_2}} \left[\cos[\omega(\boldsymbol{r})t]\cosh\left(\frac{T_p - TE}{T_2}\right) + isin[\omega(\boldsymbol{r})t]\sinh\left(\frac{T_p - TE}{T_2}\right)\right] d\boldsymbol{r}. \tag{3-5}$$

3.3.1 T_2-decay effects

Ignoring B_0 inhomogeneity and T_2^* relaxation during the acquisition window, but including T_2 relaxation along the echo train direction, we can simplify Equations 3-4 and 5 for SPRING TSE and SPRING-RIO TSE as below:

$$s_{SPRING}(t) = \int m(\boldsymbol{r})\, e^{-i2\pi \boldsymbol{k}_{j,\boldsymbol{p}}(t)\boldsymbol{r}}\, e^{\frac{-T_p}{T_2}} d\boldsymbol{r}, \quad \text{and} \tag{3-6}$$

$$s_{SPRING-RIO}(t) = \int m(\boldsymbol{r})\, e^{-i2\pi \boldsymbol{k_{j,p}}(t)\boldsymbol{r}}\, e^{\frac{-TE}{T_2}}\, \cosh\left(\frac{T_p - TE}{T_2}\right) d\boldsymbol{r}. \quad (3\text{-}7)$$

The impact of T_2 relaxation was calculated and compared among each of the described trajectories. A matrix of ones was inverse-gridded with each trajectory, and T_2 relaxation on the order of the k-space radius was simulated by exponentially decreasing the amplitude of the simulated data. The simulated data was then gridded and displayed as the windowing patterns of k-space. Point-spread-functions (PSFs) were calculated with zero padding and normalized to [0,1], and the corresponding full width at half maximum (FWHM) values were compared to determine the effects of T_2 decay on these sampling trajectories. Moreover, digital phantom simulations for SPRING TSE and SPRING-RIO TSE were performed, and the corresponding mean structural similarity indices (SSIM)[21] were calculated and compared based the reference condition without T_2 decay. The mean SSIM is defined as below:

$$mean\ \mathrm{SSIM}(\mathrm{X},\mathrm{Y}) = \frac{1}{M}\sum_{j=1}^{M} \frac{(2\, u_{x_j} u_{y_j} + C_1)(2\, \sigma_{x_j y_j} + C_2)}{(u_{x_j}{}^2 + u_{y_j}{}^2 + C_1)(\sigma_{x_j}{}^2 + \sigma_{y_j}{}^2 + C_2)}, \quad (3\text{-}8)$$

where X and Y are two input images, x_j and y_j are the image contents at the j^{th} local window, M is the number of local windows in the image. u is the mean intensity, and σ is the standard deviation over one local window. $C_1 = (0.01 * L)^2$, and $C_2 = (0.03 * L)^2$ are used here as the default parameters, where L is the dynamic range of the images. The maximum mean SSIM index value 1 is achieved only if X and Y are identical. For these simulations, FOV = 230 mm, echo train length (ETL) = 7 (SPRING TSE) or 13 (SPRING-RIO TSE), ESP = 13.5 ms, and T_2 = 70 ms.

3.3.2 B_0 off-resonance effects

The k-space phase of an off-resonant point object in SPRING-based TSE acquisitions does not grow monotonically with increasing k-space radius.[9] Instead, phase is accrued from off-resonance

over each echo spacing, with a (refocused) zero phase at the center of each echo spacing and a phase at the beginning of the next echo spacing that is inverted compared to that at the end of the preceding echo spacing.

To assess the extent of off-resonance effects, PSFs for SPRING TSE and SPRING-RIO TSE trajectories with various amounts of off-resonance were simulated by performing nonuniform FFT (NUFFT) reconstruction on a matrix of ones. Off-resonance was added by linearly increasing the phase of the simulated data during each echo spacing. The corresponding digital phantom images with three different amounts of phase accumulated at the end of the readout were further simulated for visual comparison between these two sequences. SSIM values were calculated and compared as well. For these simulations, FOV = 230 mm, ETL = 7 (SPRING TSE) or 13 (SPRING-RIO TSE), ESP = 15 ms, ADC = 8 ms, and offset frequency = 31.25 Hz (1/4 cycles), 62.5 Hz (1/2 cycles) or 93.75 Hz (3/4 cycles).

3.4 MRI experiments

3.4.1 Data acquisition

Experiments were performed on a 3T scanner (MAGNETOM Prisma, Siemens Healthcare, Erlangen, Germany) with a 32-channel head coil.

In a phantom study, axial data from a resolution phantom was acquired with SPRING TSE and the proposed SPRING-RIO TSE to evaluate the efficacy of the RIO trajectory design. Model-based trajectory measurements were performed for both sequences, and the estimated trajectories were then compared to the nominal trajectories, in terms of image quality such as edge artifacts and blurring to demonstrate the necessity of trajectory infidelity correction. Relevant spiral imaging parameters include FOV = $180 \times 180\, mm^2$, spatial resolution = $0.60 \times 0.60\, mm^2$,

slice thickness = 4 mm, refocusing RF flip angle = 150°, ETL = 7 for SPRING TSE and 13 for SPRING-RIO TSE, ESP = 14.8 ms with ADC = 7 ms. In k-space trajectory measurements, the distance between the excited slice and the isocenter was 35 mm, and the slice thickness was 0.6 mm.

Five healthy volunteers with informed consent participated in this study and were scanned using the two spiral-based TSE sequences and standard Cartesian TSE to evaluate the overall image quality. For each of these three sequences, data were acquired consecutively at the same image planes with 14 slices, 4 mm slice thickness, and 2 mm gap. Axial, coronal, and sagittal slices of the head were collected, with the FOV set to $230 \times 230\ mm^2$ for the axial plane, increasing to $250 \times 250\ mm^2$ for coronal and sagittal planes with slightly reduced resolution to avoid aliasing. The data of each slice was acquired twice for SPRING TSE and SPRING-RIO TSE sequences, with 45 seconds per measurement, and therefore one signal average (1-NSA) requires 0:45 min total scan time while two signal averages (2-NSA) require 1:30 min. Spiral k-space trajectories were estimated based on the system parameters obtained from the model-based trajectory calibration. For all sequences, a fat saturation pulse was used to null the bright fat signal and avoid the strong chemical shift effect at 3T, and the refocusing RF flip angle was set to 150°, which was used to reduce SAR to an acceptable value for Cartesian TSE. Table 3-1 lists additional parameters of these three pulse sequences.

Sequences	TR (ms)	TEeff (ms)	Readout (ms)	Refocusing RF	ESP (ms)	ETL	# Shots	# NSA	Total scan time (min)	Spatial Res (mm^3)
SPRING TSE	3000	93.2	7	150°	13.3	7	15	1/2	0:45/1:30	0.60×0.60×4
SPRING-RIO TSE	3000	93.2	7	150°	13.3	13	15	1/2	0:45/1:30	0.60×0.60×4
Cartesian TSE	3000	92	2.99	150°	9.9	15	29	1	1:31	0.60×0.60×4

Table 3-1. Sequence parameters for SPRING TSE, SPRING-RIO TSE, and Cartesian TSE.

The reconstruction was performed offline in MATLAB. The NUFFT code from the Michigan Image Reconstruction Toolbox (MIRT) package[22] was used for direct 2D non-Cartesian image reconstruction. Coil sensitivity maps were computed from the center k-space data of the field map using ESPIRiT[23]. To illustrate the performance of the trajectory correction, phantom images were reconstructed and compared with the nominal k-space trajectory and the estimated k-space trajectory.

As described in Chapter 2, for spiral imaging with long readouts, deblurring is an essential step to correct for off-resonance-induced phase errors.[24-31] In this section, semiautomatic deblurring of the component images using an established minimized phase objective function[28-30] was applied to SPRING TSE, with the objective function:

$$\min_{\omega_i} \int h(\boldsymbol{r}-\boldsymbol{r}')\ |\text{Imag}\{\tilde{m}(\boldsymbol{r}';\omega_i(\boldsymbol{r}'))\}|^{\alpha} d\boldsymbol{r}', \tag{3-9}$$

where α takes on values in the range from 0.5 to 1, Imag is the imaginary part of the image, $\tilde{m}(\boldsymbol{r};\omega_i(\boldsymbol{r}))$ is the image reconstructed at demodulation frequency ω_i, and $h(\boldsymbol{r})$ is the convolution kernel chosen to be a circularly symmetric Gaussian window.

Regarding SPRING-RIO TSE, as noted by Fielden et al.[14] and Allen et al.[31], moderate off-resonance effects can be automatically corrected by the RIO design; however, at large off-resonance values, this effect quickly degrades, and substantial blurring may remain. We chose the semiautomatic deblurring method with a maximized energy objective function proposed by Allen et al.[31] for a specific RIO trajectory in spiral imaging and extended it to correct for off-resonance effects in SPRING-RIO TSE, using the objective function:

$$\max_{\omega_i} \int h(\boldsymbol{r}-\boldsymbol{r}')\ \tilde{m}\big(\boldsymbol{r}';\omega_i(\boldsymbol{r}')\big)\ \tilde{m}(\boldsymbol{r}';\omega_i(\boldsymbol{r}'))^{*} d\boldsymbol{r}', \tag{3-10}$$

where $\tilde{m}(\boldsymbol{r};\omega_i(\boldsymbol{r}))^*$ is the complex conjugate of $\tilde{m}(\boldsymbol{r};\omega_i(\boldsymbol{r}))$. Appendix B shows that the global maximum of Equation 3-10 is invariant with T_2 decay and invariant with image phase, which eliminates the need to accurately remove the incidental phase before applying this criterion.

A low-resolution field map for the semiautomatic deblurring method was generated from the first short spiral-out arms by extracting the phase difference between the odd shots and even shots. Both phantom and in vivo brain images from SPRING TSE and SPRING-RIO TSE were reconstructed and compared with and without deblurring methods.

3.4.2 Image quality analysis

Quantitative evaluation of the proposed SPRING-RIO TSE sequence and standard Cartesian TSE sequence was performed using phantom and in vivo brain data. For brain images, regions of interest (ROIs) were drawn in the gray matter (GM) and white matter (WM) on axial images from SPRING-RIO TSE and Cartesian TSE acquisitions. Signal intensities were measured on five subjects, with ten slices per subject, and the relative SNR of ROIs and image contrast between ROIs were then calculated. The apparent SNR was measured by dividing the mean image intensity in the specified region by the standard deviation of the image intensity outside the phantom or skull and multiplying the result by the 0.66 Rayleigh distribution correction factor. Pairwise comparisons were performed on a total of 50 pairs of SNR measurements using the Tukey-Kramer method. Similarly, the apparent image contrast between ROIs was also measured using:

$$Contrast = \frac{(\text{signal 1} - \text{signal 2})}{0.5 * (\text{signal 1} + \text{signal 2})}. \tag{3-11}$$

3.5 Results

3.5.1 Simulations

The simulation results illustrated the benefits of the RIO trajectory design of SPRING-RIO TSE over the original SPRING TSE implementation in terms of T_2-decay induced resolution loss and off-resonance induced artifacts and signal loss. The windowing patterns of k-space due to T_2 relaxation during acquisition are shown in the top row of Figure 3-2. For SPRING TSE, T_2 relaxation results in a windowing of the data, with higher spatial frequencies losing signal, causing a broadening of the main lobe of the PSF (FWHM:1.59). The RIO strategy in SPRING-RIO TSE produces a smoother frequency response, thus maintaining a PSF main lobe (FWHM:1.32) nearly as sharp as that for the constant signal with no T_2-decay effects (FWHM:1.41). The comparison among the bottom images reconstructed from SPRING TSE, SPRING-RIO TSE, and the reference, and the corresponding SSIM values, demonstrate the advantage of using RIO sampling for reducing T_2-decay induced blur and subsequent resolution loss.

Figure 3-3 shows the PSFs for 1/4, 1/2, and 3/4 phase cycles of phase accrual from off-resonance over each of annular spiral ring segments. For both sequences, the effect of the refocusing RF pulses is to modulate the blurring so that there is not a substantial apparent loss of image resolution, but there is a signal loss that increases with off-resonance frequency. SPRING-RIO TSE performs better than SPRING TSE with less energy in the side lobes of the PSF. The reconstructed digital phantom images along with the SSIM values demonstrate this signal degradation with increasing off-resonance frequency, and the merit of RIO trajectory design for self-correction of moderate off-resonance effects ranging up to 1/2 phase cycle. Difference images of simulated digital brain images from SPRING TSE or SPRING-RIO TSE with T_2 decay or off-resonance effects compared

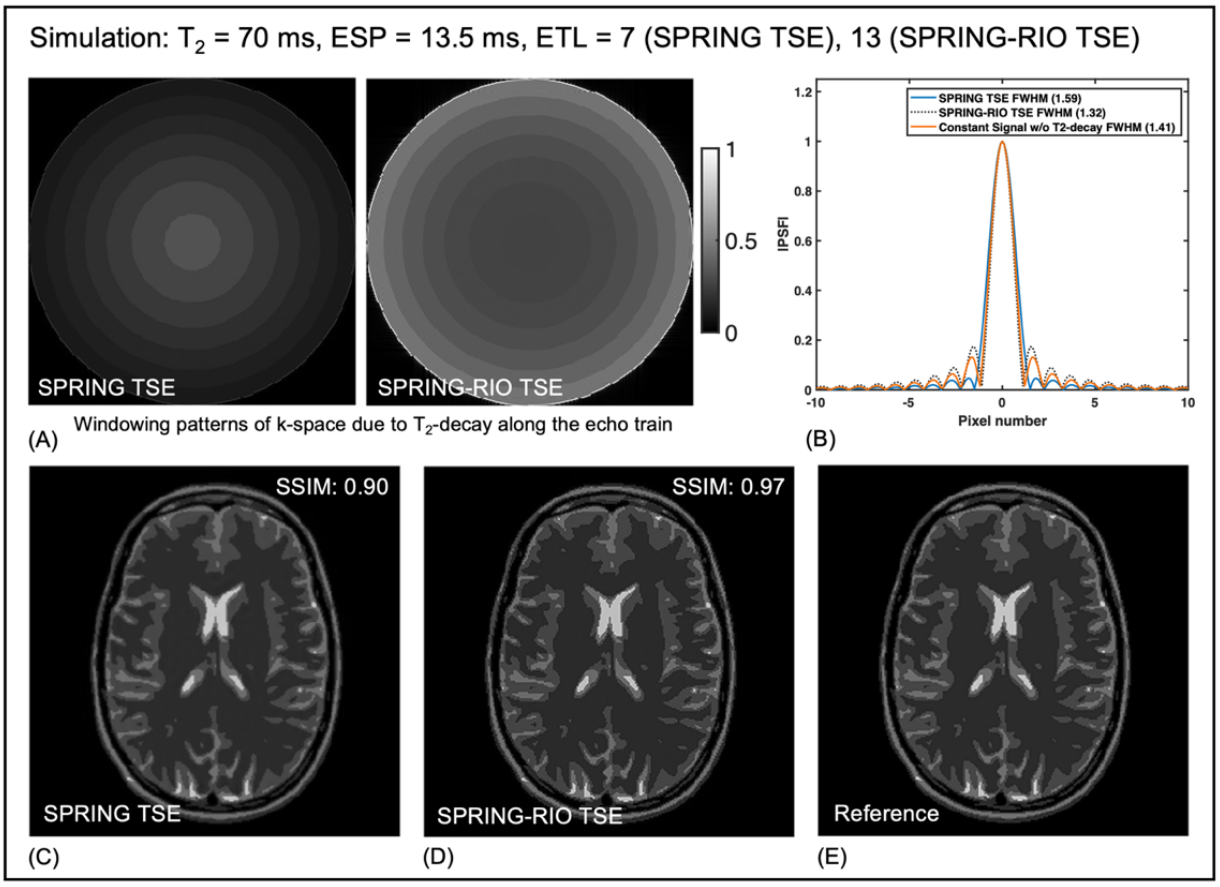

Figure 3-2. Simulation results of T_2-decay effect for SPRING TSE and SPRING-RIO TSE. Windowing patterns of k-space (A) and center lines of 2D PSFs (B) are shown for each trajectory. Note that the PSF was normalized to [0, 1] by dividing by its own peak; the peak for SPRING-RIO TSE is higher than that for SPRING TSE because of the additional data acquired in the early echoes.

to the reference are in Figure 3-4. Another example of an inferior slice with air/susceptibility from a digital brain phantom with off-resonance effects for SPRING TSE and SPRING-RIO TSE can be found in Figure 3-5.

3.5.2 Phantom images

Figure 3-6 shows reconstructions of one axial slice from a resolution phantom from SPRING TSE (Fig. 4a-f) and SPRING-RIO TSE (Fig. 3-6g-i) acquisitions using the theoretical trajectory (Fig. 3-6a,g), isotropic delay corrected trajectory (Fig. 3-6b,h), and model-based trajectory (Fig. 3-6c,i), as well as their corresponding absolute difference images relative to the goal images based on

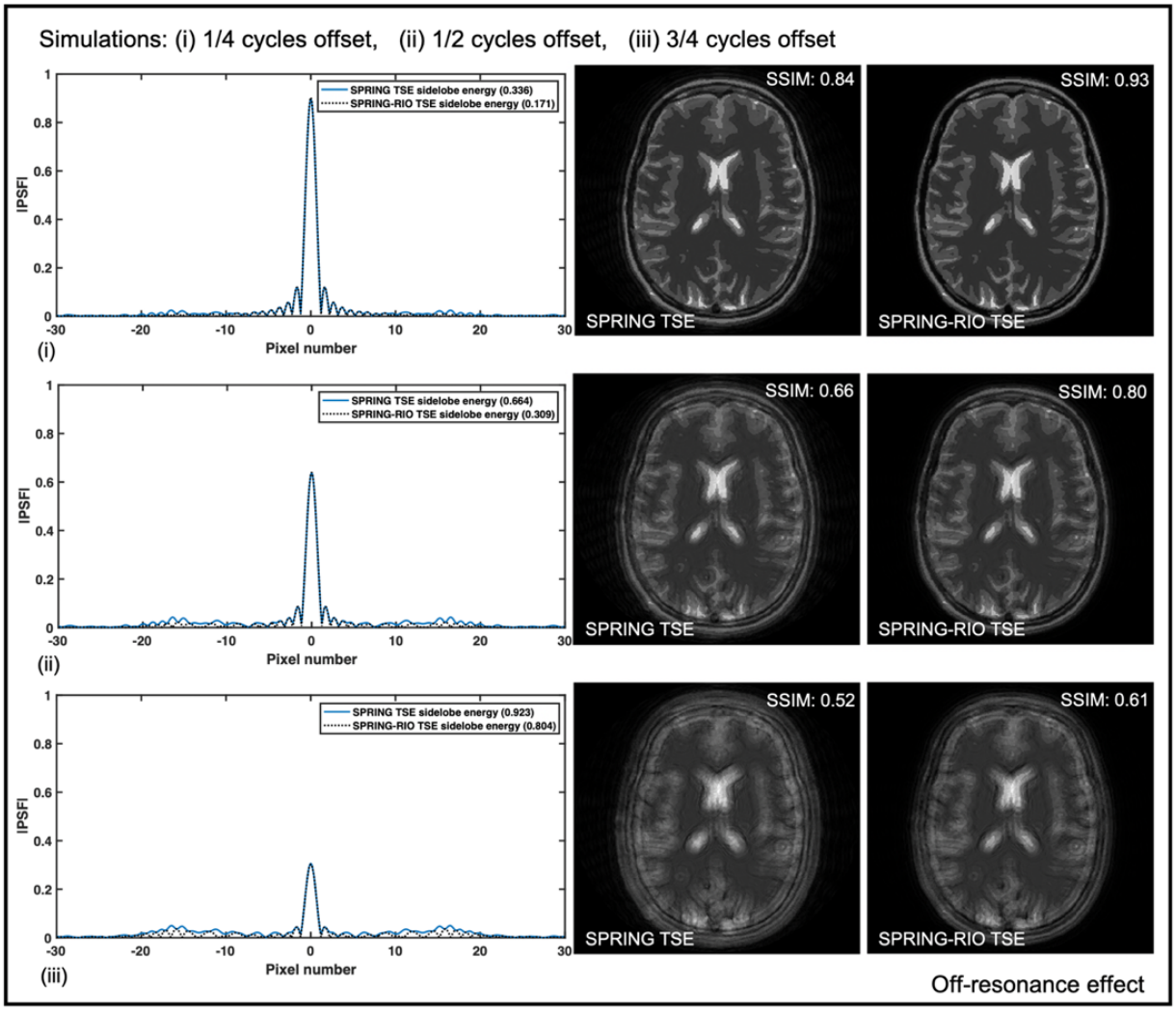

Figure 3-3. Simulation results of off-resonance effects for SPRING TSE and SPRING-RIO TSE. Off-resonance effects were simulated for three different amounts (1/4, 1/2, and 3/4 cycles) of phase accumulation. Central lines of the 2D PSF and the side lobe energy of PSFs were calculated for each sequence variation. The PSF results show the peak amplitudes of the main lobes for these two spiral-ring based TSE sequences decrease with increasing off-resonance frequency, causing signal loss yet without obvious loss in resolution. The digital brain image with no phase accumulation was used as the reference, and SSIM values were calculated between the reconstructed images of each sequence and the reference.

measured k-space trajectories. We observe that images with isotropic delay corrected k-space trajectories still show noticeable artifacts, mainly around edges, and shading and shape distortions. A slight distortion remaining in k-space trajectories (e.g., anisotropic delays and different eddy current terms on different physical gradient axes) would also cause significant artifacts. Improvements can be easily seen in Figure 3-6c,i when using a model-based estimated trajectory,

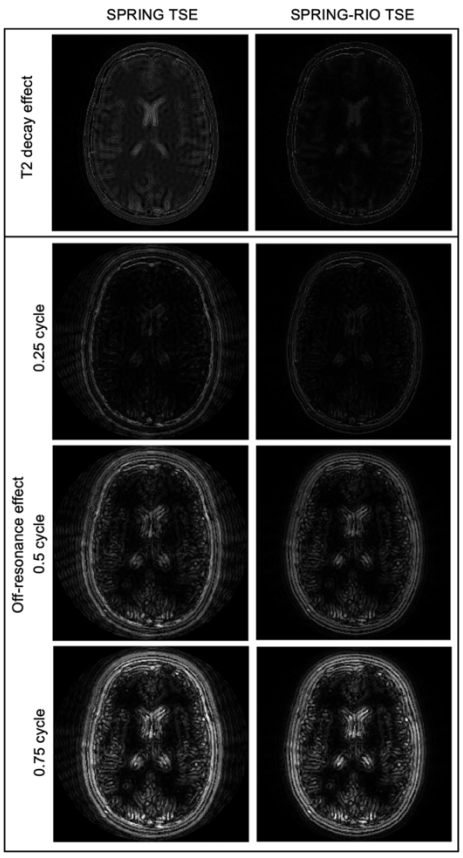

Figure 3-4 (Left)**.** Difference images between the SPRING TSE (left), SPRING-RIO TSE (right) and the reference. T2-decay effect with T2 = 70 ms (top) and off-resonance effect with a constant frequency offset of corresponding to 0.25, 0.5, and 0.75 cycles of phase (bottom) were simulated using a digital brain phantom.

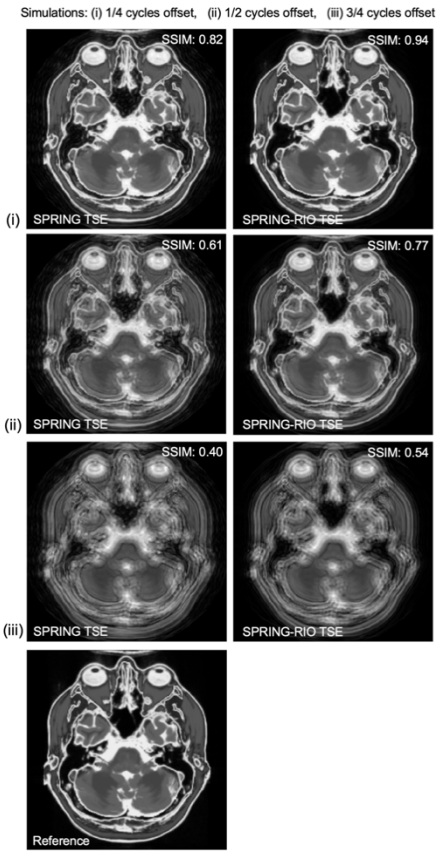

Figure 3-5 (Right)**.** Simulation results of one inferior slice with air/susceptibility from a digital brain phantom with off-resonance effects for SPRING TSE and SPRING-RIO TSE. The image (bottom) with no phase accumulation was used as the reference.

which removes most artifacts. Comparing difference images between SPRING TSE (Fig. 3-6d,e) and SPRING-RIO TSE (Fig. 3-6j,k) sequences, the SPRING-RIO TSE technique seems to be less sensitive to the gradient delays, most likely due to the time-reversed signal average between spiral-in and spiral-out rings which averages some shape distortions, although this has not been fully explored.

Figure 3-7 illustrates the efficacy of trajectory and off-resonance corrections for SPRING TSE versus SPRING-RIO TSE. The reduction of edge artifacts by using the model-based estimated trajectories for both of the spiral-ring sequences can be easily seen in Figure 3-7b,e from the zoomed portions of the images indicated by the boxes, when compared to the corresponding regions in Figure 3-7a,d. By further performing the aforementioned semiautomatic deblurring methods, both the artifacts and signal loss are significantly reduced in the fully corrected images

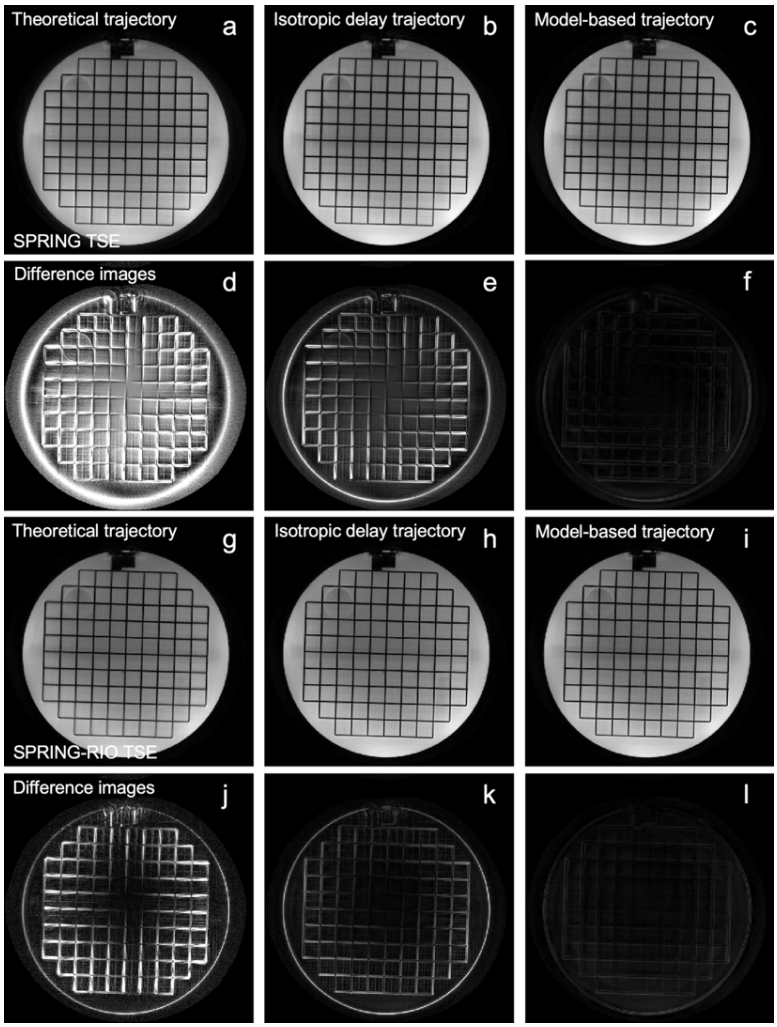

Figure 3-6. Reconstructed images of an axial slice in the resolution phantom from SPRING TSE (a-f) and SPRING-RIO TSE (g-l), and absolute difference images relative to the goal images based on measured k-space trajectories. The difference images are windowed to the same scale. a,g: Theoretical trajectory. b,h: Isotropic delay corrected trajectory. c,i: Model-based corrected trajectory. The second and fourth rows show the difference images between the trajectory type immediately above and the goal image (e.g., (d) shows the difference between image (a) and the goal image).

shown in Figure 3-7c,f. Comparing images between SPRING TSE (Fig. 3-7a-c) and SPRING-RIO TSE (Fig. 3-7d-f) sequences, images with higher SNR and improved sharpness can be seen for SPRING-RIO TSE, primarily due to the additional spiral-in rings acquired before the effective echo time. Further, in the presence of nonlinear B_0 variation, the uncorrected SPRING-RIO TSE sequence presents fewer image artifacts than an uncorrected SPRING TSE acquisition (Fig. 3-7b vs. 3-7e), thus demonstrating that the self-correcting RIO trajectory shows certain robustness to moderate off-resonance effects.

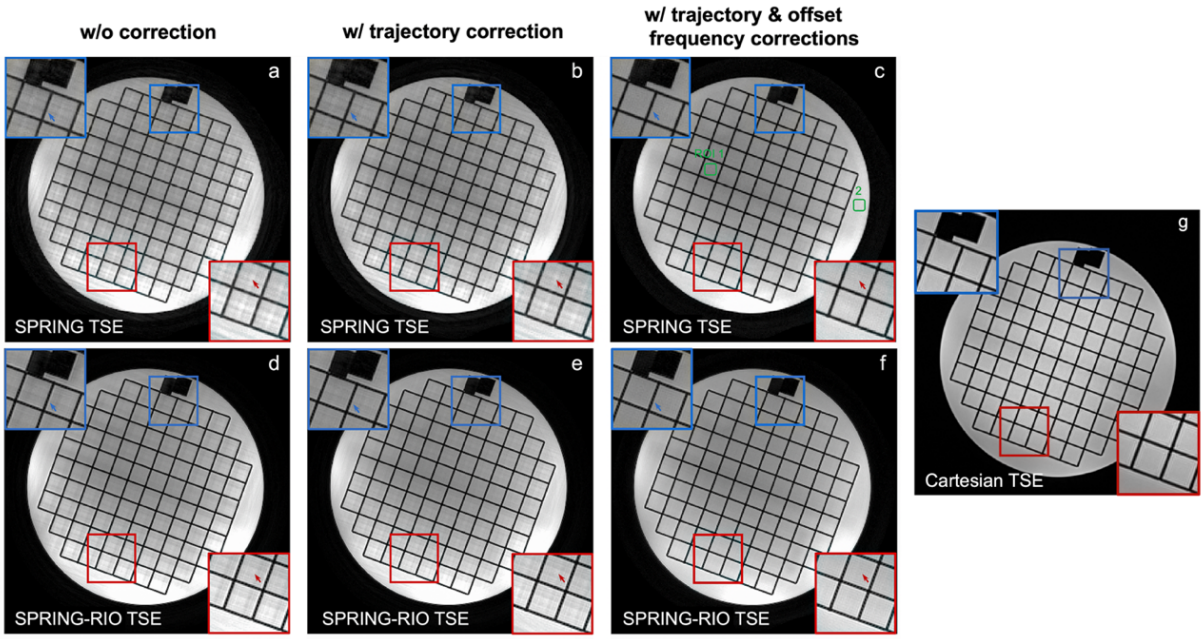

Figure 3-7. Performance of trajectory and off-resonance corrections, and of the RIO scheme. The portions of the phantom highlighted by the blue and red boxes illustrate that, without correction (a and d), noticeable artifacts around edges, shading, and strong off-resonance artifacts are present in the images. With trajectory correction (b and e), edge artifacts and shading are reduced (blue arrows). By further performing the off-resonance correction (c and f), artifacts and signal loss are significantly reduced (red arrows). Comparing images a–c and d–f, higher SNR (ROI 1: 49 versus 69, ROI 2: 73 versus 86), fewer residual artifacts, and improved sharpness can be seen for SPRING-RIO TSE (d–f) than for SPRING TSE (a-c). The image from Cartesian TSE (g) is shown for reference.

3.5.3 In vivo images

Figure 3-8 displays axial brain images acquired with SPRING TSE and SPRING-RIO TSE sequences, and reconstructed before and after off-resonance correction. The zoomed portions of the images on the left, before off-resonance correction, are consistent with simulation results and phantom studies, showing that artifacts caused by modest B_0 inhomogeneities can be reduced by the RIO design. The images in the right column demonstrate the efficacy of off-resonance correction. The SPRING-RIO TSE acquisition with semiautomatic off-resonance correction using a maximized energy objective function achieves overall better image quality than the SPRING TSE acquisition with semiautomatic off-resonance correction using a minimum phase objective function, in terms of SNR, residual artifacts, and image blurring.

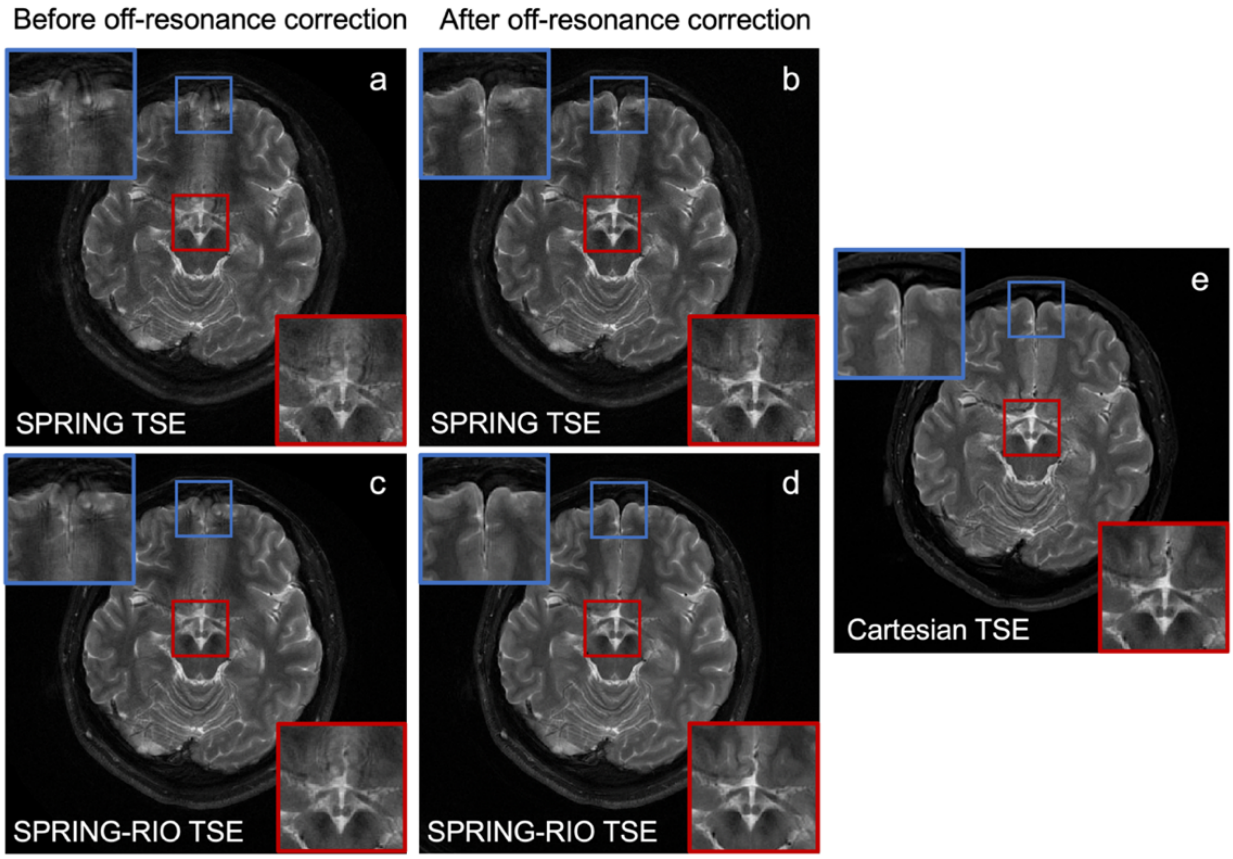

Figure 3-8. Comparison of axial brain images acquired with SPRING TSE (a, b) and SPRING-RIO TSE (c, d), and reconstructed before (a, c) and after off-resonance correction (b, d). The images in the right column demonstrate the efficacy of off-resonance correction. The SPRING-RIO TSE acquisition with semiautomatic off-resonance correction using maximized energy as a focusing criterion achieves overall better image quality than SPRING TSE acquisition with semiautomatic off-resonance correction using minimum phase as a focusing criterion. The image from Cartesian TSE (e) is shown for reference.

Axial, coronal, and sagittal brain images from SPRING TSE and SPRING-RIO TSE are shown in Figure 3-9. All the images are reconstructed using estimated trajectories and B_0 off-resonance corrections, and with two signal averages. Red arrows point to regions in the SPRING TSE brain images that show residual artifacts (presumably from off-resonance effects) even after correction, especially near air-tissue boundaries where the susceptibility gradients are relatively strong. Furthermore, we observe that compared to SPRING TSE, SPRING-RIO TSE produces sharper images with less T_2-decay induced blurring, as presented in some tissues with short T_2 values, such as skull and bone.

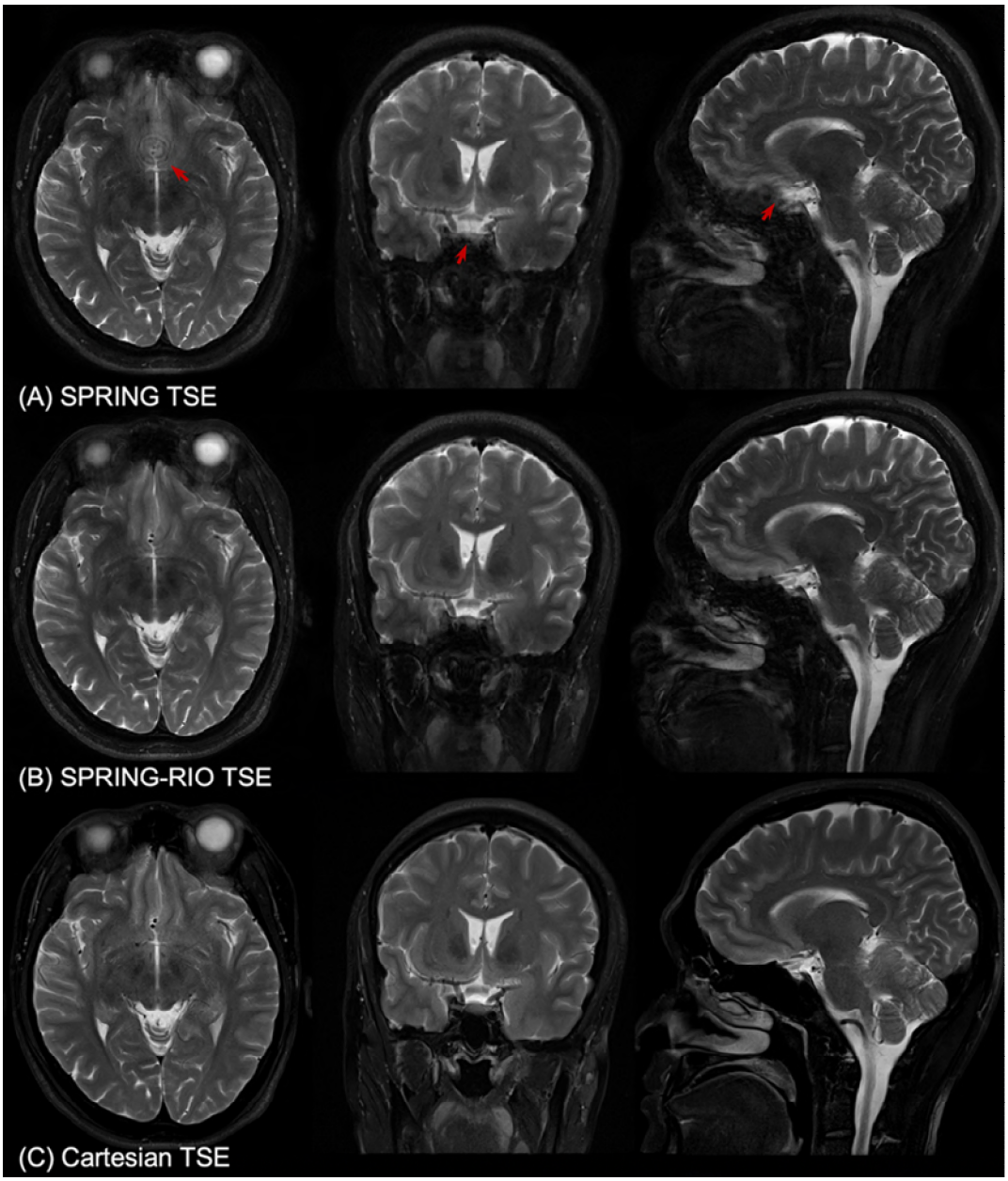

Figure 3-9. Comparison of trajectory- and off-resonance-corrected axial, coronal, and sagittal brain images from SPRING TSE (A) and SPRING-RIO TSE (B). The red arrows point to regions where SPRING-RIO TSE performs better than SPRING TSE, in terms of residual artifacts and image blurring. Tissues with short T_2 values, such as skull and bone, present sharper details in SPRING-RIO TSE than those in SPRING TSE. Images from Cartesian TSE (C) are shown at the bottom for reference.

Figure 3-10 shows a comparison of axial images acquired using the proposed SPRING-RIO TSE, with one signal average (top row) and with two signal averages (middle row), and standard Cartesian TSE (bottom row). No obvious artifacts are observed in the SPRING-RIO TSE

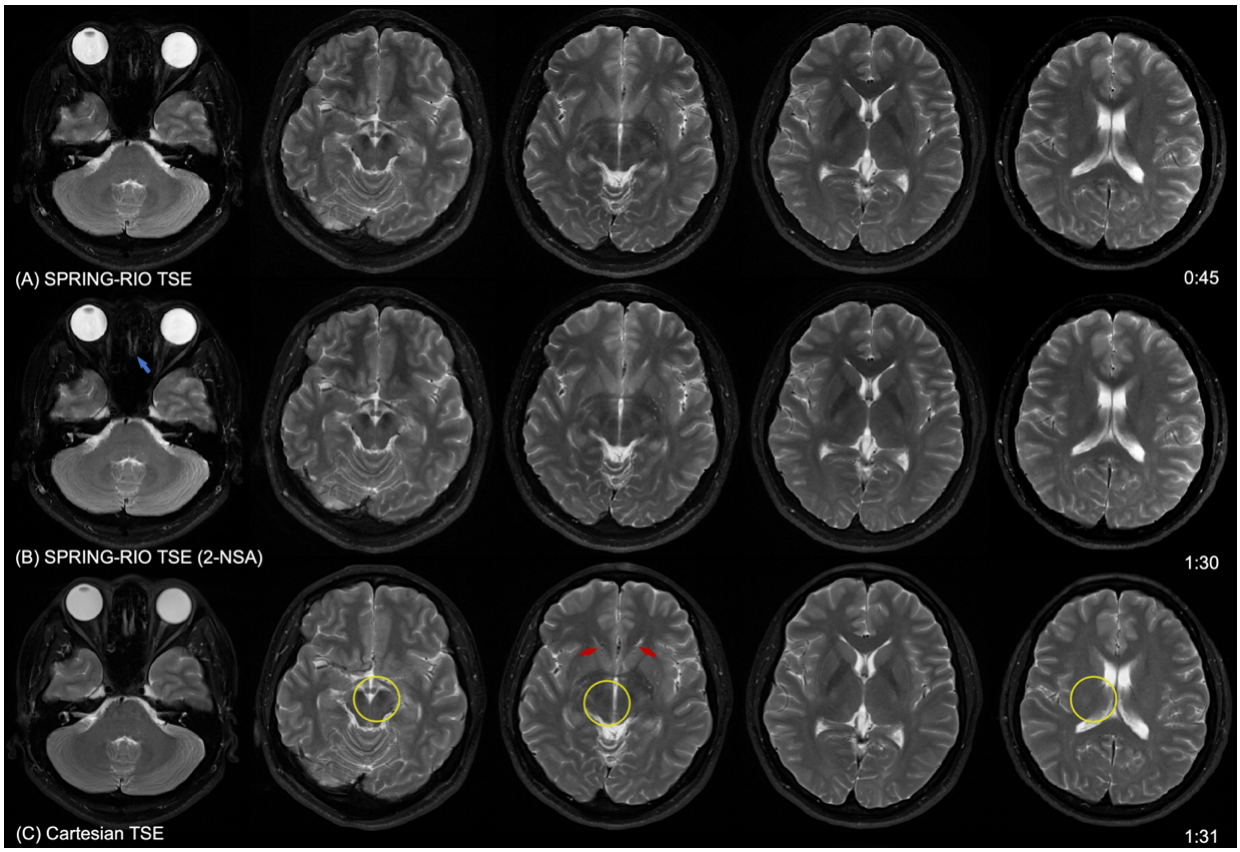

Figure 3-10. Comparison of in vivo axial images acquired using the proposed SPRING-RIO TSE method and standard Cartesian TSE. From top to bottom are corrected images from SPRING-RIO TSE with one signal average (A) and with two signal averages (B), and images from standard Cartesian TSE (C). The red arrows point to structures showing flow artifacts (left-right direction) from the anterior cerebral arteries in Cartesian TSE, while the blue arrow points to signal loss in SPRING-RIO TSE. The yellow circles indicate regions where the image contrast is better in SPRING-RIO TSE than in Cartesian TSE.

images. The results indicate that the image quality of SPRING-RIO TSE with 1-NSA is, in general, comparable to that of Cartesian TSE, yet with only half of the scan time that is used for Cartesian TSE. With 2-NSA, SPRING-RIO TSE shows a higher SNR, and that with both 1-NSA and 2-NSA show similar or slightly better contrast than the Cartesian counterpart in some areas indicated by the yellow circles, such as the dentate nuclei, substantial nigra, and red nuclei. This is also demonstrated by the measured SNR in WM and GM with SPRING-RIO TSE versus standard Cartesian TSE as shown in Figure 3-11, and image contrast between regions of iron deposition and surrounding tissue, and between GM and WM as shown in Figure 3-12.

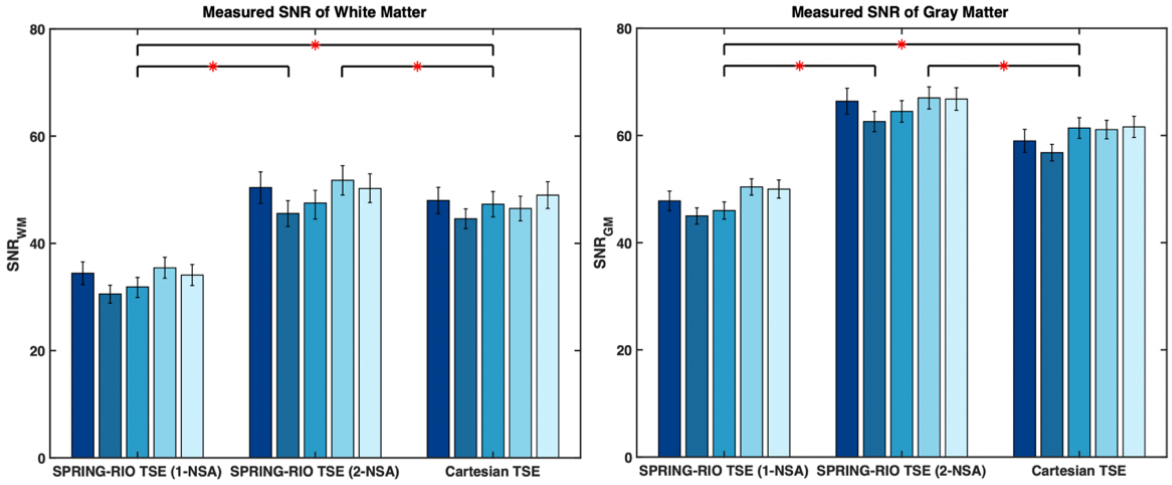

Figure 3-11. Measured SNR of ROIs in white matter (left) and gray matter (right) with SPRING-RIO TSE with one signal average (1-NSA), with two signal averages (2-NSA), and standard Cartesian TSE. The different bars for each method represent the values computed for five different volunteers. For each volunteer, ten slices are selected for SNR calculation, and thus pairwise comparisons among sequences are performed on a total of 50 pairs of SNR measurements. The asterisks indicate statistically significant differences between the methods ($P<0.05$). SPRING-RIO TSE (2-NSA) has the highest SNR in both white matter and gray matter.

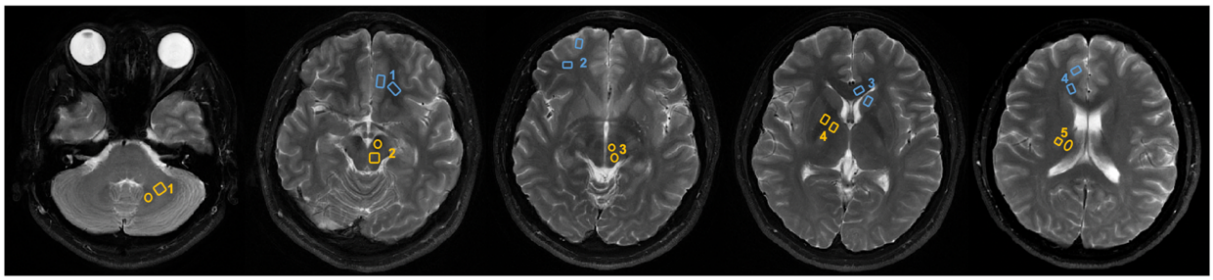

Measured Contrast (%)	Between regions with iron deposition and surrounding tissue					Between gray and white matter			
ROIs	1	2	3	4	5	1	2	3	4
SPRING-RIO TSE	23.5%	30.4%	29.3%	28.7%	23.2%	37.0%	34.8%	36.9%	35.6%
Cartesian TSE	15.9%	19.7%	17.2%	18.1%	14.2%	29.7%	30.6%	31.3%	30.1%

Figure 3-12. Measured contrast between RIOs. The first five groups (yellow regions 1~5) measure the contrast between the areas with iron deposition and the surrounding tissue. The next four groups (blue regions 1~4) measure the contrast between gray and white matter in the frontal lobe.

For the sagittal and coronal data sets shown in Figure 3-13, residual signal loss and artifacts can be seen in some areas where there are strong susceptibility gradients, and ghosting artifacts, potentially induced by concomitant fields, are observed in frontal lobes, as indicated by red arrows. Nonetheless, the overall image quality of SPRING-RIO TSE is comparable to that of Cartesian TSE, with improved contrast in areas with iron deposition (yellow circles).

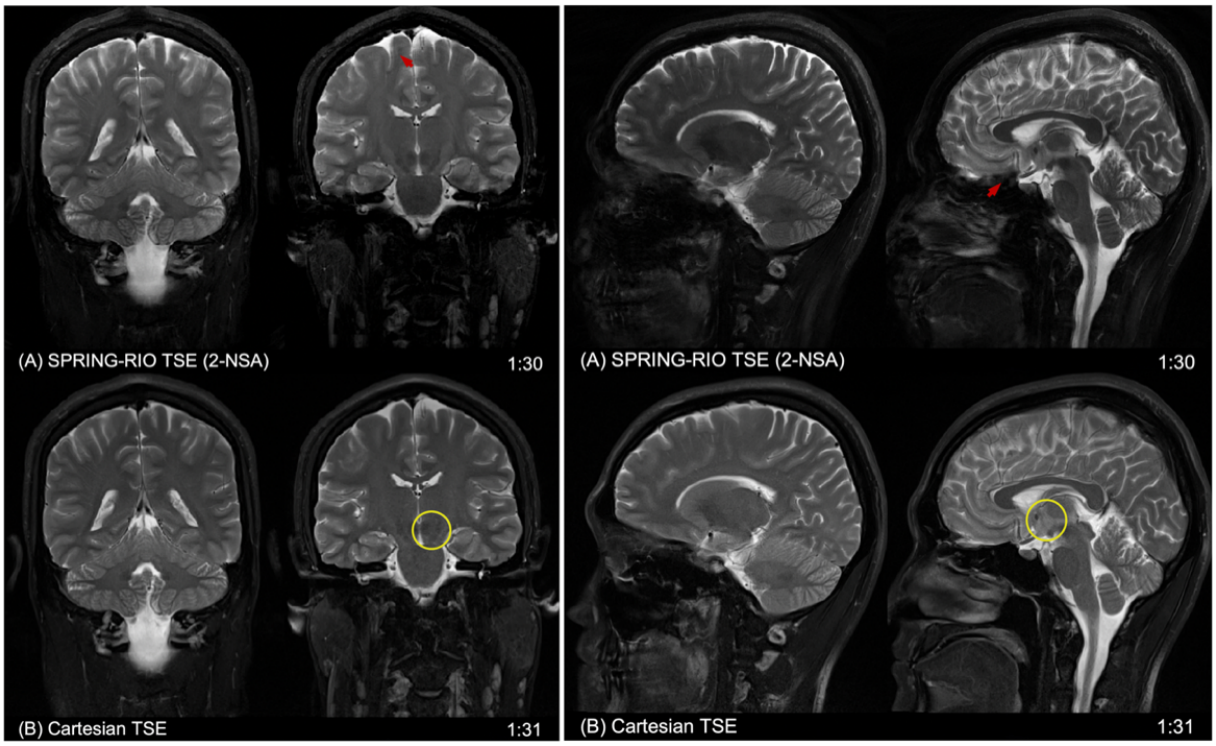

Figure 3-13. Comparison of in-vivo sagittal and coronal images acquired using the proposed SPRING-RIO TSE method and standard Cartesian TSE. The red arrows point to the structures where residual signal loss or artifacts exist, likely due to susceptibility or concomitant gradients. The yellow circles indicate areas where the image contrast is visually better in SPRING-RIO TSE than in Cartesian TSE.

3.6 Discussion

TSE echo trains provide a means for maintaining signal pathways over a long acquisition window (~200ms) using a series of high-flip-angle refocusing RF pulses. However, the specific absorption rate (SAR) limitations may restrict the protocol by limiting the number and the flip angle of refocusing RF pulses and the minimum spacing of the spin echoes, especially at high magnetic

field strengths. In a typical Cartesian TSE protocol, the refocusing flip angle is reduced to $\sim 150^{\circ}$ to mitigate the high SAR. For the SPRING-RIO TSE protocol used in this work, the refocusing flip angle was set to the same value as that used in Cartesian TSE, while the SAR from the set of refocusing RF pulses is approximately 86% of that from Cartesian TSE, primarily due to a higher k-space coverage per spin echo with a smaller number of echoes. Further reduction in SAR can be realized by optimizing the protocol. Flexibility exists to change the data acquisition time to allow a tradeoff between the echo train length and off-resonance artifact reduction. For a fixed set of parameters (e.g., FOV, in-plane spatial resolution, and total scan time), increasing the readout duration leads to a shorter echo train length, which results in a smaller number of refocusing RF pulses and thus a decreased SAR. For example, doubling the readout acquisition window from 7 ms to 14 ms results in an echo train length of 7, which would result in a SAR value that is approximately 47% of that from Cartesian TSE, if the same refocusing flip angle was used. The influence of reduced refocusing flip angles and ETL on image contrast is beyond the scope of this preliminary study; future clinical studies are needed to evaluate these impacts on image quality and contrast.

Imaging speed is an important metric, and fast scanning is one of the advantages that SPRING-RIO TSE provides. With the protocols used in this study, the minimum scan time of SPRING-RIO TSE is roughly half of that used in Cartesian TSE (0:45 min/14 slices versus 1:31 min/14 slices). Li et al.[8] proposed an alternative strategy to Cartesian TSE using an interleaved, rotated spiral-in/out readout along with a double-encoding method. However, the double-encoding method requires additional scan time, reducing the imaging speed by half, and it may be more sensitive to any motion/flow artifacts. An abstract describing an interleaved, split spiral in-out acquisition that alleviates T_2-decay effects without the need of a double-encoding was recently

reported in Ref 32. Although in this work we did not compare SPRING-RIO TSE to that technique, a future comparison of these two methods is planned. Our proposed method offers flexibility for fast scanning in tens of seconds, with a clinically acceptable SNR. Increasing the readout time (e.g., 10 ~ 15 ms) or using a longer ETL is feasible to improve scan efficiency, though it may induce stronger off-resonance effects or an increased RF SAR. Incorporating non-Cartesian parallel imaging techniques[33,34] can further accelerate the sampling speed, and it may be attractive for time-limited applications, such as breath-held single-shot abdominal imaging[35].

Gradient infidelity is one of the major concerns for reliable spiral readout imaging. The k-space trajectories can be measured and incorporated into reconstruction to improve image quality, yet it is impractical to do that for every imaging slice and each sequence parameter set. In our implementation, a model-based method that combines tuning the anisotropic delays on different gradient axes and eddy current compensation was used to estimate the actual k-space trajectories. The calculated system parameters can be used for later scans after a one-time gradient waveform calibration with no time penalty. This approach achieves good performance, as evidenced by the image quality of the phantom study.

Off-resonance induced phase error is another concern for spiral imaging, especially for a long acquisition window. As observed from in vivo results, effective deblurring was accomplished in the majority of the images. The performance is sometimes suboptimal in two scenarios: (1) in areas with low amplitude or little contrast, such as in nearly uniform regions; and (2) if a local field fluctuates too rapidly, the objective function surface will produce erroneous extrema, because the conjugate phase reconstruction assumes a spatially smooth and temporally constant field map. This typically produces errors in areas around the sinus, nasal cavity, and mouth, where the anatomical structures in the spiral images are not as clean as those in the Cartesian images.

Although a modest readout duration was used in this work to avoid large B_0-field induced phase accruals, and the affected areas are of little clinical significance, future work will optimize the deblurring method to deal with these challenges.

Concomitant (Maxwell) fields may cause phase errors as well, especially for spiral-based TSE sequences, since spiral waveforms vary along the echo train, which may disturb the spin echo train[36,37]. Although Maxwell terms scale inversely with the field strength, and concomitant gradient effects decrease as the field strength increases, we still see a potential source of Maxwell field induced artifacts at 3 T from SPRING-RIO TSE in coronal and sagittal planes and off-center slices. This work did not include concomitant-gradient compensation; however, there are several correction methods for spiral TSE via gradient waveform redesign and/or phase correction during reconstruction.[8,36-39] For example, the gradient waveform modifications presented by Mugler et al.[39] have been incorporated into interleaved, rotated spiral TSE imaging with different trajectory types, and promising results show a substantial reduction in degradation associated with self-squared Maxwell gradient effects at a low magnetic field strength (0.55 T). In the next chapter, we will describe approaches for SPRING-RIO TSE sequence to reduce the phase shifts at echoes and maintain the CPMG condition over echo spacings by sequence modifications and image reconstruction.

With a retraced in/out strategy, there is less flexibility to arbitrarily set the number of spiral rings, ETL, and FOV for a given resolution while targeting the desired TE because of their interdependencies. However, a target TE can still be approximately achieved by adjusting these imaging parameters and utilizing early echoes before the effective TE. For example, short-TE images can be acquired by simply dropping 1-2 spiral-in rings at the beginning with slightly reduced high frequency information.

3.7 Conclusion

In this chapter, we demonstrated that using annular spiral rings with a retraced in/out trajectory is a viable data acquisition method that can be incorporated into 2D TSE echo trains to efficiently suppress T_2-decay effects. With trajectory-fidelity and off-resonance corrections, this approach provides a potential alternative to Cartesian TSE for T_2-weighted neuroimaging, with high scan efficiency, low SAR, and improved image contrast.

3.8 Appendix

3.8.1 Part A

The received MR signal of a spiral-out ring for the j^{th} k-space segment acquired at the p^{th} echo can be modeled for $t \in [-\frac{T}{2}, \frac{T}{2}]$ as

$$s_{j,p}(t) = \int m(\boldsymbol{r}) e^{-i2\pi \boldsymbol{k_{j,p}}(t)\boldsymbol{r}} e^{-i\omega(r)t} e^{-(t+T_p)/T_2} d\boldsymbol{r}, \tag{3-12}$$

where T is the readout time, and $m(\boldsymbol{r})$ is the object's complex-valued magnetization. $\omega(\boldsymbol{r})$ is defined as the spatially varying resonant frequency of the object. T_p refers to the time interval between the excitation RF pulse and the center of the readout window at p^{th} echo, where $0 \leq p \leq L$, and L is the total number of spiral-out rings.

Using the similar substitution, the received MR signal of a second acquisition from a spiral-in ring for the same j^{th} k-space segment but acquired at the q^{th} echo can be derived as, for $t' \in [-\frac{T}{2}, \frac{T}{2}]$:

$$s_{j,q}(t') = \int m(\boldsymbol{r}) e^{-i2\pi \boldsymbol{k_{j,q}}(t')\boldsymbol{r}} e^{-i\omega(r)t'} e^{-(t'+T_q)/T_2} d\boldsymbol{r}, \tag{3-13}$$

where T_q refers to the time interval between the excitation RF pulse and the center of the readout window at q^{th} echo, and $-L+1 \leq q \leq 0$.

For retraced in-out trajectories, a few properties of the k-space trajectory must be defined. First, each ring segment has duration T, and each pair of the two retraced rings are anti-symmetric about the echo time such that

$$T_p + T_q = 2\,TE. \tag{3-14}$$

Then, we can constrain the ring trajectories to be time-reversed copies of each other as

$$\boldsymbol{k_{j,p}}(t) = \boldsymbol{k_{j,q}}(-t) = -\boldsymbol{k_{j,q}}(t). \tag{3-15}$$

The central self-retraced spiral in-out segment can be considered as a special case when $p = q = 0$. We can also define ΔT in terms of T_p, T_q as

$$\Delta T = T_p - T_q. \tag{3-16}$$

Assuming each readout in the TSE echo train is short relative to the T_2 relaxation, we can write that

$$e^{\frac{-T}{T_2}} \approx 1. \tag{3-17}$$

Before we can combine $s_{j,p}$ with $s_{j,q}$, we must time-reverse $s_{j,q}$ since the second spiral-in acquisition is run in the opposite direction through k-space. Let $t = -t'$, we can get

$$s_{j,q}(-t) = \int m(\boldsymbol{r}) e^{-i2\pi \boldsymbol{k_{j,q}}(-t)\boldsymbol{r}} e^{-i\omega(\boldsymbol{r})(-t)} e^{-(-t+T_q)/T_2} d\boldsymbol{r}. \tag{3-18}$$

Using all the above assumptions, $s_{j,q}(-t_2)$ can be written as

$$s_{j,q}(-t) \approx \int m(\boldsymbol{r}) e^{-i2\pi \boldsymbol{k_{j,p}}(t)\boldsymbol{r}} e^{i\omega(\boldsymbol{r})t} e^{-(T_p-\Delta T)/T_2} d\boldsymbol{r}. \tag{3-19}$$

Now, the combination of the two signals can be written as

$$s(t) = \frac{s_{j,p}(t)+s_{j,q}(-t)}{2} = \frac{1}{2}\int M(\boldsymbol{r})e^{-i2\pi \boldsymbol{k_{j,p}}(t)\boldsymbol{r}}e^{-\frac{Tp}{T_2}}\left[e^{-i\omega(\boldsymbol{r})t} + e^{i\omega(\boldsymbol{r})t}e^{+\frac{\Delta T}{T_2}}\right]dr. \quad (3\text{-}20)$$

To simplify more, we can get

$$s(t) = \frac{1}{2}\int M(\boldsymbol{r})e^{-i2\pi \boldsymbol{k_{j,p}}(t)\boldsymbol{r}}e^{\frac{-(T_p-\frac{\Delta T}{2})}{T_2}}\left[e^{-i\omega(\boldsymbol{r})t}e^{-\frac{\Delta T}{2T_2}} + e^{i\omega(\boldsymbol{r})t}e^{\frac{\Delta T}{2T_2}}\right]dr. \quad (3\text{-}21)$$

For the next step, substitute the terms $e^{i\omega(\boldsymbol{r})t} = \cos[\omega(\boldsymbol{r})t] + isin[\omega(\boldsymbol{r})t]$, $e^{\frac{\Delta T}{2T_2}} = \cosh\left(\frac{\Delta T}{2T_2}\right) + \sinh\left(\frac{\Delta T}{2T_2}\right)$, $e^{\frac{-\Delta T}{2T_2}} = \cosh\left(\frac{\Delta T}{2T_2}\right) - \sinh\left(\frac{\Delta T}{2T_2}\right)$, $T_p - \frac{\Delta T}{2} = TE$, and $\frac{\Delta T}{2} = T_p - TE$. Multiplying out the terms in the brackets, we can get

$$s(t) = \int m(\boldsymbol{r})e^{-i2\pi \boldsymbol{k_{j,p}}(t)\boldsymbol{r}}e^{\frac{-TE}{T_2}}\left[\cos[\omega(\boldsymbol{r})t]\cosh\left(\frac{T_p-TE}{T_2}\right) isin[\omega(\boldsymbol{r})t]\sinh\left(\frac{T_p-TE}{T_2}\right)\right]\boldsymbol{dr}. \quad (3\text{-}22)$$

The equation above describes the magnitude and phase modulation of the combination of the signals collected from SPRING-RIO TSE due to the off-resonance effect during the readout window and T_2-decay effect along the echo train.

3.8.2 Part B

We extend the original signal equation to conjugate phase reconstruction. Let

$$\tilde{s}(t;\omega_i(\boldsymbol{r})) = \frac{s_{j,p}(t)e^{i\omega_i(r)t}+s_{j,q}(-t)e^{-i\omega_i(r)t}}{2}. \quad (3\text{-}23)$$

In this case, each ring trajectory is demodulated at frequency ω_i, and the time reversal of $s_{j,q}$ produces a demodulation term that is the complex conjugate of that applied to $s_{j,p}$. To evaluate $\tilde{s}(t;\omega_i(\boldsymbol{r}))$ for a point object at location $\boldsymbol{r_o}$,

$$\tilde{s}(t;\omega_i)|_{r_o} = e^{-i2\pi \boldsymbol{k_{j,p}}(t)\boldsymbol{r_0}} \cdot e^{\frac{-TE}{T_2}} \left[\cos\{[\omega(\boldsymbol{r_0}) - \omega_i]t\} \cosh\left(\frac{T_p - TE}{T_2}\right) + isin\{[\omega(\boldsymbol{r_0}) - \omega_i]t\} \sinh\left(\frac{T_p - TE}{T_2}\right)\right]. \quad (3\text{-}24)$$

We then multiply $\tilde{s}(t;\omega_i)$ by its complex conjugate and substitute $cosh^2(x) = 1 + sinh^2(x)$ to yield

$$\tilde{s}(t;\omega_i)|_{r_o} \tilde{s}(t;\omega_i)|_{r_o}{}^* = e^{\frac{-TE}{T_2}} \left[cos^2\{[\omega(\boldsymbol{r_0}) - \omega_i]t\} + sinh^2\left(\frac{T_p - TE}{T_2}\right)\right]. \quad (3\text{-}25)$$

The $cos^2\{[\omega(\boldsymbol{r_0}) - \omega_i]t\}$ term attenuates the distribution of energy across the k-space trajectory for any $\omega_i \neq \omega(\boldsymbol{r_0})$. By invoking Parseval's theorem, the integrated squared magnitude of the PSF is maximized at $\omega_i = \omega(\boldsymbol{r_0})$ for given sequence parameters. This final set shows that the magnitude modulation of the k-space energy caused by off-resonance is independent of T_2-decay and incidental image phase.

3.9 References

1. Hennig J, Nauerth A, Friedburg H. RARE imaging: a fast imaging method for clinical MR. *Magn Reson Med*. 1986; 3:823-833.
2. Busse RF, Hariharan H, Vu A, Brittain JH. Fast spin echo sequences with very long echo trains: design of variable refocusing flip angle schedules and generation of clinical T_2 contrast. *Magn Reson Med*. 2006; 55:1030-1037.
3. Mugler JP III. Optimized three-dimensional fast-spin-echo MRI. *J Magn Reson Imaging*. 2014; 39:745-767.
4. Zhou X, Liang ZP, Cofer GP, Beaulieu CF, Suddarth SA, Johnson GA. Reduction of ringing and blurring artifacts in fast spin-echo imaging. *J Magn Reson Imaging*. 1993; 3:803–807.
5. Takahashi H, Ogawa K, Oshio K, Momoshima H. A proposal of removal method for T_2 decay effects in RARE sequence. *IEEE Trans Nucl Sci.* 1995; 42:1343–1347.

6. Constable RT, Anderson AW, Zhong J, Gore JC. Factors influencing contrast in fast spin-echo MR imaging. *Magn Reson Imaging*. 1992; 10:497-511.

7. Meyer CH, Hu BS, Nishimura DG, Macovski A. Fast spiral coronary artery imaging. *Magn Reson Med*. 1992; 28:202-213.

8. Li Z, Karis JP, Pipe JG. A 2D spiral turbo-spin-echo technique. *Magn Reson Med*. 2018; 80:1989–1996.

9. Block W, Pauly J, Nishimura D. RARE spiral T_2-weighted imaging. *Magn Reson Med*. 1997; 37:582–590.

10. Hennig J, Menza M, Barghoorn A, Riemenschneider B, Kroboth S, Zaitsev M. Spiral RARE with annular segmentation. In Proceedings of the 27th Annual Meeting of ISMRM, Montreal, Quebec, Canada, 2019. p. 4632.

11. Wang Z, Allen S, Feng X, Mugler JP, Meyer CH. SPRING TSE: 2D T_2-Weighted Brain Imaging using SPiral RING Turbo Spin-Echo. In Proceedings of the 28th Annual Meeting of ISMRM, Virtual Conference, 2020. p. 3714.

12. Wang Z, Allen S, Feng X, Mugler JP, Meyer CH. SPRING-RIO TSE: 2D T_2-Weighted Turbo Spin-Echo Brain Imaging using SPiral RINGs with Retraced In/Out Trajectories. In Proceedings of the 29th Annual Meeting of ISMRM, Virtual Conference, 2021. p. 0837.

13. Wang Z, Feng X, Mugler JP, Meyer CH. Rapid and Simultaneous Acquisition of T2-weighted and Fluid-attenuated Brain Images using a Spiral-ring Turbo Spin-echo Imaging. Proceedings of the ISMRM 29th Annual Meeting, Virtual Conference, 2021. p. 1247.

14. Fielden SW, Meyer CH. A simple acquisition strategy to avoid off-resonance blurring in spiral imaging with redundant spiral-in/out k-space trajectories. *Magn Reson Med*. 2015; 73:704–710.

15. Bernstein MA, King KF, Zhou X. *Handbook of MRI pulse sequences*. Elsevier: Burlington, MA, 2004.

16. Meyer CH, Pauly JM, Macovski A. A rapid, graphical method for optimal spiral gradient design. In Proceedings of the 4th Annual Meeting of ISMRM, New York, 1996. p. 392.

17. Ding X, Tach J, Ruggieri P, Perl J, Masaryk T. Improvement of spiral MRI with the measured k-space trajectory. *J Magn Reson lmag*. 1997;7: 938 –940.

18. Tan H, Meyer CH. Estimation of k-space trajectories in spiral MRI. *Magn Reson Med*. 2009; 61:1396–1404.

19. Feng X, Salerno M, Kramer C M, Meyer CH. Non-Cartesian balanced steady-state free precession pulse sequences for real-time cardiac MRI. *Magn Reson Med*. 2016;75(4):1546.

20. Duyn JH, Yang Y, Frank JA, van der Veen JW. Simple correction method for k-space trajectory deviations in MRI. *J Magn Reson*. 1998; 132:150 –153.

21. Wang Z, Bovik AC, Sheikh HR, Simmoncelli EP. Image quality assessment: from error visibility to structural similarity. *IEEE Trans Image Process*. 2004; 13:600–612.

22. Fessler A Jeffrey, "Michigan Image Reconstruction Toolbox," available at http://web.eecs.umich.edu/~fessler/irt/fessler.tgz.

23. Uecker M, Lai P, Murphy MJ, Virtue P, Elad M, Pauly JM, Vasanawala SS, Lustig M. ESPIRiT–an eigenvalue approach to auto-calibrating parallel MRI: where SENSE meets GRAPPA. *Magn Reson Med*. 2014; 71:990–1001.

24. Noll DC, Meyer CH, Pauly JM, Nishimura DG, Macovski A. A homogeneity correction method for magnetic resonance imaging with time-varying gradients. *IEEE Trans Med Imaging*. 1991; 10:629–637.

25. Irarrazabal P, Meyer CH, Nishimura DG, Macovski A. Inhomogeneity correction using an estimated linear field map. *Magn Reson Med*. 1996; 35:278–282.

26. Man LC, Pauly JM, Macovski A. Multifrequency interpolation for fast off-resonance correction. *Magn Reson Med*. 1997; 37:785–792.

27. Sutton BP, Noll DC, Fessler JA. Fast, iterative image reconstruction for MRI in the presence of field inhomogeneities. *IEEE Trans Med Imaging*. 2003; 22:178–188.

28. Noll DC, Pauly JM, Meyer CH, Nishimura DG, Macovski A. Deblurring for non-2D fourier transform magnetic resonance imaging. *Magn Reson Med*. 1992; 25:319–333.

29. Man LC, Pauly JM, Macovski A. Improved automatic off-resonance correction without a field map in spiral imaging. *Magn Reson Med*. 1997; 37:906–913.

30. Chen W, Meyer CH. Semiautomatic off-resonance correction in spiral imaging. *Magn Reson Med*. 2008; 59:1212–1219.

31. Allen SP, Feng X, Fielden SW, Meyer CH. Correcting image blur in spiral, retraced in/out (RIO) acquisitions using a maximized energy objective. *Magn Reson Med*. 2019; 81:1806–1817.

32. Peng X, Borup D, Pipe JG. Accelerated Spiral Turbo-Spin-Echo Sequence with Split Spiral In-out Acquisition. In Proceedings of the 29th Annual Meeting of ISMRM, Virtual Conference, 2021. p. 4185.

33. Pruessmann KP, Weiger M, Bornert P, Boesiger P. Advances in sensitivity encoding with arbitrary k-space trajectories. *Magn Reson Med*. 2001; 46:638–651.

34. Lustig M, Pauly JM. SPIRiT: iterative self-consistent parallel imaging reconstruction from arbitrary k-space. *Magn Reson Med*. 2010; 64:457– 471.

35. Semelka RC, Kelekis NL, Thomasson D, Brown MA, Laub GA. HASTE MR imaging: description of technique and preliminary results in the abdomen. *J Magn Reson Imaging*. 1996; 6: 698– 699.

36. Zhou XJ, Tan SG, Bernstein MA. Artifacts induced by concomitant magnetic field in fast spin-echo imaging. *Magn Reson Med*. 1998; 40:582-591.

37. King KF, Ganin A, Zhou XJ, Bernstein MA. Concomitant gradient field effects in spiral scans. *Magn Reson Med*. 1999;41:103–112.

38. Chen W, Sica CT, Meyer CH. Fast conjugate phase image reconstruction based on a Chebyshev approximation to correct for B_0 field inhomogeneity and concomitant gradients. *Magn Reson Med*. 2008; 60:1104–1111.

39. Mugler JP, Campbell-Washburn AE, Ramasawmy R, Pfeuffer J, Meyer, CH. Maxwell Compensation for Spiral Turbo-Spin-Echo Imaging. In Proceedings of the 29th Annual Meeting of ISMRM, Virtual Conference, 2021. p. 0003.

Chapter 4: Concomitant magnetic-field compensation for 2D spiral-ring turbo-spin-echo imaging at 0.55 T and 1.5 T

4.1 Introduction

In Chapter 3, we introduced 2D spiral-ring turbo-spin-echo imaging for fast T_2-weighted brain imaging at 3 T and mainly discussed off-resonance correction of B_0 inhomogeneities. Another important source of off-resonance existing in spiral imaging is concomitant magnetic fields[1-5]. In this chapter, we will focus on the mathematical analysis and correction strategies of concomitant field effects for 2D spiral-ring TSE.

TSE acquisition is sensitive to any inconsistent phase errors induced by system imperfections (e.g., eddy currents, concomitant fields) among echo signals, limiting its use for obtaining high quality T_2-weighted images.[6,7] Since the gradients used for imaging inevitably generate concomitant fields, which scale quadratically with gradient amplitude, compensation for them becomes increasingly important for TSE when using readouts with high gradient amplitude (> 20 mT/m). There has recently been renewed interest in MRI at lower magnetic field strengths (< 1 T)[8,9], where these effects are increased because concomitant fields scale inversely with the field strength, and thus the phase errors induced by concomitant gradients increase. As depicted in Chapter 2, concomitant gradient effects in Cartesian TSE have been well described, and several strategies have been developed, for example as described by Zhou et al.[2], to eliminate or minimize the associated image degradation.

Imaging with prolonged readouts such as spiral acquisitions at low fields have recently shown benefits in regaining SNR using a high-performance MR scanner at 0.55 T[8-12], because off-

resonance effects decrease as field strength decreases. Therefore, a potentially important application area for spiral TSE is low field imaging. However, spiral TSE imaging[13-15] presents challenges for compensating concomitant gradient effects, since the spiral readouts vary along the echo train as compared to Cartesian TSE, where the same readout waveform is used for every echo. Hence, concomitant field phase errors induced by differences in spiral readouts along the echo train may disturb the TSE signal pathway and violate the Carr-Purcell-Meiboom-Gill (CPMG) condition[16], resulting in severe signal loss and image blurring which cannot be fully corrected in image reconstruction. Researchers have investigated concomitant gradient compensation for interleaved, time-symmetric spiral-in/out TSE imaging[15,17], and recently Mugler et al.[18] redesigned the pulse sequence to achieve compensation of self-squared Maxwell field terms by modifying gradient waveforms along the entire echo train for 2D T_2-weighted interleaved, rotated spiral-arm TSE imaging with several trajectory types (spiral-out, -in, or -in/out). Promising results showed that this approach provided substantial improvement in image quality at 0.55 T by reducing or eliminating degradation associated with self-squared concomitant gradient effects.

Our previous work proposed an alternative approach to 2D TSE imaging using annular spiral rings with a retraced in/out trajectory, dubbed "SPRING-RIO TSE[13]", for fast T_2-weighted brain imaging at 3 T. Compared to the interleaved, rotated spiral-arm segmentation which requires a double-encoding strategy, annular spiral-ring segmentation inserts several annular segments into TSE echoes, with the benefit of reduced T_2-decay artifacts by converting the T_2-dependent signal modulation into a k-space apodizing filter.[13,19-21] Since spiral-ring waveforms for each echo along the echo train vary along the echo train and are temporally asymmetric, the concomitant field effects on images from SPRING-RIO TSE at relatively low-field strength become non-negligible and must be corrected.

Building on the previous work, this chapter proposes a general method that incorporates both pulse sequence design and image reconstruction methods to compensate for concomitant field effects in SPRING-RIO TSE.[22] First, we introduce strategies for gradient waveform modifications to compensate for the self-squared Maxwell terms at the echo time and between echo spacings. Second, we describe image reconstruction methods to correct for residual concomitant fields and B_0 inhomogeneity induced phase accruals along the readout. Finally, we validate the feasibility of the proposed techniques and compare its performance to that of SPRING-RIO TSE with no concomitant field compensation and Cartesian TSE in phantom and in vivo scans at both 0.55 T and 1.5 T.

4.2 Concomitant field corrections

The mathematical description of Maxwell fields B_c and the corresponding accumulated phase terms in signal equation has been described in Chapter 2. To produce high quality spiral-ring TSE images at 0.55 T and 1.5 T, the concomitant field induced phase error must be eliminated or mitigated to a negligible level. In this section, we present several strategies to substantially reduce the phase errors in SPRING-RIO TSE via both pulse sequence modifications and the image reconstruction process.

4.2.1 Sequence-based corrections

The goal of gradient waveform modifications is to eliminate the phase shift from self-squared terms at the k-space center, and to reduce the difference in phase shifts among echoes, targeting a constant phase shift at the end of every echo. For any arbitrary gradient $g'(t)$, its waveform can be decomposed into three orthogonal gradient components $\{g'_x(t), g'_y(t), g'_z(t)\}$, and the

concomitant field integral $M = \{M_x, M_y, M_z\}$ of each component from self-squared terms can be calculated as:

$$M = \left\{ \int (g'_x(t'))^2 dt' , \int (g'_y(t'))^2 dt', \int (\frac{g'_z(t')}{2})^2 dt' \right\}, \quad (4\text{-}1)$$

For a single spatial location $\boldsymbol{r}_0$, the phase error from the self-squared terms induced by the concomitant field can be determined by its concomitant field integral M.

In SPRING-RIO TSE, the data were collected by self-retraced spiral in-out rings for the center of k-space, spiral-out rings at the end of the echo train paired with time-reversed, spiral-in rings with opposite gradient polarity at the beginning of the echo train for the outer portion of k-space. Therefore, the implementation of sequence in Figure 4-1 was accomplished as follows:

1. The gradient waveform reshaping strategy, as described in Ref 2, was used to simultaneously nullify both the linear and the quadratic phase induced by encoding gradients and their concomitant gradients, respectively. In this work, the left crusher gradient of the first refocusing RF pulse (green dashed box) was redesigned to correct for echo-to-echo phase variations from self-squared terms produced by the slice selection gradients/crushers.
2. For each excitation (shot), the maximum concomitant field integral M_{max} from self-squared terms for each readout gradient axis was determined from the spiral-ring with the highest gradient amplitude (see Figure 4-2).
3. Bipolar gradient pairs were added at both the beginning and the end of each remaining echo spacing (i.e., two pairs for each axis) to increase the concomitant field integrals for each gradient axis. The gradient amplitudes and durations of the added bipolar pairs for each echo were determined by subtraction of the concomitant field integral M_j for the current j^{th}

spiral ring from M_{max}, while those of the bipolar pairs placed at the interval between the excitation RF pulse and the first refocusing RF pulse were determined by $\frac{M_{max}}{2}$.

4. The gradient polarity of one of the four bipolar pairs in each echo spacing was set to be the opposite of the others (Figure 4-1B) for self-balancing quadratic cross-terms induced by added bipolar pairs themselves. The benefits of this strategy compared to that without the gradient polarity reversal (Figure 4-1A) will be discussed in the following sections.
5. Additional time was added to each echo spacing as needed to achieve compensation, and the final concomitant integral at the end of each echo spacing was designed to be a constant value of $\frac{M_{max}}{2}$. In this work, 5 ms of additional time (2.5 ms before and after each readout) was added for bipolar gradient pairs. This additional time was also added to SPRING-RIO TSE with no compensation for comparison to that with sequenced-based concomitant field corrections.

4.2.2 Reconstruction-based corrections

The goal of the image reconstruction method is to further reduce the residual phase errors from concomitant gradients and B_0 off-resonance effects accrued during the readout. As reported in Ref 3, for spiral scanning, the concomitant gradient phase accruals along the acquisition window were approximated from the lowest order Maxwell gradients for arbitrary scan plane orientation as follows:

$$\phi_c(\Delta\omega_c(\boldsymbol{r}), t) = \Delta\omega_c(\boldsymbol{r})\, t_c, \tag{4-2}$$

with

$$\Delta\omega_c(\boldsymbol{r}) = \gamma \frac{g_m^2}{4B_0}(F_1X^2 + F_2Y^2 + F_3Z^2 + F_4XZ + F_5YZ + F_6XY), \tag{4-3}$$

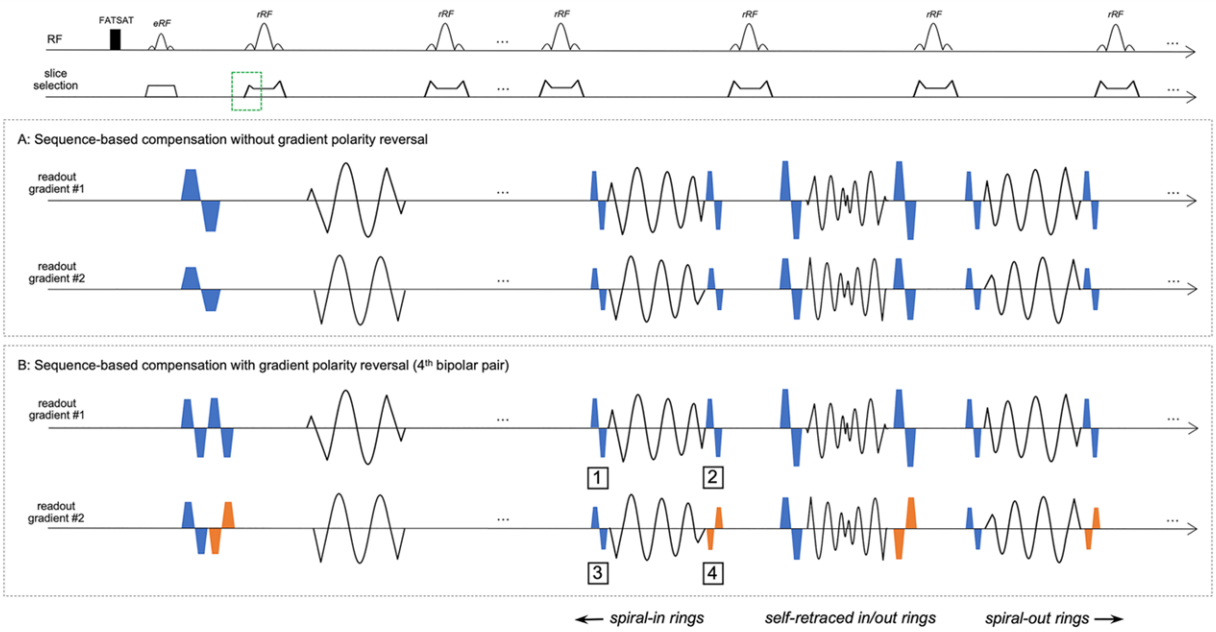

Figure 4-1. Pulse sequence timing diagrams including fat saturation, TSE data acquisition using annular spiral rings, a reshaped gradient waveform for slice-selection (green dashed box), and additional bipolar gradients (blue boxes) placed at each readout gradient axis #1 and # 2 for concomitant field compensation along the echo train. For each shot, the data were collected by spiral-in rings, a self-retraced spiral in-out ring, and spiral-out rings, sequentially, with the number of spiral-in rings equivalent to that of spiral-out rings. Inner rings require larger bipolar gradients than outer rings for maintaining the constant concomitant self-squared terms at the end of each echo spacing. A: Sequence-based compensation without bipolar-gradient polarity reversal. B: Sequence-based compensation with bipolar-gradient polarity reversal. Compared to A, the gradient polarity of one bipolar gradient pair in each echo spacing, the 4th pair for example (orange boxes), is set to be the opposite of the other pairs for self-balancing the concomitant quadratic cross-terms induced by these four added bipolar gradients. The first two bipolar pairs placed between the excitation RF pulse and the first refocusing RF pulse shown in A are split into four pairs, followed by the gradient polarity reversal of the 4th pair. A total of 5 ms additional time is added for an increased echo spacing to both sequences shown in A and B.

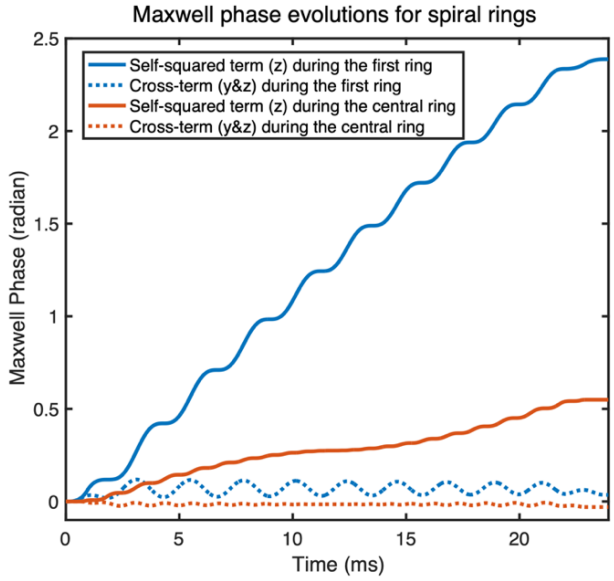

Figure 4-2. Simulation of phase evolutions induced by Maxwell fields for one specific pixel from a sagittal plane, of which the parameters include B_0 = 0.55 T, $Gmax$ = 21 mT/m, ETL = 9, spiral ring duration = 18 ms, pixel location (y, z) = (50, 50) mm. The self-squared term produced by the first spiral-ring with the largest gradient amplitude is almost five times larger than that by the central ring (blue solid line vs. orange solid line). The self-squared term from either the outer ring or inner ring is substantially larger than its corresponding quadratic cross-term (blue solid line vs. blue dashed line, orange solid line vs. orange dashed line, respectively).

and a scaled concomitant field time parameter $t_c(t)$ was given by

$$t_c(t) = \frac{1}{g_m^2}\int_0^t g_0^2(t')\,dt', \tag{4-4}$$

where g_0 is the gradient envelope and g_m is the maximal readout gradient amplitude used in all spiral rings. X, Y, Z are the logical coordinates which define the readout 1, readout 2, and slice coordinates, respectively. F_i are constants calculated from the rotation matrix, which are given in the appendix in Ref 3. In TSE imaging, however, each refocusing RF pulse alternates the sign of the accumulated Maxwell phase, resulting in a negative phase from the self-squared terms at the beginning and a positive phase at the end of each echo spacing (ESP). Hence, we modified the time parameter $t_{c_j}(t)$ specifically for SPRING-RIO TSE, as:

$$t_{c_j}(t) = \frac{1}{g_m^2}\left(\int_0^t g_j^2(t')\,dt' - \frac{M_j}{2}\right), \tag{4-5}$$

where g_j is the gradient envelope and M_j is the concomitant field integral of the j^{th} ring trajectory. The derivation of Equation 4-5 can be found in Appendix A.

Previously, a semiautomatic deblurring method with a maximized energy objective[23] was applied to SPRING-RIO TSE for B_0 field inhomogeneity correction. The term "semiautomatic" refers to the method where an automatic method is used to search for a high-resolution field map using offset frequency constraints calculated from an acquired low-resolution map. In this work, we chose the fast conjugate phase reconstruction method based on a Chebyshev approximation proposed by Chen et al. [24] and extended it to correct for nonlinear off-resonance effects induced by both B_0 field inhomogeneities and concomitant gradients in SPRING-RIO TSE. To perform simultaneous semiautomatic B_0 off-resonance correction and concomitant gradient compensation, a series of images are reconstructed from the following equation:

$$m(\boldsymbol{r};\Delta\omega_i) = \sum_{k=0}^{N-1} h_k\,(\Delta\widetilde{\omega}(\boldsymbol{r}) + \Delta\omega_i, \Delta\omega_c(\boldsymbol{r}), \tau) I_k(\boldsymbol{r}) - \frac{1}{2} h_0 I_0(\boldsymbol{r}),\ \ i = 1, 2 \ldots, \quad (4\text{-}6)$$

where $\Delta\widetilde{\omega}(\boldsymbol{r})$ is the B_0 off-resonance frequency constraint calculated from a low-resolution field map, and $\Delta\omega_i$ is constant frequency shift from $\Delta\widetilde{\omega}(\boldsymbol{r})$. h_k is the constant Chebyshev coefficient as a function of the local B_0 inhomogeneity, the concomitant field, and the readout length τ, the calculation of which is given in the appendix in Ref 24. $I_k(\boldsymbol{r})$ is the k^{th} order Chebyshev demodulated base image, and for $t \in [-\frac{\tau}{2}, \frac{\tau}{2}]$, it can be calculated as follows:

$$I_k(\boldsymbol{r}) = \int (\frac{2t}{\tau})^k W(t) s(t) e^{i2\pi k(t)\boldsymbol{r}} dt, \quad (4\text{-}7)$$

where $W(t)$ is the density compensation function. The concomitant field effect is first corrected when reconstructing the demodulated image $m(\boldsymbol{r};\boldsymbol{\Delta\omega_i})$, followed by a semiautomatic deblurring method for B_0 field inhomogeneity correction, using a maximized energy objective function:

$$\max_{\Delta\omega_i} \int p(\boldsymbol{r} - \boldsymbol{r}')\, m(\boldsymbol{r}';\Delta\omega_i)\, m(\boldsymbol{r}';\Delta\omega_i)^* d\boldsymbol{r}', \quad (4\text{-}8)$$

where $m(\boldsymbol{r};\Delta\omega_i)^*$ is the complex conjugate of $m(\boldsymbol{r};\Delta\omega_i)$**,** and $p(\boldsymbol{r})$ is the convolution kernel chosen to be a circularly symmetric Gaussian window. The optimization of $\Delta\omega_i$ that best deblurs a local region of $m(\boldsymbol{r};\Delta\omega_i)$ is performed by searching for a correct demodulated frequency which maximizes its local integral of signal energy. A high-resolution field map will then be generated after Equation 4-8, each pixel of which has its own estimated constant frequency shift.

The total number of base images required depends on the range of B_0 inhomogeneity and concomitant gradient field. Linear B_0 off-resonance correction based on an estimated spatially linear field map was incorporated to reduce the computational cost by narrowing the range of B_0 field inhomogeneity. For a given scan plane orientation with FOV and table shifts, linear

concomitant gradient correction was also applied to reduce the frequency range of an off-center slice to that of a slice at isocenter.[24]

4.3 Simulations

All simulations were implemented in MATLAB (R2020b software; MathWorks, Natick, MA). To illustrate the Maxwell field effects from self-squared terms of the SPRING-RIO TSE sequence, signal pathways along the echo train at several off-center table (z) locations and in the presence of B_1 inhomogeneity (resulting in different refocusing RF flip angles) were simulated by extended phase graph[25] (EPG) method with no k-space weighting. Signal intensity loss (SI_l) at each echo was calculated based on the equation:

$$SI_l = \frac{SI_c - SI_r}{SI_r}, \tag{4-9}$$

where SI_c and SI_r are the normalized signal curves of the current scenario and the standard T_2-decay curve as the reference, respectively. Specifically, axial planes with off-center table locations ranging from 0 to 60 mm with 20 mm increments, and with the refocusing RF flip angles ranging from 120° to 180° with 20° increments, were used for simulation. Other simulation parameters include B_0 = 0.55 T, echo train length (ETL) = 9, spiral readout = 16 ms, T_1 = 800 ms, and T_2 = 70 ms.

Ignoring B_0 inhomogeneity, the simulation of phase evolutions from self-squared terms during the acquisition window and along the echo train was performed for SPRING-RIO TSE with and without sequence-based corrections, from $z_c = 50$ mm off-center axial plane at 0.55 T. First, the net Maxwell-field-induced phase $\Delta\phi_{c_j}$ at the j^{th} ring trajectory with a gradient envelope g_j during the readout was calculated based on:

$$\Delta\phi_{c_j}(t) = \frac{\gamma z_c^2}{2B_0}\int_0^t g_j^2(t')dt'. \quad (4\text{-}10)$$

Second, considering the 180° refocusing RF pulse which alternates the sign of the Maxwell field induced phase, the accrued phase ϕ_{c_j} for j^{th} ring trajectory is given by:

$$\phi_{c_j}(t) = \sum_{k=0}^{j-1}(-1)^{k+j}\Delta\phi_{c_k}(\tau) + \Delta\phi_{c_j}(t), \quad (4\text{-}11)$$

where $\Delta\phi_{c_0}(\tau)$ is the net phase accrual between the excitation and first refocusing pulses. Finally, the increased phase accruals induced by the added bipolar gradients were also calculated and added into ϕ_{c_j} for each echo spacing in SPRING-RIO TSE with sequence-based modifications. Further, to illuminate the quadratic cross-terms and the effect of bipolar-gradient polarity reversal on the SPRING-RIO TSE sequence, Maxwell phase evolutions during two individual (second and central) echo spacings were simulated at a specific sagittal location with and without bipolar-gradient polarity reversal.

4.4 MRI experiments

4.4.1 Data acquisition

Experiments were performed on 1.5 T (MAGNETOM Avanto) and prototype 0.55 T with high-performance gradients (ramped-down MAGNETOM Aera) MR scanners (Siemens Healthcare, Erlangen, Germany) using a 12-channel (1.5 T) or 16-channel (0.55 T) receive head coil.

In phantom studies, sagittal data from a resolution phantom was acquired at 0.55 T using SPRING-RIO TSE with no compensation, with sequence-based compensation (Figure 4-1A), and with sequence-based compensation including bipolar-gradient reversal (Figure 4-1B). At 1.5 T, images from an axial plane at isocenter were acquired using SPRING-RIO TSE with no

compensation and Cartesian TSE as a reference, while images at -10.6 cm off-center location were acquired via SPRING-RIO TSE with no compensation and with sequence-based compensation as shown in Figure 4-1B. Relevant spiral imaging parameters included FOV = $180 \times 180\ mm^2$, spatial resolution $= 0.65 \times 0.65\ mm^2$, slice thickness = 4 mm, refocusing RF flip angle = 180°, ETL = 8 (0.55 T) or 9 (1.5 T), ADC = 21 ms (0.55 T) or 12 ms (1.5 T).

Eleven healthy volunteers (six at 0.55 T and five at 1.5 T) gave informed consent and were scanned using SPRING-RIO TSE sequences with and without sequence-based compensation, and a standard Cartesian TSE sequence to evaluate the overall image quality. Table 4-1 lists parameters of pulse sequences used for human studies at 0.55 T and 1.5 T. Data were acquired consecutively at matched imaging planes using 14 slices with 4-mm slice thickness and 2-mm gap. A saturation pulse was used for fat suppression, and for reconstruction corrected spiral-ring trajectories were utilized based on a one-time model-based trajectory calibration.[13,26] Axial, coronal, and sagittal slices of the brain were all scanned, with an increased FOV ($250 \times 250\ mm^2$) for non-axial orientations. For signal averaging (NSA), the data of each slice from SPRING-RIO TSE was acquired once at 1.5 T (1-NSA, 0:33 min) and six times at 0.55 T (6-NSA, 2:24 min).

	Sequences	FOV (mm²)	TR (ms)	TEeff (ms)	Readout (ms)	Refocusing RF	ESP (ms)	ETL	# Shots	# NSA	Scan time (min)	Spatial Res (mm³)
0.55 T	SPRING-RIO TSE	230×230	3000	127	21	180°	31.7	8	8	6	2:24	0.70×0.70×4
	Cartesian TSE	230×230	3000	126	8	180°	12.6	16	20	3	3:08	0.72×0.72×4
1.5 T	SPRING-RIO TSE	230×230	3000	114	12	180°	22.8	9	11	1	0:33	0.71×0.71×4
	Cartesian TSE	230×230	3000	117	5	180°	10.7	16	20	1	1:08	0.72×0.72×4

Table 4-1. Sequence parameters for SPRING-RIO TSE and Cartesian TSE at 0.55 T and 1.5 T, respectively.

4.4.2 Image reconstruction

All images were reconstructed offline in MATLAB. 2D NUFFT[27] code was used for non-Cartesian image reconstruction. ESPIRiT[28] was used for coil sensitivity map estimation. A low-resolution

B_0 field map was generated from single-shot spirals at two TEs (ΔTE = 1 ms) acquired during two preparation scans before TSE acquisitions.[29] To illustrate the performance of reconstruction-based compensation, both phantom and in vivo images using SPRING-RIO TSE with sequence-based compensation were reconstructed and compared with no compensation, with concomitant field correction only, and with simultaneous concomitant field and B_0 field inhomogeneity corrections.

A 3D table of Chebyshev coefficients h_k was precalculated with B_0 field inhomogeneity ($\frac{\Delta\omega_i}{2\pi}$) ranging from -150 Hz to 150 Hz (1.5 T) or -80 Hz to 80 Hz (0.55 T), and concomitant field off-resonance frequency ($\frac{\Delta\omega_c}{2\pi}$) ranging from 0 Hz to 250 Hz (1.5 T) or 0 Hz to 400 Hz (0.55 T), both with a 1 Hz frequency increment and 15 base images. As discussed in Ref 24, the range of frequency was sufficient after incorporating linear concomitant field and B_0 field inhomogeneity corrections, and this 3D table was used for data sets acquired with similar sequence parameters. The searching range of the B_0 field offset frequency shifts from -60 Hz to 60 Hz with a 10 Hz frequency increment was used for the semiautomatic deblurring.

4.4.3 Image quality analysis

Evaluation of SPRING-RIO TSE with full compensation and conventional Cartesian TSE was performed quantitatively on in vivo data. SNR with the pseudo-replica method[30] was calculated, and the SNR efficiency map was then derived by multiplying the calculated SNR by the coefficient $1/(voxel\ size\ \times \sqrt{scan\ time})$, which equaled 1.17 at 0.55 T and 2.38 at 1.5 T for SPRING-RIO TSE, and 1.0 at 0.55 T and 1.66 at 1.5 T for Cartesian TSE. Regions of interest (ROIs) were drawn in white matter (WM) and gray matter (GM) on the SNR efficiency maps, and the averaged SNR was obtained for each subject at both 0.55 T and 1.5 T, with three slices per orientation and a total

of nine slices per subject. Pairwise comparisons between these two imaging methods were performed using one-way ANOVA with the Tukey-Kramer post hoc test.

4.5 Results

4.5.1 Simulations

Simulation results in Figure 4-3A and 4-3B illustrate how echo-to-echo phase variations caused by Maxwell fields along the echo train affect the signal pathway of SPRING-RIO TSE without sequence-based compensation. The evolution of signal intensity loss, each with nine echoes, simulated at four different table (z) positions are shown in Figure 4-3A. A 150° refocusing RF flip angle was used for the simulation to approximate a slice-selective refocusing RF pulse with a nominal flip angle of 180°. As table position increases, the signal intensity changes along the echo-train in a non-intuitive fashion. For example, signal intensities simulated at 60 mm off-center drop rapidly for the first several echoes, while the magnitude of the 5^{th} echo (at TE_{eff}) is higher than that of its surrounding echoes, due to the signal distribution among spin echo (SE) and stimulated echo (STE) components. Figure 4-3B shows the dependence of refocusing flip angles on the magnitude of echoes simulated at 40 mm off-center table location. The signal intensity loss curve shows more oscillations as the refocusing flip angle decreases. Note that for a given pixel, echoes from the signal evolution using an ideal 180° refocusing RF pulse (no STE, green line) will have a phase modulation (not shown) which may result in ghosting and shading artifacts, although the magnitudes are the same as those from the standard T_2-decay curve, which results in no signal intensity loss.

Figure 4-4 shows the simulation of Maxwell phase pathways from self-squared terms along the echo train and during the acquisition window for SPRING-RIO TSE without (black lines) and

with (blue lines) sequence modifications, for an axial plane 50 mm off-center. Red dots indicate the k-space center, while orange arrows show the effects of refocusing RF pulses, which alternate the sign of the phase error throughout the echo train. The green dashed boxes indicate examples of increased Maxwell phase by added bipolar gradients. It can be clearly seen that outer rings produce more Maxwell phase accruals than inner rings and thus require less additional Maxwell phase from the added bipolar pairs. After adding the bipolar compensation gradients, the accrued phase for each echo spacing starts at $-\phi$ and ends at ϕ, where ϕ is a constant value, and the phase at the k-space center, as well as at the other spin echoes, is zero.

Figure 4-5 shows the simulation of Maxwell phase evolutions from quadratic cross-terms during the second and central echo spacings for SPRING-RIO TSE without (dashed lines) and with (solid lines) bipolar-gradient polarity reversal, at a pixel location (50, 50) mm in the sagittal plane. The quadratic cross-terms from spiral rings have minimal effects on phase variations over echo spacings due to the gradient waveforms with alternating polarities; however, the pair of added bipolar gradients will not only produce the self-squared phase terms as needed but will also create undesirable cross-terms that may be large enough to induce additional phase error variations among echoes (dashed lines). With bipolar-gradient polarity reversal, the net phase accruals from the bipolars returns to zero at the end of each echo spacing (solid lines).

4.5.2 Phantom studies

Figure 4-6 shows how sequence modification with bipolar-gradient polarity reversal improves image quality at 0.55 T for a sagittal plane at isocenter. Figure 4-6A is an image from Cartesian TSE as the reference, while Figure 4-6B is reconstructed from SPRING-RIO TSE with no compensation, showing severe bands of signal loss and obvious image artifacts. Figure 4-6C is the result with sequence-based compensation, but without gradient polarity reversal, showing

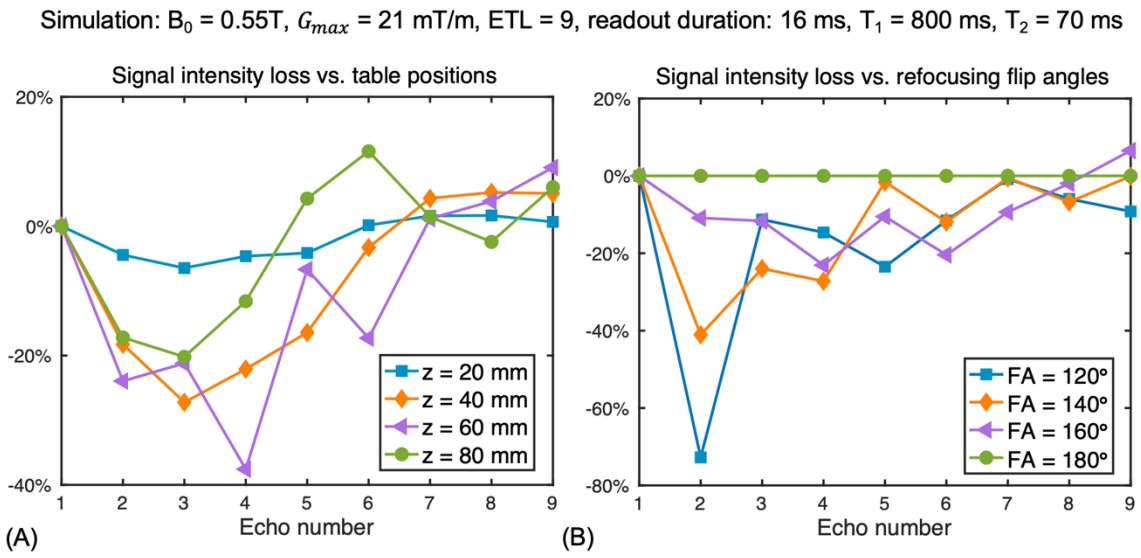

Figure 4-3. A-B: Simulation results showing how Maxwell fields affect the signal pathway of SPRING-RIO TSE sequence along the echo train, at several off-center axial table locations (A) and with different refocusing RF flip angles (B). Note that each signal evolution was simulated without k-space weighting. A 150° refocusing RF flip angle was used for the simulation of A and a 40 mm off-center axial plane for B.

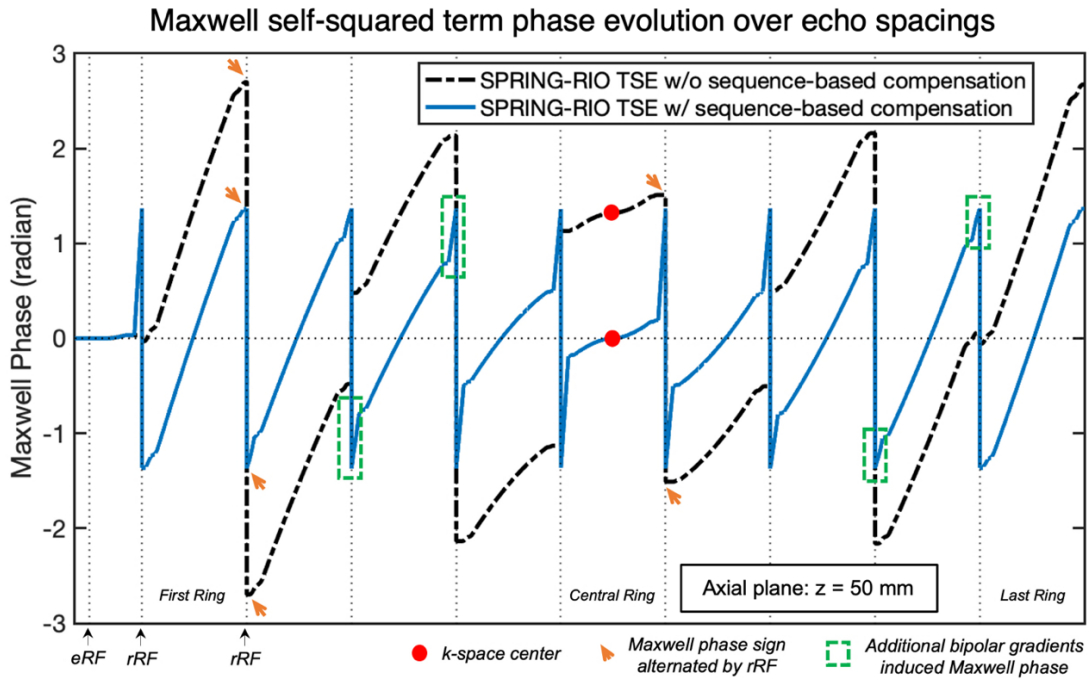

Figure 4-4. Results showing the Maxwell phase accruals from a $z_c = 50$ mm off-center axial plane along the echo train and during the readout, before (black lines) and after (blue lines) sequence-based compensation. *eRF* and *rRF* denote excitation and refocusing RF pulses, respectively. Red circles point out the k-space center, while orange arrows show the effects of *rRF*, which alternate the sign of the phase error throughout the echo train. Green dashed boxes indicate examples of increased Maxwell phase by added bipolar gradients. After compensation, the center of k-space has zero phase shifts and the phase at the end of each echo spacing has the designed value ($\emptyset \propto \frac{M_{max}}{2}$).

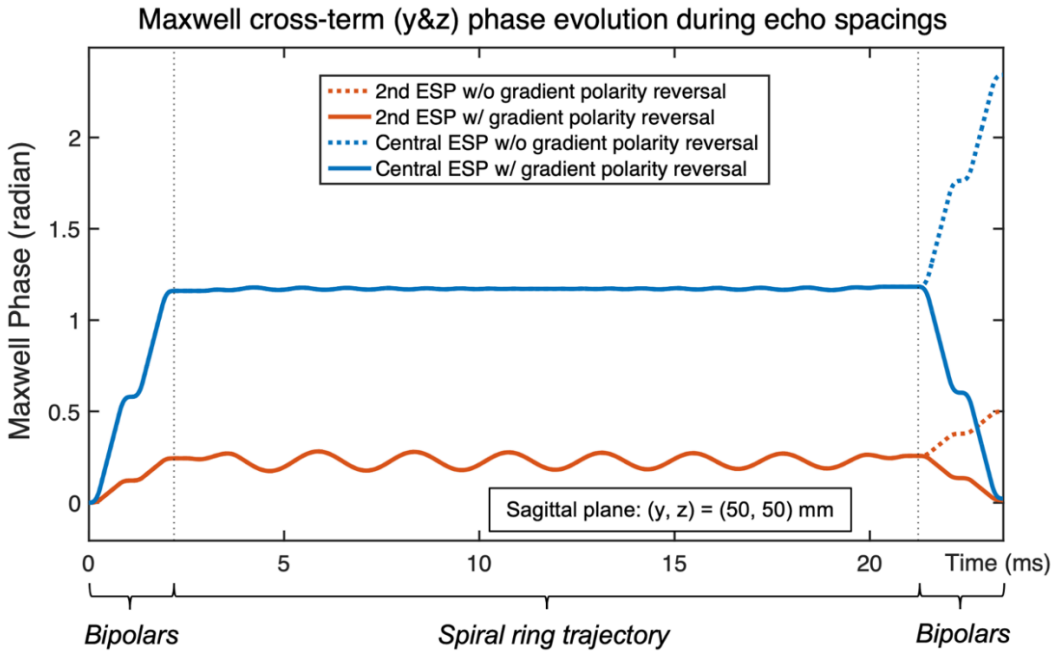

Figure 4-5. Simulation of cross-term Maxwell phase evolutions at a pixel location (y, z) = (50, 50) mm from a sagittal plane. The net cross-term phases evolve back to almost zero at the end of each echo spacing where the sequence modification with gradient polarity reversal is applied (solid line), while there is a huge phase difference between these two echo spacings when without gradient polarity reversal is not applied (dashed line).

improved image quality compared to Figure 4-6B but still presenting noticeable artifacts and signal loss along the diagonals (red arrows), primarily because of cross-term phase errors induced by the added bipolar gradients. Figure 4-6D is the result with sequence-based compensation along with gradient polarity reversal, indicating much better image quality with reduced artifacts and signal loss when compared to Figure 4-6B-C (see zoomed portions of images indicated by boxes). By applying the image reconstruction-based corrections for residual phase errors during the readout, artifacts are further reduced, as shown in Figure 4-6E. Some vials may show different image contrast between SPRING-RIO TSE and the reference, mainly due to the different sequence parameters (e.g., ESP and ETL) used in acquisition, though TE and TR are fixed. The images (Fig. 4-6B-E) show slight geometric distortion induced by gradient nonlinearity, which could be corrected using standard remapping methods.[31,32] Pre-scan normalization could also be utilized to remove the shading in Figure 4-6B-E.

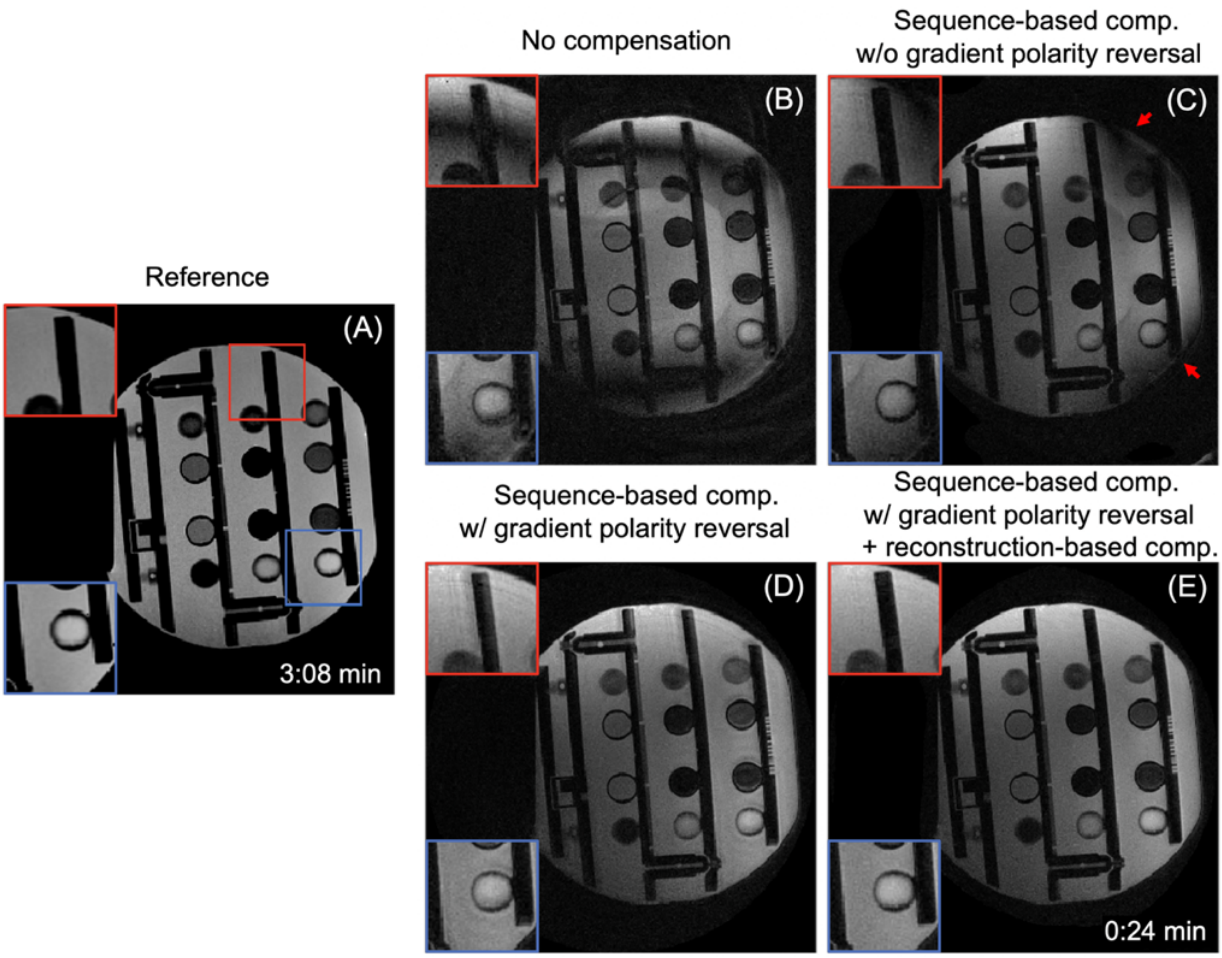

Figure 4-6. Reconstructed images of a sagittal slice in a resolution phantom demonstrating the performance of the sequence modification with gradient polarity reversal on image quality at 0.55 T. A: Image from Cartesian TSE as the reference (scan time: 3:08 min). B-E: Images from SPRING-RIO TSE with different compensation methods (scan time: 0:24 min). B: Image with no compensation showing severe signal loss and artifacts. C: Image with sequence-based compensation but without gradient polarity reversal, showing improved image quality when compared to B but still displaying obvious artifacts especially along the diagonals (red arrows). D: Image with sequence-based compensation and with gradient polarity reversal, showing much improved image quality with reduced artifacts and signal loss. E: By also applying image reconstruction corrections for residual phase errors along the readout, the artifacts are further reduced (zoomed regions). Geometric distortion shown in images (B-E) due to gradient nonlinearity could be corrected using standard remapping methods.

Figure 4-7 shows 1.5-T axial images acquired at two table (z) positions using SPRING-RIO TSE with different compensation methods and standard Cartesian TSE. At isocenter (z = 0), no obvious image artifacts are seen in Figure 4-7A from SPRING-RIO TSE with no compensation, compared to the reference in Figure 4-7B. For z = -10 cm, however, the result in Figure 4-7C from SPRING-RIO TSE with no compensation shows severe signal dropouts and blurring. Applying

the sequence-based compensation, Figure 4-7D shows a substantial reduction in image degradation associated with concomitant field effects along the echo train, but residual artifacts still exist. The image quality is further improved by applying reconstruction corrections for residual phase errors along the readout induced by concomitant field (named “Full Maxwell compensation” in Fig. 4-7E) and by both concomitant field and B_0 off-resonance correction (named “Full Maxwell plus B_0 off-resonance compensation” in Fig. 4-7F).

Figure 4-8 shows a representative example of double-oblique phantom images at 0.55 T. Improved image quality, in terms of signal loss, blurring, and artifacts, can be seen in the fully corrected image (Fig. 4-8C) when compared to no compensation (Fig. 4-8A) or partially corrected (Fig. 4-8B) images (zoomed regions). Minor residual artifacts remain in Figure 4-8C after corrections compared to the reference (Fig. 4-8D), which can also be seen in Figure 3 (Fig. 4-6A vs. Fig. 4-6E), potentially due to quadradic cross-terms or higher order terms from spiral rings during the readout which may need to be further corrected.

4.5.3 In vivo studies

Figure 4-9 shows images of one 1.5-T axial brain slice from a human subject acquired at -10.6 cm off-center. Figure 4-9A shows the Cartesian TSE image, while Figure 4-9B-E shows images acquired with the SPRING-RIO TSE sequence with no compensation (Fig. 4-9B), with sequence-based compensation along the echo train (Fig. 4-9C) and reconstructed using full Maxwell field compensation (Fig. 4-9D) and full Maxwell field plus B_0 off-resonance compensation (Fig. 4-9E). Comparing images before and after sequence-based compensation (Fig. 4-9B vs. 4-9C), improved image quality is consistent with simulation results and phantom studies, showing that strong artifacts and signal dropouts caused by concomitant fields along the echo train can be substantially reduced by sequence modifications of Figure 4-1B. Further improvements can be achieved after

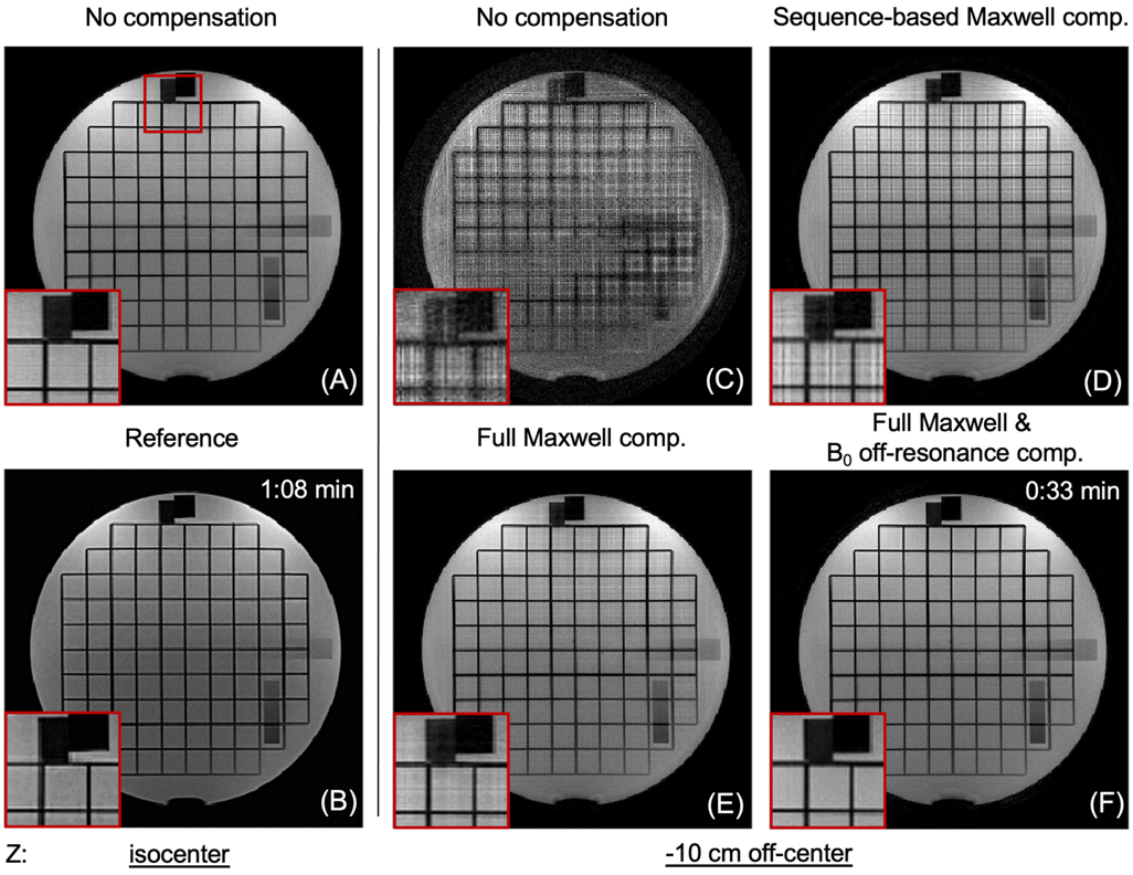

Figure 4-7. Phantom results from an axial plane scanned at 1.5 T showing the performance of concomitant compensation via different sequence modifications and image reconstruction. A, C-F: Images from SPRING-RIO TSE scanned at two locations and with different compensation methods (scan time: 0:33 min). B: Image from Cartesian TSE as the reference (scan time: 1:08 min). For the table location set at iso-center, there is no noticeable artifact shown in image (A) from uncompensated SPRING-RIO TSE compared to the reference (B). For the table location set at -10 cm off-center, the uncompensated image (C) from SPRING-RIO TSE shows substantial signal loss and artifacts. With sequence-based compensation along the echo train (D), no significant signal loss is seen but residual artifacts still exist (zoomed regions). Performing full Maxwell compensation completely removes Maxwell-field-induced image degradation (E). Applying B_0 inhomogeneity phase correction further improves image quality (F).

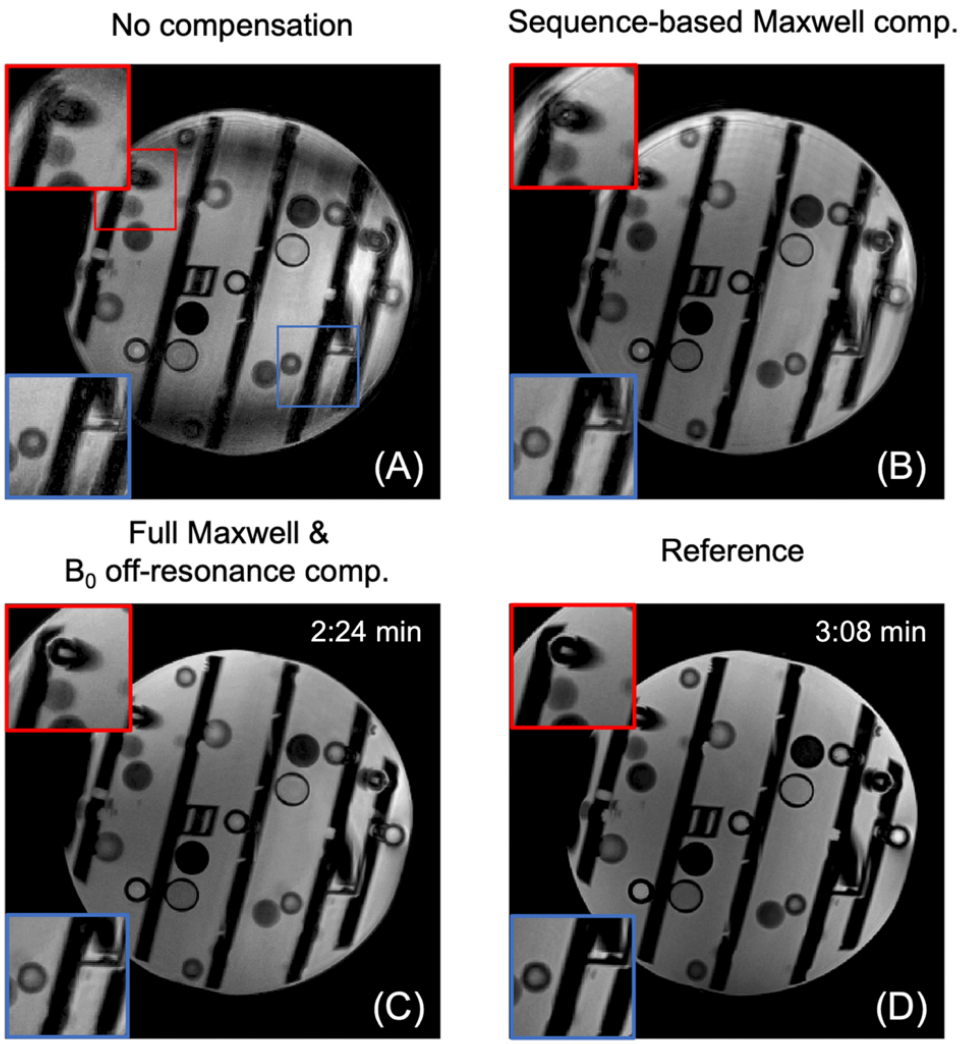

Figure 4-8. Images of a double-oblique slice (sagittal 30° towards coronal, 20° towards transverse) through a resolution phantom acquired with Gmax = 21 mT/m at 0.55 T. A-C: Image from SPRING-RIO TSE with different compensation methods (scan time: 2:24 min). D: Cartesian TSE as the reference (scan time: 3:08 min). Improved image quality, in terms of signal loss, blurring, and artifacts, can be seen in the fully corrected image (C) when compared to uncorrected (A) or partially corrected (B) images (zoomed regions).

fully correcting for both concomitant and B_0 inhomogeneity fields, as seen in Figure 4-9E compared to Figure 4-9C-D in the zoomed portions of images indicated by the boxes. After all corrections, SPRING-RIO TSE (0:33 min for 14 slices) has similar image quality compared to the Cartesian reference (1:08 min for 14 slices) but requires less than half of the total scan time.

Figures 4-10 (1.5 T) and 4-11 (0.55 T) display examples of axial, coronal, and sagittal brain

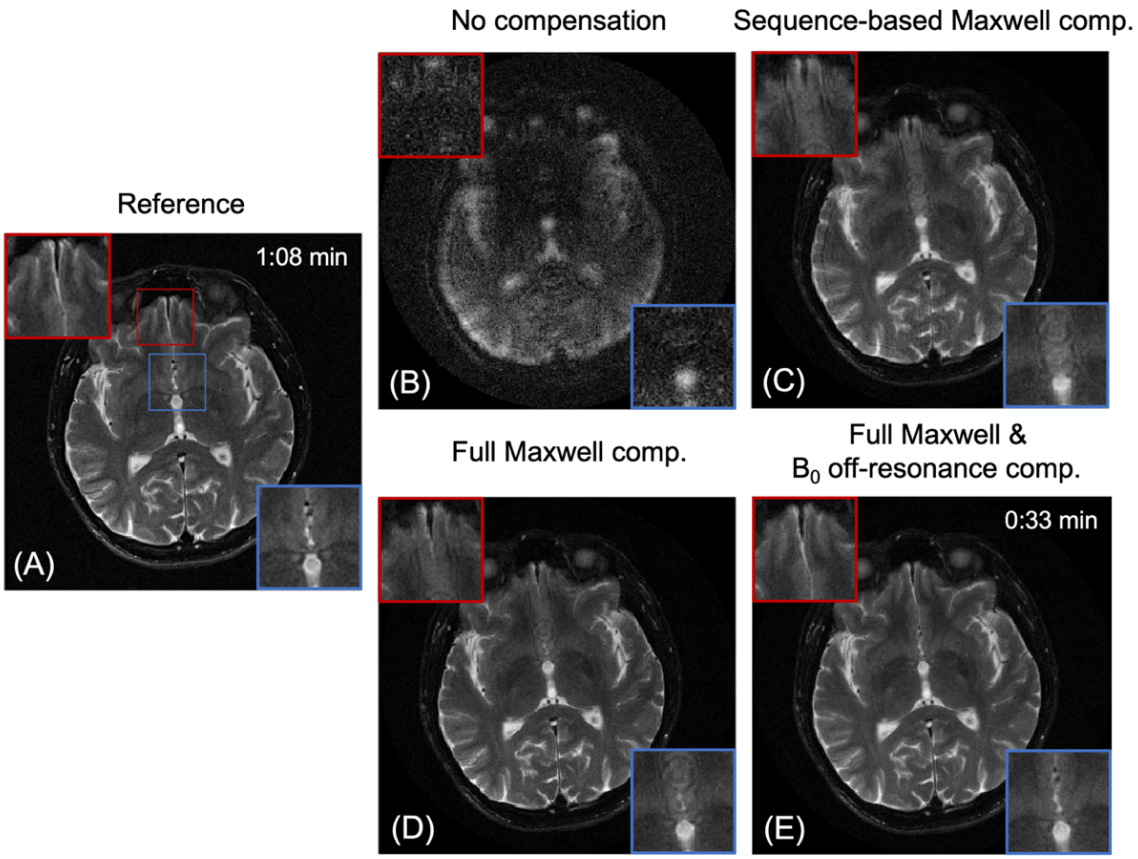

Figure 4-9. Comparison of 1.5-T axial brain images acquired at z = -10.6 cm plane via Cartesian TSE as the reference (A) and SPRING-RIO TSE (B-E). Images are reconstructed with no compensation (B), with sequence-based compensation (C), with full Maxwell field compensation (D) which includes sequence-based compensation along the echo train and reconstruction-based compensation along the trajectory, and with full Maxwell field compensation plus B_0 off-resonance correction (E). After full corrections, the image E from SPRING-RIO TSE with minimal artifacts presents similar image quality compared to the reference A (zoomed regions) but with less than half the total scan time.

images from SPRING-RIO TSE with no compensation (top row) or with full Maxwell plus B_0 off-resonance compensation (middle row), and from standard Cartesian TSE (bottom row). No obvious artifacts are observed in SPRING-RIO TSE images after full compensation. SNR measurements in WM and GM with SPRING-RIO TSE versus the standard Cartesian TSE are shown in Figure 4-12. Significant increases (15 – 20%) of the SNR efficiency ($p < 0.05$) are shown in both white and gray matter for SPRING-RIO TSE compared to those for standard Cartesian TSE at both 0.55 T and 1.5 T. Examples of the SNR efficiency maps can be found in Figure 4-13.

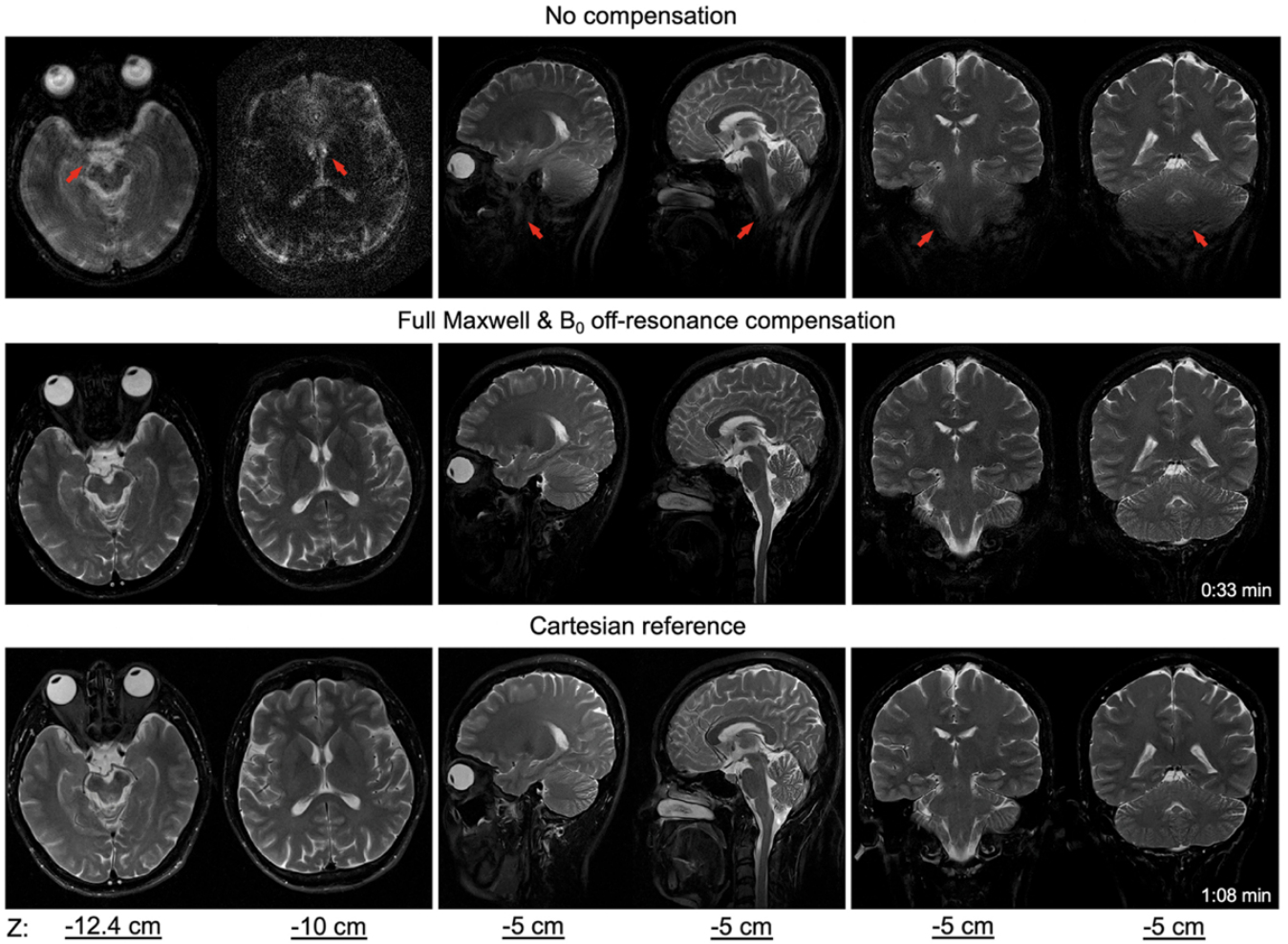

Figure 4-10. In vivo images acquired at 1.5 T using SPRING-RIO TSE with no compensation (top row), and with full Maxwell field compensation plus B_0 off-resonance compensation (middle row), compared to those from Cartesian TSE (bottom row). The slice positions for axial images (left column) are -12.4 cm and -10 cm, while the table position for sagittal (middle column) and coronal images (right column) is set to -5 cm. The red arrows point to structures where SPRING-RIO TSE with no compensation shows strong signal loss, image blurring or artifacts, due to strong time-varying and spatially dependent concomitant gradients.

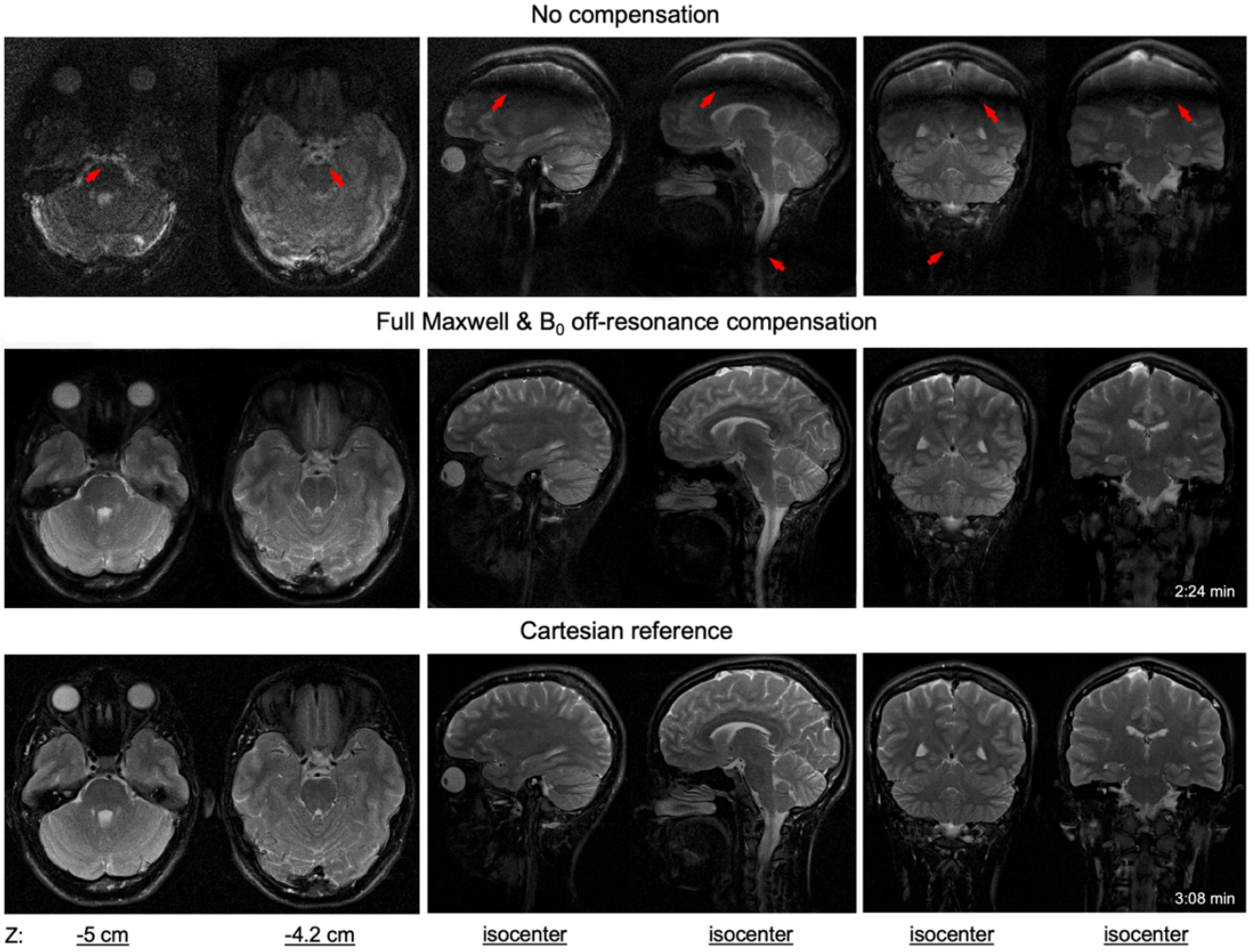

Figure 4-11. In-vivo images acquired at 0.55 T using SPRING-RIO TSE, with no compensation (top row), and with full Maxwell field compensation plus B_0 off-resonance compensation (middle row), compared to those from Cartesian TSE (bottom row). The slice positions for axial images (left column) are -5 cm and -4.2 cm, while the table position for sagittal (middle column) and coronal images (right column) is set to be isocenter. The red arrows point to structures where there are severe bands of signal loss, image blurring or artifacts.

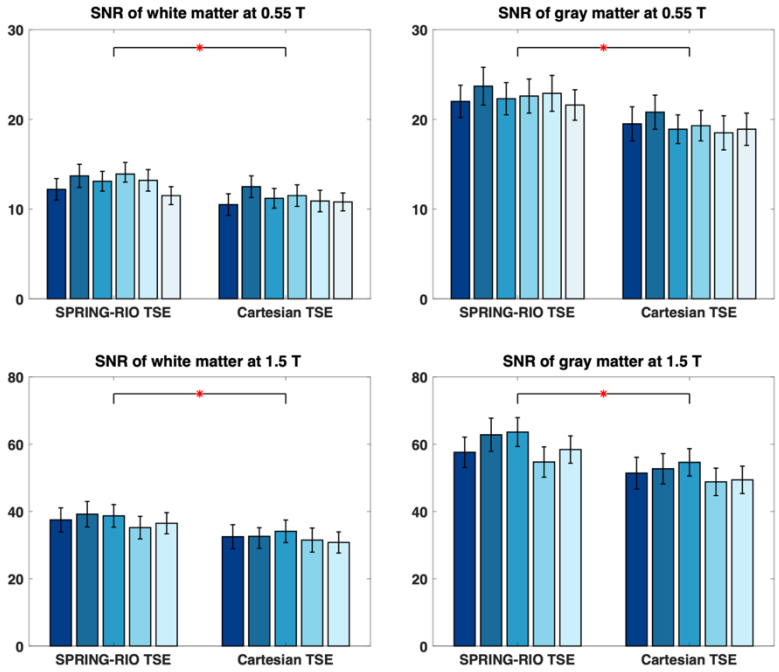

Figure 4-12. SNR efficiency values of ROIs in white matter (left) and gray matter (right) using SPRING-RIO TSE and standard Cartesian TSE. The different bars for each scenario represent the average values computed for six volunteers at 0.55 T (top) and five volunteers at 1.5 T (bottom). For each volunteer, nine slices are selected for SNR measurements. The asterisks indicate statistically significant increases of the SNR efficiency using SPRING-RIO TSE over that using Cartesian TSE, in both white matter and gray matter and at both 0.55 T and 1.5 T ($p < 0.05$).

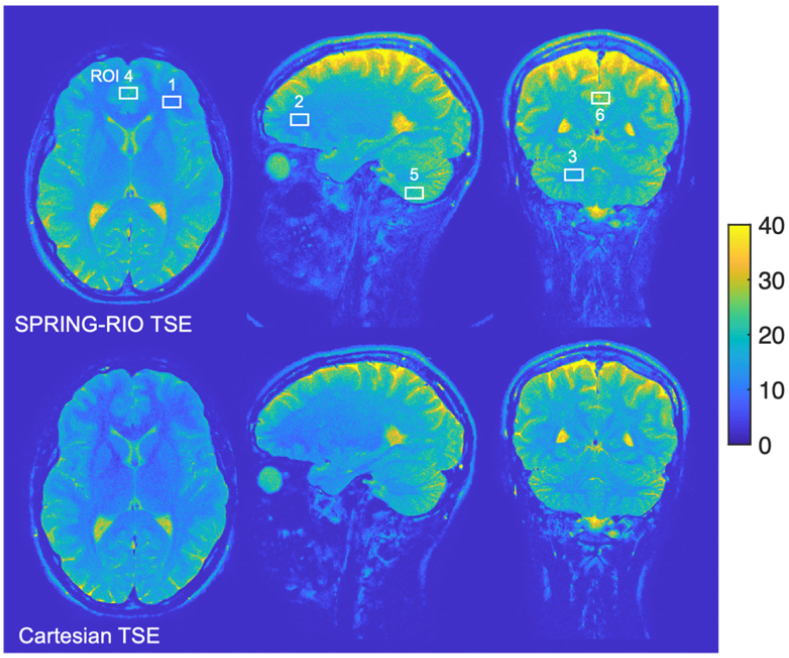

Figure 4-13. Example of comparisons of the SNR efficiency maps of SPRING-RIO TSE and the Cartesian reference at 0.55 T. The SNR values of ROIs (1 - 3 for WM, 4 - 6 for GM) are shown below.

Averaged SNR	White matter			Gray matter		
ROIs	1	2	3	4	5	6
SPRING-RIO TSE	9.1	11.5	13.0	20.9	22.1	25.3
Cartesian TSE	7.6	9.7	10.9	17.5	18.9	20.6

4.6 Discussion

TSE imaging relies heavily on a stable signal pathway along the echo train, and any signal cancellation due to echo-to-echo phase variations from non-negligible, time-varying concomitant fields cannot be corrected by directly applying image-reconstruction-based compensation. Here we demonstrated a spiral annular ring TSE sequence with both sequence- and reconstruction-based correction of concomitant field artifacts at 0.55 T and 1.5 T. The first and most important step is to eliminate the difference in phase shifts among echoes via sequence modifications to maintain the CPMG condition in SPRING-RIO TSE. Using bipolar waveforms as the quadratic nulling gradients permits the self-squared concomitant field integrals to be further increased, as needed for echoes with small concomitant integrals generated from inner spiral ring waveforms, while still maintaining the original zeroth gradient moment. When imaging in non-axial orientations, additional considerations need to be taken for quadratic cross-terms from non-zero, time-overlapped gradient waveforms. In this work, several strategies were used to mitigate cross-term phase errors. First, the timing of gradient waveforms was adjusted so that there was minimal or no gradient overlapping between slice crushers and readout gradients. Second, unlike spiral-ring readouts, for which the induced cross-term phase can be neglected compared to the self-squared counterparts because of the time-alternation of gradient polarities (see Figure 4-2), the cross-terms from added bipolar pairs are much closer in amplitude to the self-squared terms, because the same gradient polarity is played during the time of overlap. The performance of artifact suppression using sequence-based compensation with bipolar-gradient polarity reversal for one of four bipolar gradients (Figure 4-1B) over that without bipolar-gradient polarity reversal (Figure 4-1A) was demonstrated by the phantom study shown in Figure 4-6. Although in this study we did not notice a strong influence of small, but non-zero, cross-term phase errors from spiral-ring waveforms, a

future study may be needed to evaluate the potential impact of these phase errors on image quality. On the other hand, the added bipolar gradients will create unwanted eddy currents and increase certain sensitivity to flow signals. However, the induced eddy currents will be partially self-cancelled with minimal effects on the phase variation over echo spacings because of short, multiple on and off correction gradient transitions. Using a flow-compensated 1-2-1 gradient scheme instead of 1-1 bipolars would show better flow artifacts suppression, although it might further increase the minimum ESP.

Imaging plane shift (or off-center distance) is one of the major sources in generating concomitant fields, and for slices that are far away from isocenter, concomitant gradient correction becomes increasingly important. Setting the table position at, or close to, isocenter before scanning is a straightforward way to mitigate concomitant field effects at 1.5 T by decreasing the z^2 component, which dominates the amplitude of the concomitant fields B_c. However, lower-field systems will suffer from image degradation associated with these gradients at positions closer to isocenter than higher-field systems, as the artifacts at 0.55 T can be easily seen in Figure 4-11 where the table position is set at 4 cm off-center for an axial plane, and even at isocenter for sagittal and coronal planes. Furthermore, the multi-slice technique used in 2D TSE-based acquisitions may produce undesirable and unexpected artifacts associated with the slice position at 0.55 T, which cannot be fixed by a simple table movement to isocenter. Therefore, the proposed compensation method is necessary to mitigate the concomitant gradient effects for a given scan orientation, especially when scanning at low fields.

The maximal amplitude of spiral ring gradients is another concern because the concomitant field phase is proportional to the square of the gradient amplitude. In this work, a moderate maximal gradient amplitude of 21 mT/m was used to constrain the spiral design[33]. Reducing the

maximal gradient amplitude to around 10 mT/m, for example, will decrease the concomitant field offset frequency by a factor of four and thus may alleviate the requirement for comprehensive concomitant field compensation. However, this may increase the total scan time by nearly half per measurement for a given parameter set (FOV, spatial resolution, ETL, etc.). For time-limited applications where imaging speed is an important metric, such as breath-held single-shot T_2-weighted abdominal[34] or lung imaging[35], decreasing the maximal gradient amplitude for certain reduction of concomitant field effects but with an increased scan time may be impractical; instead, a spiral readout with a higher maximal gradient amplitude (30 - 40 mT/m) and a higher slew rate (150 - 180 T/m/s) is preferable for fast scanning, and this will inevitably increase the concomitant field offset frequency by several times and must be corrected by the methods proposed in this study.

As observed from phantom and in vivo results, effective image reconstruction-based compensation is achieved to correct the residual phase errors induced by both the concomitant field and B_0 field inhomogeneity during the spiral-ring readout for each echo, although the retraced in-out design will partially self-correct the off-resonance effects. As discussed in Ref 24, semiautomatic B_0 off-resonance correction may offer some compensation for concomitant field effects, since the time parameter t in off-resonance phase term $\phi(\Delta\omega(\boldsymbol{r}), \Delta\omega_c(\boldsymbol{r}), t)$ is equivalent to approximating the scaled concomitant field time parameter t_c as at, where a is a constant. However, in this work we found that directly applying semiautomatic B_0 off-resonance correction to images acquired using SPRING-RIO TSE with sequence-based compensation may still exhibit obvious image artifacts and cannot completely eliminate the residual concomitant field phase error (see Figure 4-14). The rationale behind this is that the signal phase evolution during the readout caused by concomitant gradients may be very different from that caused by B_0 inhomogeneity

fields in SPRING-RIO TSE. For example, $t_c \approx t$ may only fit to outer spiral rings where the gradient amplitude achieves a constant and almost maximum value g_m, while t_c becomes much smaller than the value of t for inner rings with small gradient amplitudes. Thus, the approximation of the scaled time parameter t_c as a linear function of t for the same constant parameter a may be unreasonable for spiral rings designed in our sequences, and compensation of time-varying, spatially dependent concomitant fields is necessary before applying semiautomatic B_0 off-resonance correction. As a result, reconstruction-based compensation was implemented in this work for artifact-free images by simultaneously correcting concomitant gradient field and B_0 field inhomogeneity.

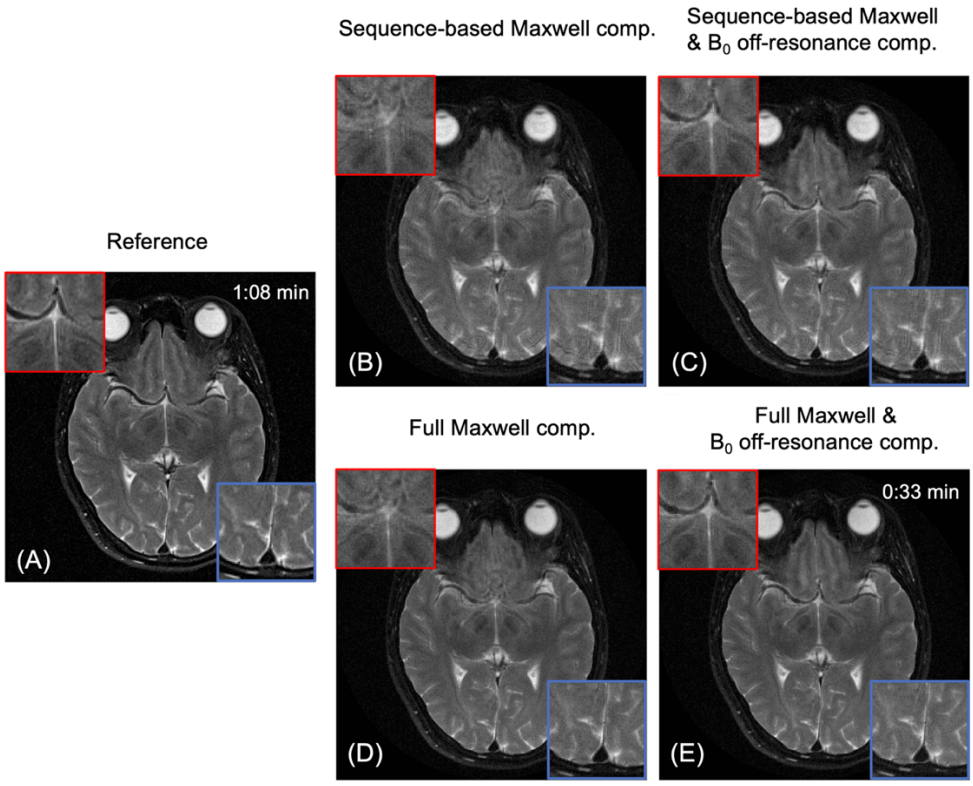

Figure 4-14. Reconstructed images of an axial brain slice from Cartesian TSE (A) and SPRING-RIO TSE (B-E) and at 1.5 T. B: Image acquired with sequence-based compensation but without any reconstruction compensation. C: Image acquired with sequence-based compensation and reconstructed with semiautomatic B0 off-resonance compensation only during the readout. D: Image acquired with sequence-based compensation and reconstructed with Maxwell field compensation only during the readout. E: Image acquired with sequence-based compensation and reconstructed with simultaneous Maxwell field and B_0 off-resonance compensation during the readout. Note that artifacts still exist in image C and D, due to the residual off-resonance effects.

Compared to imaging at 3 T, a lower magnetic field strength (e.g., 0.55 T, 1.5 T) offers favorable physical properties, such as increased B_0 field homogeneity and longer T_2^* decay, which permits SNR-efficient acquisitions such as spiral imaging with a longer readout. Because the effective SNR scales with the time spent on sampling but inversely with the total scan time ($\propto \sqrt{\frac{T_{sampling}}{T_{scan}}}$), a prolonged spiral-ring data acquisition strategy used in this work (e.g., 12 ms at 1.5 T, 21 ms at 0.55 T) can be leveraged to mitigate the SNR loss at lower fields compared to the standard Cartesian TSE for a fixed total scan time, as demonstrated in Figure 4-10. Furthermore, for SPRING-RIO TSE protocols shown in Table 4-1, the RF SAR from the 180° refocusing RF pulses is approximately 53% (e.g., at 0.55 T) of that from the corresponding Cartesian TSE, because of a higher k-space coverage per spin echo with a shorter echo train length (e.g., 8 versus 15) per shot. Increasing the spiral-ring readout duration and/or using a longer ETL is feasible to further improve scan efficiency, though it may induce stronger off-resonance effects and/or an increased RF SAR. However, the sequence-based compensation proposed in this work requires almost 5 ms of additional time added in each echo spacing; future studies are warranted to explore optimization of sequence parameters to reduce the sacrifice in SNR/scan efficiency.

4.7 Conclusion

In this chapter, we demonstrated a 2D spiral-ring T_2-weighted TSE pulse sequence that incorporates sequence modifications and image reconstruction methods to mitigate the image degradation associated with concomitant gradient effects at 0.55 T and 1.5 T. This approach presents a general compensation method that can be extended to compensate concomitant field induced effects for TSE imaging with other asymmetric non-Cartesian trajectories for low-field MRI and is applicable to all field strengths.

4.8 Appendix

The derivation of Equation 4-5 is described below:

1. After sequence-based corrections, the final concomitant integrals at the beginning and at the end of each echo spacing are constant values of $-M_{max}/2$ and $M_{max}/2$, respectively.
2. Due to the added bipolars, the increased Maxwell integral produced by the added bipolars for the current j^{th} echo spacing is equal to $(M_{max} - M_j)$, with the Maxwell integrals produced by the bipolars both before and after the readout equal to $(M_{max} - M_j)/2$.
3. The Maxwell integral at the beginning of the readout can be expressed as

$$-\frac{M_{max}}{2} + \frac{M_{max} - M_j}{2} = -\frac{M_j}{2}$$

4. The Maxwell integral $M_j(t)$ during the readout can then be expressed as

$$M_j(t) = -\frac{M_j}{2} + \int_0^t g_j^2(t')\,dt'$$

5. The final time parameter $t_{c_j}(t)$ can then be calculated by dividing $M_j(t)$ by g_m^2, which becomes:

$$t_{c_j}(t) = \frac{1}{g_m^2}\left(\int_0^t g_j^2(t')\,dt' - \frac{M_j}{2}\right)$$

4.9 References

1. Bernstein MA, Zhou XJ, Polzin JA, King KF, Ganin A, Pelc NJ, Glover GH. Concomitant gradient terms in phase contrast MR: analysis and correction. *Magn Reson Med*. 1998; 39:300–308.
2. Zhou XJ, Tan SG, Bernstein MA. Artifacts induced by concomitant magnetic field in fast spin echo imaging. *Magn Reson Med*. 1998;40:582–591.
3. King KF, Ganin A, Zhou XJ, Bernstein MA. Effect of Maxwell fields in spiral scans. Concomitant gradient field effects in spiral scans. *Magn Reson Med*. 1999;41:103–112.

4. Zhou XJ, Du YP, Bernstein MA, Reynolds HG, Maier JK, Polzin JA. Concomitant magnetic field induced artifacts in axial echo planar imaging. *Magn Reson Med*. 1998; 39:596–605.

5. Du YP, Joe Zhou X, Bernstein MA. Correction of concomitant magnetic field-induced image artifacts in nonaxial echo-planar imaging. *Magn Reson Med*. 2002;48(3):509–15.

6. Hennig J, Nauerth A, Friedburg H. RARE imaging: a fast imaging method for clinical MR. *Magn Reson Med*. 1986;3:823–833.

7. Mugler JP III. Optimized three-dimensional fast-spin-echo MRI. *J Magn Reson Imaging*. 2014;39:745-767.

8. Campbell-Washburn AE, Ramasawmy R, Restivo MC, et al. Opportunities in interventional and diagnostic imaging by using high-performance low-field-strength MRI. *Radiology*. 2019;293:384–393.

9. Hori M, Hagiwara A, Goto M, Wada A, Aoki S. Low-Field Magnetic Resonance Imaging: Its History and Renaissance. *Invest Radiol*. 2021;56(11):669-679.

10. Restivo MC, Ramasawmy R, Bandettini WP, Herzka DA, Campbell-Washburn AE. Efficient spiral in-out and EPI balanced steady-state free precession cine imaging using a high-performance 0.55T MRI. *Magn Reson Med*. 2020;84:2364–2375.

11. Javed A, Ramasawmy R, O'Brien K, et al. Self-gated 3D stack-of-spirals UTE pulmonary imaging at 0.55T. *Magn Reson Med*. 2022;87:1784–1798.

12. Wang Z, Feng X, Mugler JP, Salerno M, Campbell-Washburn AE, Meyer CH. Spiral-in-out bSSFP Real-Time Cine on a High Performance 0.55T Scanner. In Proceedings of the 29th Annual Meeting of ISMRM, Virtual Conference, 2021. p. 0504.

13. Wang Z, Allen SP, Feng X, Mugler JP, Meyer CH. SPRING-RIO TSE:2D T2-Weighted Turbo Spin-Echo brain imaging using SPiral RINGs with retraced in/out trajectories. *Magn Reson Med*. 2022;88:601-616.

14. Li Z, Wang D, Robison RK, et al. Sliding-slab three-dimensional TSE imaging with a spiral-in/out readout. *Magn Reson Med*. 2016;75:729-738.

15. Li Z, Karis JP, Pipe JG. A 2D spiral turbo-spin-echo technique. *Magn Reson Med*. 2018; 80:1989–1996.

16. Meiboom S, Gill D. Modified spin-echo method for measuring nuclear relaxation times. *Rev Sci Instrum*. 1958;29:688–691.

17. Li Z, Srivastava SP, Karis JP. A spiral fluid-attenuated inversion recovery magnetic resonance imaging technique for stereotactic radiosurgery treatment planning for trigeminal neuralgia. *Med Phys*. 2021;48:6881–6888.

18. Mugler JP, Campbell-Washburn AE, Ramasawmy R, Pfeuffer J, Meyer, CH. Maxwell Compensation for Spiral Turbo-Spin-Echo Imaging. In Proceedings of the 29th Annual Meeting of ISMRM, Virtual Conference, 2021.p.0003.

19. Block W, Pauly J, Nishimura D. RARE spiral T_2-weighted imaging. *Magn Reson Med*. 1997;37:582–590.

20. Hennig J, Menza M, Barghoorn A, Riemenschneider B, Kroboth S, Zaitsev M. Spiral RARE with annular segmentation. In Proceedings of the 27th Annual Meeting of ISMRM, Montreal, Quebec, Canada, 2019. p. 4632.

21. Wang Z, Feng X, Mugler JP, Meyer CH. Rapid and Simultaneous Acquisition of T2-weighted and Fluid-attenuated Brain Images using a Spiral-ring Turbo Spin-echo Imaging. Proceedings of the ISMRM 29th Annual Meeting, Virtual Conference, 2021. p. 1247.

22. Wang Z, Feng X, Ramasawmy R, Campbell-Washburn AE, Mugler JP, Meyer CH. Maxwell Field Compensation for 2D Spiral-Ring Turbo Spin-Echo Imaging at 0.55T and 1.5T. In Proceedings of the 31st Annual Meeting of ISMRM, London, UK, 2022.

23. Allen SP, Feng X, Fielden SW, Meyer CH. Correcting image blur in spiral, retraced in/out (RIO) acquisitions using a maximized energy objective. *Magn Reson Med*. 2019;81:1806–1817.

24. Chen W, Sica CT, Meyer CH. Fast conjugate phase image reconstruction based on a Chebyshev approximation to correct for B_0 field inhomogeneity and concomitant gradients. *Magn Reson Med*. 2008;60:1104–1111.

25. Weigel M. Extended phase graphs: dephasing, RF pulses, and echoes - pure and simple. *J Magn Reson Imaging*. 2015;41(2):266–95.

26. Tan H, Meyer CH. Estimation of k-space trajectories in spiral MRI. *Magn Reson Med*. 2009;61:1396–1404.

27. Fessler A Jeffrey, “Michigan Image Reconstruction Toolbox,” available at http://web.eecs.umich.edu/~fessler/irt/fessler.tgz.

28. Uecker M, Lai P, Murphy MJ, Virtue P, Elad M, Pauly JM, Vasanawala SS, Lustig M. ESPIRiT–an eigenvalue approach to auto-calibrating parallel MRI: where SENSE meets GRAPPA. *Magn Reson Med*. 2014;71:990–1001.

29. Feng X, Wang Z, Meyer CH. Real-time dynamic vocal tract imaging using an accelerated spiral GRE sequence and low rank plus sparse reconstruction. *Magn Reson Imaging*. 2021;80:106-112.

30. Robson PM, Grant AK, Madhuranthakam AJ, Lattanzi R, Sodickson DK, McKenzie CA. Comprehensive quantification of signal-to-noise ratio and g-factor for image-based and k-space- based parallel imaging reconstructions. *Magn Reson Med*. 2008;60:895- 907.

31. Glover GH, Pelc NJ. Method for correction of image distortion due to gradient non-uniformity. *US Patent* 4,591,789; 1986.

32. Tao S, Trzasko JD, Shu Y, et al. Non-Cartesian MR image reconstruction with integrated gradient nonlinearity correction. *Med Phys*. 2015;42(12):7190-7201.

33. Meyer CH, Pauly JM, Macovski A. A rapid, graphical method for optimal spiral gradient design. In Proceedings of the 4th Annual Meeting of ISMRM, New York, 1996. p. 392.

34. Semelka RC, Kelekis NL, Thomasson D, Brown MA, Laub GA. HASTE MR imaging: description of technique and preliminary results in the abdomen. *J Magn Reson Imaging*. 1996;6:698-699.

35. Vogt FM, Herborn CU, Hunold P, et al. HASTE MRI versus chest radiography in the detection of pulmonary nodules: comparison with MDCT. *AJR Am J Roentgenol*. 2004; 183: 71–78.

Chapter 5: Variable-flip-angle 3D spiral-in/out TSE/SPACE using echo-reordering and concomitant gradient compensation at 0.55 T

5.1 Introduction

Chapter 3 and 4 have discussed the feasibility of 2D TSE with annular spiral-ring trajectories for fast T_2-weighted imaging, providing a promising alternative to the standard Cartesian counterpart. In this chapter, we will switch our focus to 3D TSE imaging.

3D single-slab turbo-spin-echo imaging[1-3], also known as its commercial name "SPACE" (Siemens Healthineers) or "CUBE" (GE Healthcare) or "VISTA" (Philips Healthcare), uses very long echo trains to increase the scan efficiency by varying the flip-angle of the refocusing RF pulses for T_2-weighted imaging in a variety of applications, such as neuro, spine, and musculoskeletal imaging. However, 3D Cartesian sampling remains time-consuming because of its relatively inefficient k-space coverage when prescribing high-isotropic spatial resolution. This problem becomes worse at low-fields due to the inherently lower SNR, requiring several signal averages to maintain clinically acceptable image quality.[4]

Spiral acquisitions cover k-space more efficiently than their conventional Cartesian counterpart, providing a means to reduce scan time or improve SNR.[5,6] Spiral acquisitions are attractive at low fields, where improved field homogeneity enables imaging with prolonged readouts for higher SNR.[7] However, as described previously, the presence of concomitant (Maxwell) fields at low fields may affect the signal pathway in TSE-based imaging, especially

when using high amplitude partition encodings and/or time-varying spiral readouts where the phase error induced by concomitant gradients varies along the echo train.[8-10]

In this chapter, we developed a 3D TSE method using interleaved, rotated spiral-in/out readouts, incorporating a variable-flip-angle approach with echo-reordering to shape the signal evolution, and parallel imaging/compressed sensing to further accelerate the data acquisition at 0.55 T. Additionally, we included sequence modifications and image reconstruction methods to compensate for the concomitant gradient effects along the echo train and during the acquisition window.

5.2 Methods

5.2.1 Pulse sequence design

A simplified timing diagram of the sequence for a sagittal slice orientation is shown in Figure 5-1. Spiral interleaves were rotated in the outer loop, where each excitation acquires a single spiral-in/out arm for every 3D-partition encoding, while the inner loop incremented the partition encodings along the echo direction.

To improve scan efficiency (RO: 4.48 ms, ESP: 7.2 ms), sequence modifications included:

1. Non-spatially-selective refocusing RF pulses were used for the whole-brain excitation.
2. Spoiler gradients (~ 4π dephasing) were combined with 3D partition encodings.
3. Spiral-in/out prewinder and rewinder lobes were played simultaneously with the preceding Gx gradient (spoiler plus the current partition encoding) and the following Gx gradient (spoiler minus the current partition encoding) along the partition direction.
4. Constant-density and variable-density spirals were used for fully-sampled, and 2X-accelerated undersampled data, respectively.

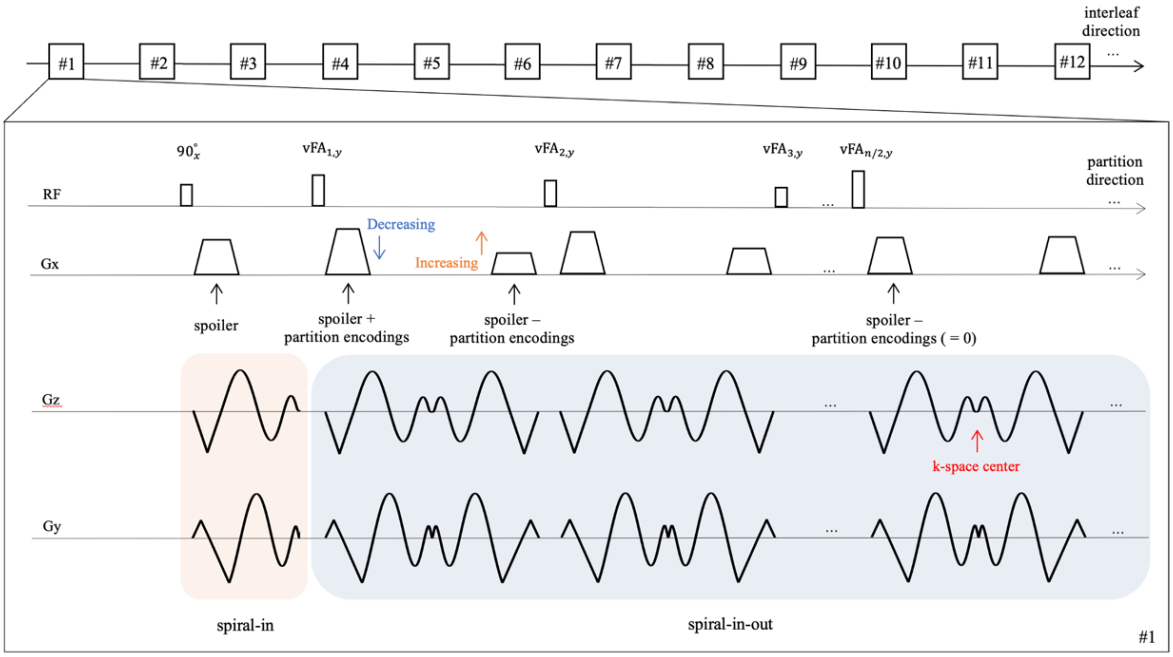

Figure 5-1. Pulse sequence timing diagram including spiral-in gradients for Maxwell compensation before the first refocusing RF pulse, constant-density spiral-in/out readouts for data acquisition, and linearly decreasing partition blips combined with spoiler gradients for kz encodings. Note that the inner loop is for partition lines while the outer loop is for rotated spiral arms. Sagittal orientation was used for all imaging methods.

As mentioned before, encoding gradients with variable amplitudes along the echo train will produce unbalanced concomitant fields that need to be corrected via sequence modifications first.[9,10] To reduce the self-squared Maxwell terms:

1. Gradient de-rating was used for partition encodings.
2. Spiral-in gradients (the first half of the following spiral-in/out readout) were added in the interval between the excitation pulse and the first refocusing pulse, as shown in the orange box.

The utility of the added spiral-in gradients is to not only compensate the self-squared terms for the current spiral-in/out interleaf but also self-balance the quadratic cross-terms induced by using the same overlapping strategy for the spiral-in prewinder lobes and spoiler/partition-

encoding gradients. No additional time was needed for concomitant field compensation, resulting in no sacrifice in scan efficiency.

5.2.2 Variable-flip-angle generation and the effective TE

In this work, a prescribed signal evolution based on asymptotic target pseudo-steady-state stabilization, as described in Ref 3, was firstly determined for gray matter specifically at 0.55 T (T_1 = 800 ms, T_2 = 110 ms). The prospective EPG algorithm was then utilized for the calculation of the variable-flip-angle RF series that meet this target signal curve and the sequence parameters (e.g., ESP), as shown in Figure 5-2A.

The effective TE at the *k*th echo as the k-space center can be determined by the Equation given below[3]:

$$TE_{eff}(k) = -T_2 \ln\left(\frac{s(k)}{s_{coh}(k)}\right) \quad (5\text{-}1)$$

where s and s_{coh} are the normalized signal intensity with and without relaxation effects at each echo, respectively. T_2 is the transverse relaxation time of the current tissue. Figure 5-2B shows the effective TE at different echoes, where the central line of 3D partition encodings was sampled. In this work, the total number of echoes was designed to be 80, and the k-space center was placed at the middle of the echo train (n = 40), thus resulting in an estimated contrast equivalent to a TE of 111 ms with conventional spin-echo imaging.

5.2.3 Trajectory correction

As described in Chapter 2, a gradient impulse response function (GIRF)[11] is a means to characterize the gradient distortions, such as gradient delays, eddy current, and field oscillations, and has been used to predict the actual k-space trajectories by incorporating the pre-calculated

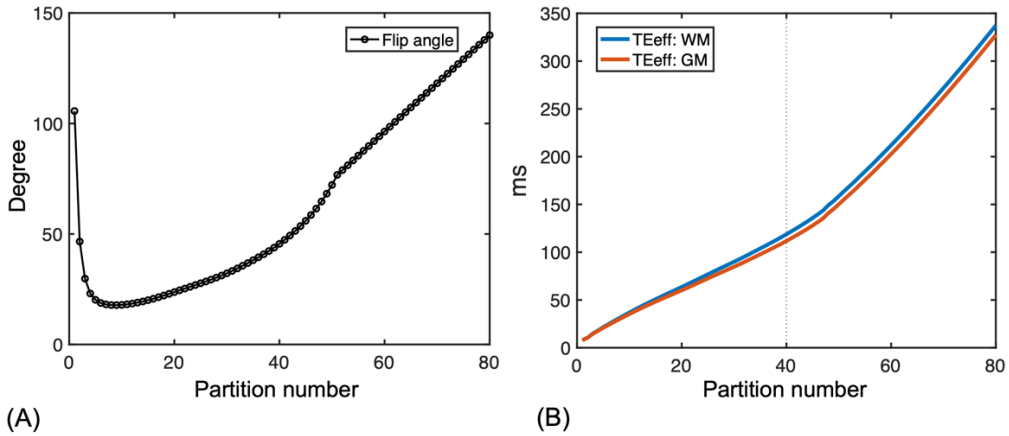

Figure 5-2. (A) The variable-flip-angle RF series generated for 80 partition lines following one excitation. (B) The effective TE for WM and GM varies at different partition number as the k-space center. In this work, the center k-space is set at the middle of the partition-encodings, resulting in an effective TE of 111 ms for GM, 120 ms for GM.

GIRF files (x, y, z axes) into the theoretical trajectories. The calibration was performed in a spherical phantom separately and can be used for future scans with arbitrary orientation planes. To demonstrate the performance of this method on spiral imaging, we compared the phantom images reconstructed from thermotical trajectories, trajectories with anisotropic delay correction, and trajectories with GIRF correction.

5.2.4 Image reconstruction

All images were reconstructed offline in MATLAB. The 2D NUFFT code was used for fully-sampled non-Cartesian image reconstruction, and L1-ESPIRiT[13] was utilized for undersampled datasets. Residual phase errors from concomitant gradients during the readout were corrected by a fast conjugate phase reconstruction method based on a Chebyshev approximation.

5.2.5 Echo reordering and signal normalization

Images reconstructed directly from the raw data may show certain image blurriness, due to the lowpass k-space filter induced by the variable-flip-angle scheme with the 3D-partition-encoding along the echo train. Echo reordering (also called double encoding), which was originally

proposed for 2D interleaved, rotated spiral TSE, improves the performance on the swirl-like artifacts reduction induced by the strong signal variation along the echo train.[12] In this work, echo-reordering was applied whereby the echo order was reversed during the second measurement, and data after signal averaging was further normalized based on a simulated signal decay from EPG and relaxation parameters of gray matter.

5.2.6 MRI experiments

Experiments were performed on a ramped-down 0.55 T MR scanner (prototype MAGNETOM Aera, Siemens Healthcare, Erlangen, Germany) using a 16-channel head/neck coil. For both phantom and healthy volunteer studies (n = 3), images were acquired using spiral SPACE with and without compensation, with Cartesian SPACE as a reference. Both fully-sampled and 2 X undersampled datasets were collected sequentially, and SNR measurements were performed on fully-sampled images only by dividing the mean image intensity in ROIs by the SD of the image intensity outside skull and multiplying the 0.66 Rayleigh distribution correction factor. GRAPPA[14] was utilized for undersampled Cartesian SPACE. Sagittal orientation was used for all imaging, with a $250 \times 250\ mm^2$ FOV and 160 mm slab thickness, which results in 1 mm^3 isotropic whole brain T_2-weighted images. Other sequence parameters can be found in Table 5-1.

Sequences	FOV (mm^3)	TR (ms)	TEeff (ms)	Readout (ms)	ESP (ms)	ETL	# Shots	Acceleration method	Acceleration ratio	Scan time (min)	Spatial Res (mm^3)
Spiral SPACE	250×250×160	2300	111 (GM)	4.48	7.2	80	64	L1-ESPIRiT	1/2	4:54/9:48	1×1×1
Cartesian SPACE	250×250×160	2500	115 (GM)	1.1	3.1	248	250	GRAPPA	1/2	4:59/9:53	1×1×1

Table 5-1. Sequence parameters for Spiral SPACE and Cartesian SPACE at 0.55 T.

5.3 Results

Figure 5-3 shows the signal pathways for white matter, gray matter, fat, and cerebral spinal fluid.

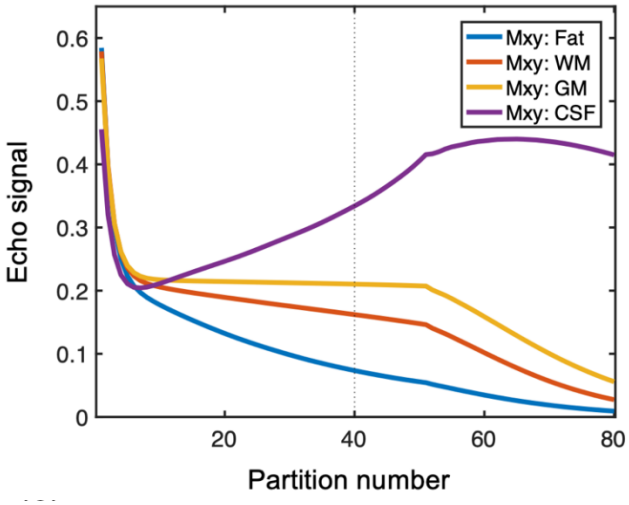

Figure 5-3. The signal pathways of fat, white matter, gray matter, and CSF calculated using the EPG algorithm.

Note that the fat signal is much lower than others, therefore additional fat saturation is not needed.

Figure 5-4 illustrates the performance of the proposed sequence-based Maxwell compensation and trajectory correction in phantom studies. Signal loss can be seen at the top and bottom of Figure 5-4A because of strong concomitant fields along the physical Z axis. After Maxwell compensation, Figure 5-4B shows much improved image quality but still demonstrates edge artifacts and signal shading due to the trajectory infidelity. Applying trajectory correction using the GIRF method (Figure 5-4D) yields better image quality than the anisotropic gradient delay model (Figure 5-4C), as can be easily seen in zoomed regions.

Figure 5-5 shows brain images from spiral SPACE with no concomitant field compensation (top), with sequence-based concomitant field compensation (middle), or with full concomitant field compensation (sequence and reconstruction, bottom). Signal loss and blurring artifacts are substantially reduced when using sequence-based concomitant field compensation (zoomed regions), and the residual blurring artifacts accrued during the readout can be further mitigated through image reconstruction.

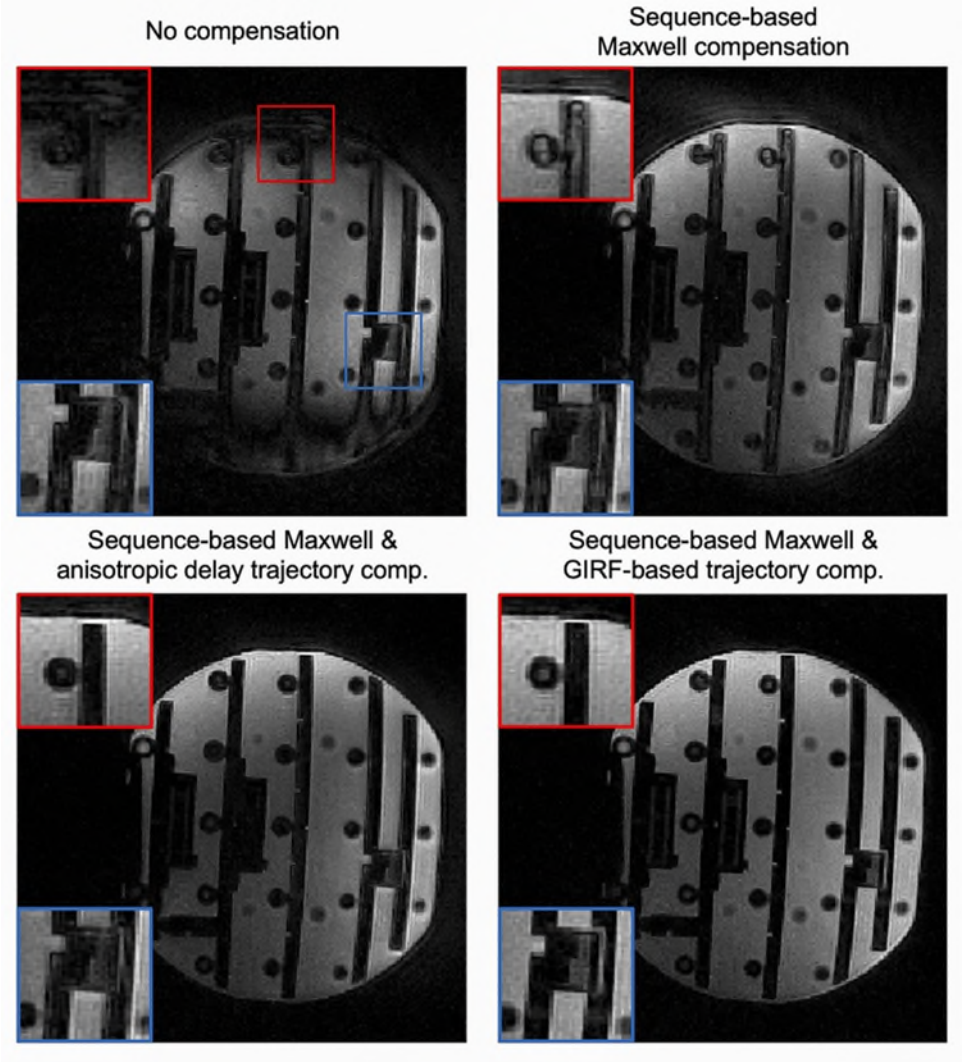

Figure 5-4. Reconstructed images of a sagittal slice in a resolution phantom demonstrating the performance of Maxwell compensation and trajectory correction on image quality (scan time: 2:27 min). (A) Image from spiral SPACE without any compensation. (B) Image with Maxwell compensation only. (C) Image with Maxwell compensation and trajectory correction using anisotropic delay model. (D) Image with Maxwell compensation and trajectory correction using a GIRF model.

Figure 5-6 shows fully-corrected spiral SPACE images without echo-reordering (top) and with echo-reordering (middle), compared to Cartesian SPACE images (bottom). Data after echo-reordering and averaging was further normalized based on a simulated signal decay using EPG, and the corresponding images show improved sharpness compared to those without echo-reordering.

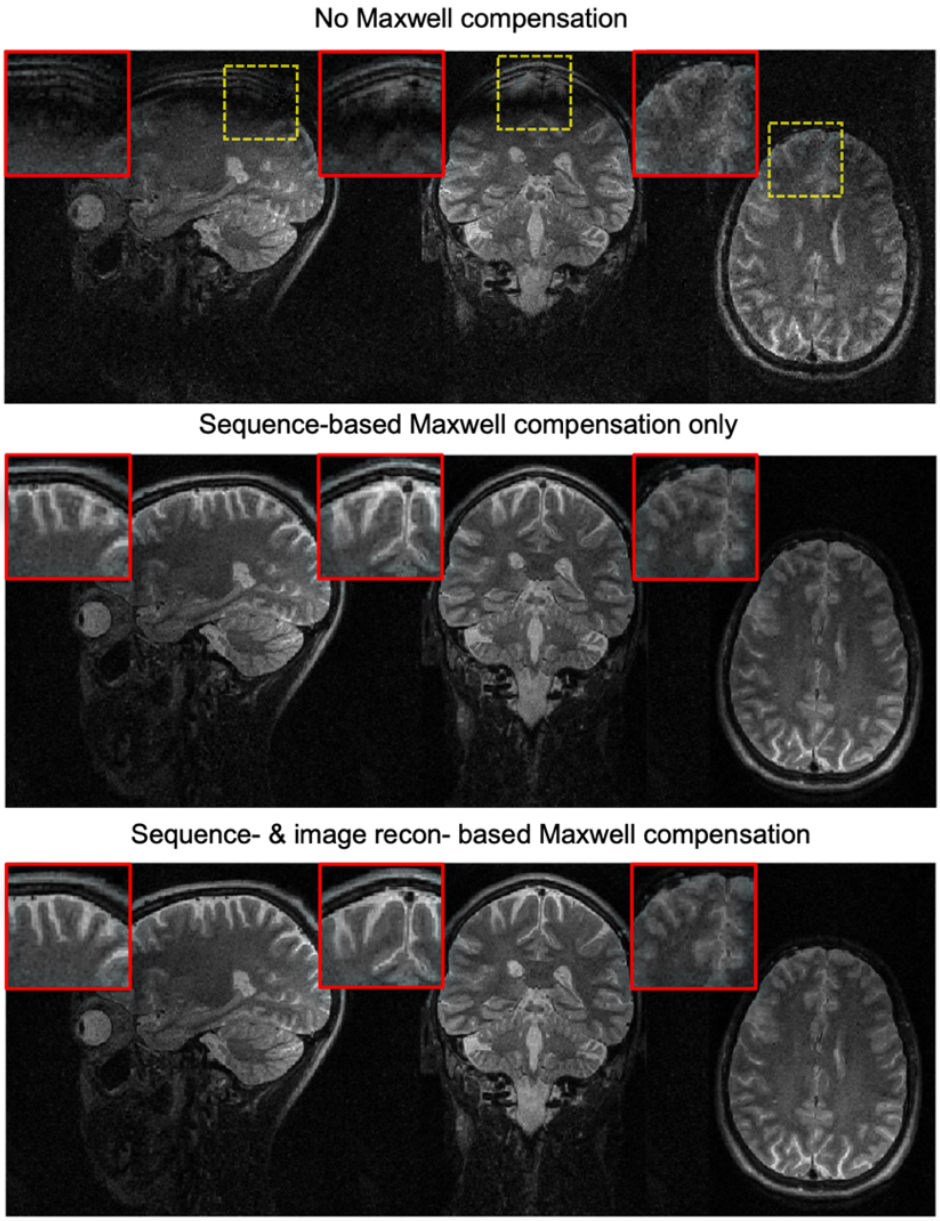

Figure 5-5. Comparison of in vivo images using spiral SPACE with no Maxwell compensation (top), or with sequence-based Maxwell compensation (middle), or with both sequence- and image reconstruction-based Maxwell compensation (bottom) (scan time: 9:48 min). It can be clearly seen that there is regional signal loss and artifacts at the top and bottom of sagittal and coronal slices where Maxwell gradients were strong, while there is global signal loss and blurring for axial slices when the slices were far away from isocenter (zoomed regions).

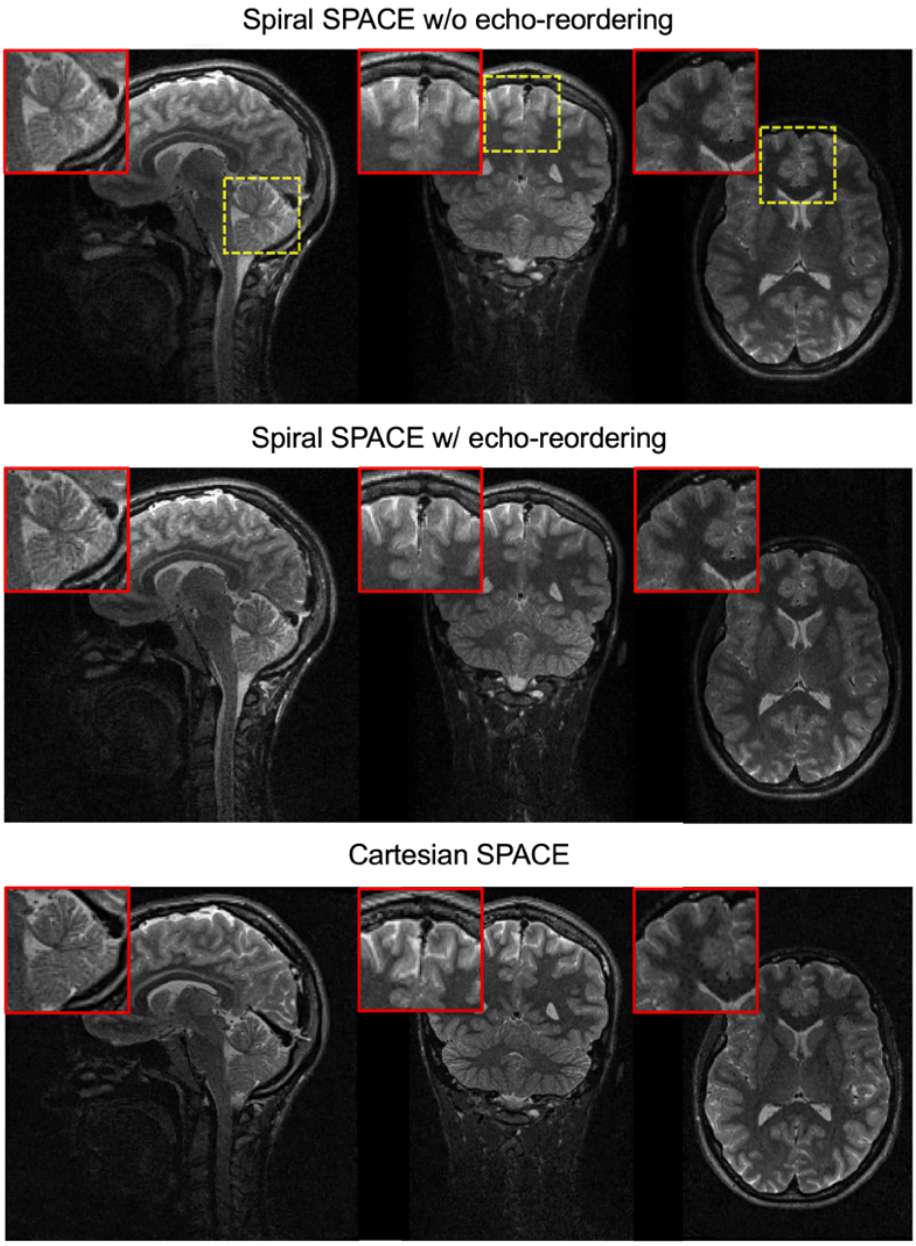

Figure 5-6. Comparison of in vivo fully-corrected images from another healthy volunteer using spiral SPACE without echo-reordering (top), or with echo-reordering and signal normalization (middle), and Cartesian SPACE as the reference (bottom) (scan time: 9:53 min). The images at the top look slightly blurred due to the initial signal decay along the echo train, while those in the middle show improved sharpness with similar image quality compared to the Cartesian counterpart (zoomed regions).

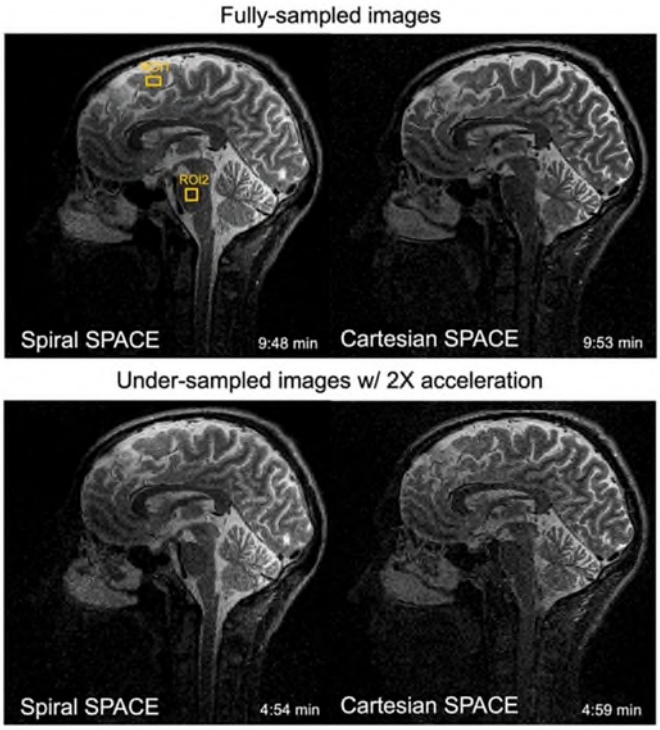

Figure 5-7. Comparison of in vivo images from fully-sampled data (top) and two-fold under-sampled data (bottom), using spiral SPACE (left) and Cartesian SPACE as the reference (right). Total scan time was shown below on each image. SNR of spiral versus Cartesian SPACE: ROI 1 (13.0 vs. 10.9), ROI 2 (7.3 vs. 6.2).

Figure 5-7 displays the images reconstructed with fully-sampled (top, ~10 min scan time) and 2X-undersampled (bottom, ~5 minute scan time) acquisitions by spiral SPACE (left) and Cartesian SPACE (right). Apparent SNR measurements showed increased apparent SNR values when using spiral SPACE over Cartesian SPACE ($17.1 \pm 2.3\%$ gain) for similar scan times.

5.4 Discussion and future work

This work introduces an alternative approach to Cartesian SPACE for 1 mm^3 isotropic whole brain T_2-weighted imaging on a high performance 0.55 T scanner. In this technique, the Cartesian readouts are replaced by interleaved, rotated spiral-in-out trajectories, combined with a variable-flip-angle refocusing train, echo-reordering, and concomitant gradient compensation. Parallel imaging (PI) and compressed sensing (CS) are utilized for further acceleration. Compared to 3D-Cartesian SPACE, this method can be leveraged to mitigate the lower SNR of 0.55 T via the improved SNR efficiency of prolonged spiral trajectory sampling.

The variable-flip-angle RF series play a significant role in extending the useable duration of the echo train and maintaining the signal intensity by slowly increasing the refocusing flip angles to against the signal decay mostly due to the T_2 relaxation. In this study, we generated two versions of variable-flip-angle series shown in Figure 5-8A, and the corresponding signal pathways of gray matter are shown in Figure 5-8B, of which the first has a higher signal amplitude around the central portion of the echo train while the latter has a flatter shape across the echo train. Figure 5-8C and D shows the in vivo images obtained from these two sets of RF series, respectively. It can be easily seen that image C has higher SNR over image D, mostly likely due to more signal energy acquired by echoes from the first variable-flip-angle version. The drawback of the first version compared to the second is it may induce image blurring because of a shorter signal plateau followed by a faster signal decay; however, the blurring can be mitigated by using echo-reordering and signal normalization as described before.

Concomitant gradient compensation is necessary for spiral TSE imaging to obtain high quality images with minimal artifacts. As shown in this work, at low field systems, using spiral gradient waveforms with a maximum amplitude of 25 mT/m and even a short (4.48 ms) readout time will still produce unwanted concomitant gradients that cause severe image degradation. Chapter 4 has presented several general strategies of concomitant gradient compensation methods that can be applied to any type of spiral-based TSE acquisition. Based on that, this chapter describes a special case that uses time-symmetric spiral-in/out readouts in 3D TSE/SPACE. Because of the sampling scheme where in each echo train the spiral readout is the same, no additional bipolar gradients are needed to be inserted into each echo, permitting a short ESP with high scan efficiency. Furthermore, the symmetric property of the spiral-in/out readout enables effective concomitant compensation for both self-squared and quadratic-cross terms by simply

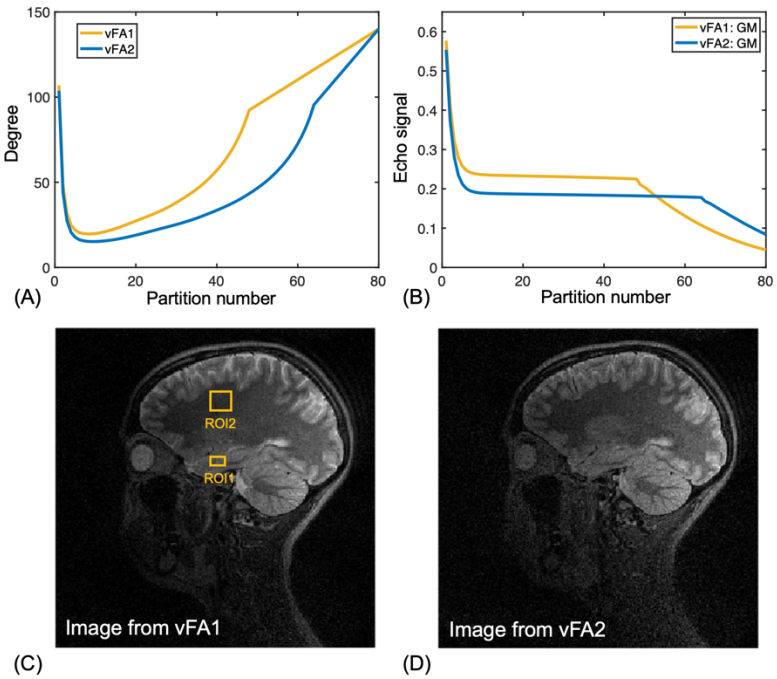

Figure 5-8. Comparison of two sets of variable-flip-angles (A), the corresponding signal pathways of GM (B), and fully-sampled in vivo images (C from version 1, D from version 2). SNR of spiral SPACE from version 1 versus that from version 2: ROI 1 (13.4 vs. 11.1), ROI 2 (8.7 vs. 6.3).

placing the spiral-in arms (the first half of spiral-in/out arms) into the interval between the excitation pulse and the first refocusing pulse, which in turn allows gradient overlapping to further increase the scan efficiency regardless of the induced non-zero cross-terms concomitant phase errors.

In this preliminary implementation, only three healthy volunteers were recruited for in vivo validation; a larger study will be performed in the future. Parallel imaging and compressed sensing enable further data acceleration for spiral SPACE. In this work, we used variable density spiral trajectories and accelerated the data acquisition along the interleave domain. Note that the acceleration can also be performed along the 3D-partition-encoding direction via parallel imaging and/or partial Fourier reconstruction as in conventional Cartesian SPACE. Compared to the vendor provided Cartesian SPACE which uses the GRAPPA acceleration method, the proposed spiral SPACE shows obvious noise reduction yet with some image blurriness due to the L1-constraint. Advanced image reconstruction may be applied to this method, such as deep learning based de-

aliasing and/or de-noising which have shown superior image quality and less computational cost compared to conventional image reconstruction methods.

5.5 Conclusion

In this chapter, we demonstrated a 3D spiral SPACE pulse sequence that incorporates variable flip-angles with an echo reordering strategy, concomitant gradient compensation, and variable-density undersampling for fast T_2-weighted brain imaging at 0.55 T. This approach is an attractive alternative to the conventional Cartesian SPACE for brain images with improved SNR efficiency.

5.6 References

1. Mugler JP 3rd. Optimized three-dimensional fast-spin-echo MRI. *J Magn Reson Imaging*. 2014;39(4):745-767. doi:10.1002/jmri.24542
2. Hennig J, Weigel M, Scheffler K. Calculation of flip angles for echo trains with predefined amplitudes with the extended phase graph (EPG)-algorithm: principles and applications to hyperecho and TRAPS sequences. *Magn Reson Med*. 2004; 51: 68– 80.
3. Busse RF, Hariharan H, Vu A, Brittain JH. Fast spin echo sequences with very long echo trains: design of variable refocusing flip angle schedules and generation of clinical T2 contrast. Magn Reson Med. 2006;55(5):1030-1037.
4. Campbell-Washburn AE et al. Opportunities in interventional and diagnostic imaging by using high-performance low-field-strength MRI. *Radiology* 2019; 293:384-393.
5. Li Z, Wang D, Robison RK, et al. Sliding-slab three-dimensional TSE imaging with a spiral-in/out readout. *Magn Reson Med*. 2016;75:729-738.
6. Wang Z, Allen SP, Feng X, Mugler JP, Meyer CH. SPRING-RIO TSE: 2D T2-Weighted Turbo Spin-Echo Brain Imaging using SPiral RINGs with Retraced In/Out Trajectories. *Magn Reson Med*. 2022;88:601-616.

7. Restivo MC, Ramasawmy R, Bandettini WP, Herzka DA, Campbell-Washburn AE. Efficient spiral in-out and EPI balanced steady-state free precession cine imaging using a high-performance 0.55T MRI. *Magn Reson Med*. 2020;84:2364–2375.

8. Zhou XJ, Tan SG, Bernstein MA. Artifacts induced by concomitant magnetic field in fast spin-echo imaging. *Magn Reson Med*. 1998; 40:582-591.

9. Mugler JP, Campbell-Washburn AE, Ramasawmy R, Pfeuffer J, Meyer, CH. Maxwell Compensation for Spiral Turbo-Spin-Echo Imaging. Proceedings 29th Annual Meeting ISMRM, Virtual meeting. 2021:0003.

10. Wang Z, Feng X, Ramasawmy R, Campbell-Washburn AE, Mugler JP, Meyer CH. Maxwell Field Compensation for 2D Spiral-Ring Turbo Spin-Echo Imaging at 0.55T and 1.5T. In Proceedings of the 31st Annual Meeting of ISMRM, London, UK, 2022:0319.

11. Vannesjo SJ, Haeberlin M, Kasper L, Pavan M, Wilm BJ, Barmet C, Pruessmann KP. Gradient system characterization by impulse response measurements with a dynamic field camera. *Magn Reson Med*. 2013; 69: 583–593.

12. Li Z, Karis JP, Pipe JG. A 2D spiral turbo-spin-echo technique. *Magn Reson Med*. 2018;80:1989–1996.

13. Uecker M, Lai P, Murphy MJ, Virtue P, Elad M, Pauly JM, Vasanawala SS, Lustig M. ESPIRiT–an eigenvalue approach to auto-calibrating parallel MRI: where SENSE meets GRAPPA. *Magn Reson Med*. 2014;71:990–1001.

14. Griswold MA, Jakob PM, Heidemann RM, Nittka M, Jellus V, Wang J, Kiefer B, Haase A. Generalized auto-calibrating partially parallel acquisitions (GRAPPA). *Magn Reson Med*. 2002;47:1202–1210.

Chapter 6: High spatiotemporal real-time cardiac MRI using accelerated spiral-out and spiral-in/out bSSFP pulse sequences at 1.5 T

6.1 Introduction

Chapters 3 – 5 mainly described techniques of rapid spiral imaging for the application in T_2-weighted brain imaging. In Chapter 6, we will concentrate on another application which is extremely time-sensitive: real-time cardiac cine imaging.

In clinical practice, cardiac magnetic resonance images are often acquired during a breath-hold using an electrocardiography-gated (ECG-gated) balanced steady-state free precession (bSSFP) pulse sequence with segmented Cartesian readouts.[1] While producing images with high image quality and spatiotemporal resolution, this conventional method is time-consuming, typically taking 5-6 minutes to cover the whole left ventricle and may be contaminated by ECG-gating and breathing artifacts. Thus, real-time imaging that does not rely on cardiac gating or breath-holding may be advantageous for patients with arrhythmias or who have difficulties in holding their breath.[2-4]

Compressed sensing[5] (CS) has been widely used to accelerate data acquisition in real-time imaging. By exploiting extensive spatiotemporal data redundancy, this technique allows highly undersampled MRI data to be reconstructed without loss of information. Moreover, CS can be extended to further increase imaging speed, for example, by combining it with parallel imaging[6,7] (PI) to exploit joint sparsity across images captured by multiple coils (e.g., k-t SPARSE-SENSE[8-10]), or by combining it with low-rank matrix completion to enable reconstruction of a matrix with

missing entries under low-rank and incoherent conditions (e.g., L&S[11], L+S[12]). To date, the L+S model has been investigated in several applications, including cardiac imaging[12,13], speech imaging[14], and temperature imaging[15], for its ability to achieve good image quality with high acceleration rates.

Since CS-based methods require a sparse representation, incoherent aliasing artifacts are often generated via random undersampling of Cartesian k-space or the use of non-Cartesian sampling patterns.[5] The achievable incoherence from a 2D Cartesian k-space trajectory, however, is relatively low when compared to that from non-Cartesian trajectories. Therefore, non-Cartesian bSSFP sequences, such as radial- or spiral-based trajectories, may improve real-time cardiac MRI by using intrinsic variable density trajectories. Several investigators have demonstrated that radial[10,16-18] and spiral-out[19-21] sampling patterns inherently generate incoherent aliasing artifacts and can achieve high acceleration capability when combined with advanced acceleration methods, both due to their advantageous time-efficiency and inherent robustness to flow and motion artifacts.

In this work, two optimized spiral-based (spiral-out and spiral-in/out) bSSFP pulse sequences were designed and combined with the reconstruction methods to produce highly accelerated cardiac MRI under ungated free-breathing conditions.[22,23] A comparison of these combinations was then conducted in normal volunteers. Finally, the proposed methods were validated against a standard ECG-gated breath-hold cine sequence under whole heart coverage short-axis views.

6.2 Methods

6.2.1 Pulse sequence design

Figure 6-1A shows the timing diagram of real-time spiral-based cine sequences within a single

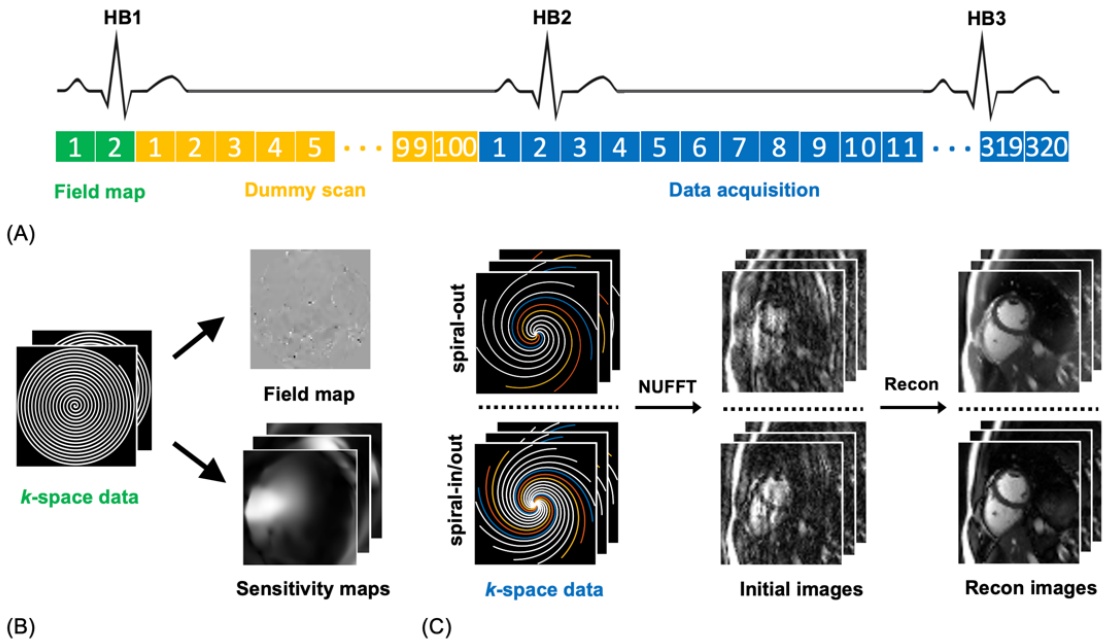

Figure 6-1. (A) Pulse sequence diagram showing the sampling strategy with the field map acquisition, dummy scan, and dynamic data acquisition. (B) The field map and sensitivity maps were estimated using the fully sampled center of k-space data collected from the field map acquisition. (C) Acquisition and reconstruction pipeline used for real-time spiral cine imaging.

scan. A low spatial resolution field map was acquired before bSSFP module using spectral-spatial[24] RF water excitation pulses and two identical, single-shot fully sampled spiral-out arms (green boxes) placed at two-TEs. Dummy cycles (yellow boxes) with a total number of 100 TRs were then used to approach steady state magnetization.[25] Immediately after the pre-scan, dynamic data with a total of 320 spiral arms per slice were collected using a tiny golden angle rotation (blue boxes). Interleaved, rotated spiral-out and spiral-in/out readouts were both evaluated in this study.

For spiral-out gradients, we generated a spiral-out arm constrained by the gradient amplitudes and slew rates in a minimum time[26], along with the following rewinder gradients with zeroth and first-order moments nulling via triangular gradients[20], as shown in Figure 6-2A. The rewinder gradient was designed to overlap with the next slice-selection prewinder to shorten the minimum TR. The resulting spiral-out readout was 1.28 ms in length. Figure 6-2B shows the gradients for a spiral-in/out readout using the algorithm described in Ref. 19. Based on the

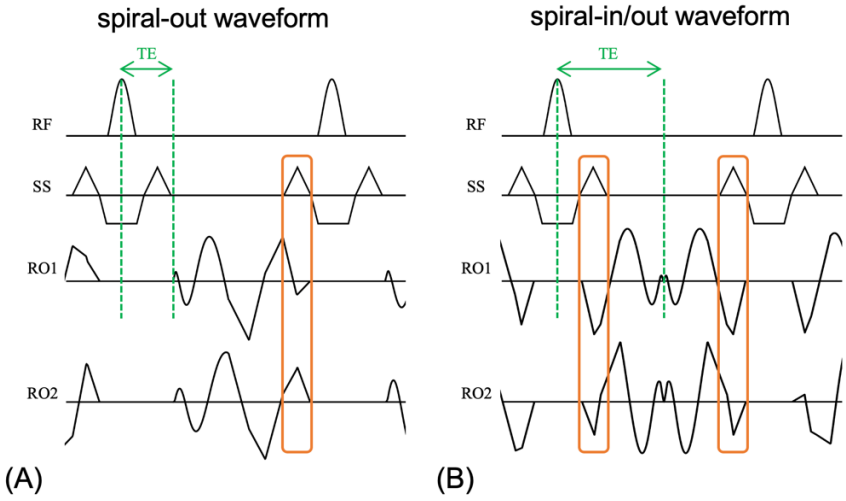

Figure 6-2. Pulse sequence diagrams within one TR using the spiral-out waveforms (A) and spiral-in/out waveforms (B). The orange boxes indicate the overlaps between the readout and the slice selection. Note that the spiral-in/out trajectory has longer acquisition window compared to the spiral-out trajectory for a fixed TR. TE was set to be the minimum one for the spiral-out cine and to be one half of the TR for the spiral-in/out cine, as pointed by green lines.

symmetry of the readout (the preceding time-reversed spiral-in arm and the following spiral-out arm), the spiral-in/out prewinder and rewinder waveforms were designed to overlap with the current slice-selection rewinder and the next slice-selection prewinder gradients, respectively. This property enables a shorter TR or a longer spiral readout compared to the spiral-out trajectory in which the overlap is only feasible on one side. Here, we fixed the TR and chose a longer spiral-in/out readout in our experiments. The resulting spiral-in/out readout was 2.04 ms in length.

Both fully sampled spiral-out and spiral-in/out trajectories contained 64 arms, with a variable sampling density spiral (VDS) using dual-density from 1.5× to 0.3× Nyquist for the spiral-out readout and from 2.3× to 0.4× Nyquist for the spiral-in/out readout. The radius of the density transition was set to be one third of the k-space. Eight sequential arms were combined to reconstruct each cardiac frame with an acceleration ratio of eight. Among interleaves tiny golden-ratio angle increments were used for both spiral-out and spiral-in/out cines to reduce phase disturbances induced by eddy currents in bSSFP acquisition. Tiny golden angles were defined using the golden ratio $\tau = (1 + \sqrt{5})/2$ and the sequence

$$\psi_{N\_sym} = \frac{\pi}{\tau+N-1}, \quad N = 1,2,\ldots, \tag{6-1}$$

for symmetric center-through trajectories such as spiral-in/out.[27] For asymmetric trajectories such as spiral-out, the angle sequence was

$$\psi_{N\_asym} = \frac{2\pi}{\tau+N-1}, \quad N = 1,2,\ldots. \tag{6-2}$$

Here we used the golden angle of 23.63° and 47.26° for the spiral-in/out readout and the spiral-out readout, respectively. The number of slices varies from 10 to 15 depending on the size of the heart. The total acquisition time was 2-3 s per slice in vivo experiments. Other sequence parameters are given in Table 6-1.

6.2.2 Analysis of point spread functions

Point spread functions (PSFs) of spiral-out and spiral-in/out sampling patterns were both computed for each time frame with eight spiral arms per frame. The maximum intensity projection (t-MIP)[28] over the time domain was computed from each series of a total of 80 PSFs. The sidelobe-to-peak ratio (SPR)[5] was then calculated for each trajectory using Equation 6-3 as follows:

$$SPR = \max_{i \neq j}\left(\frac{PSF_{i,j}}{PSF_{i,i}}\right). \tag{6-3}$$

6.2.3 System imperfections

In spiral imaging, k-space infidelity may cause image blurring or distortion[19,29,30]. In this paper, both the spiral-out and spiral-in/out readouts were calculated by the model-based k-space trajectory estimation[19,30]. Off-resonance effects may also cause severe banding artifacts and image blurring. In this work, a Siemens cardiac shim package was used to improve field homogeneity,

							Resolution	
Sequences	FOV (mm²)	TR/TE (ms)	FA	GA	Spiral density	# Interleaves	Spatial (mm³)	Temporal (ms)
spiral-out cine	330×330	4.48/1.05	60°	47.26°	1.5x – 0.3x	8	1.50 × 1.50 × 8	36
spiral-in/out cine	330×330	4.44/2.22	60°	23.63°	2.3x – 0.4x	8	1.51 × 1.51 × 8	36
standard breath-hold cine	330×330	2.7/1.2	60°	-	-	108	1.50 × 1.50 × 8	40

Table 6-1. Sequence parameters for the real-time spiral-out bSSFP cine, the spiral-in/out bSSFP cine, and the standard ECG-gated, breath-hold Cartesian bSSFP cine.

and time-optimized gradients were designed to achieve a TR of less than 5 ms for both spiral cine sequences, along with a linear off-resonance correction[31].

6.2.4 Image reconstruction

The image reconstruction pipeline is shown in Figure 6-1B-C. Coil sensitivity maps were calculated from the fully sampled field map data using ESPIRiT[32]. The L+S reconstruction was implemented using a temporal total-variation (TTV) operator as the sparsifying transform. The regularization parameters for the low-rank term (λ_L) and the sparse term (λ_S) were determined by comparing the resulting image quality for a series of testing values. For simulated datasets, regularization parameters were chosen by evaluating the normalized root mean square error (NRMSE) and structural similarity index[33] (SSIM); for in vivo datasets, parameters were chosen based on the qualitative assessment of the residual aliasing artifacts and visual temporal blurring (see Figure 6-3). For comparison, the CS method was implemented by a similar methodology for parameter selection and by directly enforcing the sparsity on the original matrix, A view-sharing (VS) reconstruction method was also used for reconstruction comparison.

All computations were performed offline in MATLAB (R2020b software; MathWorks, Natick, MA). The NUFFT operator[34,35] was utilized for spiral image reconstruction, and the

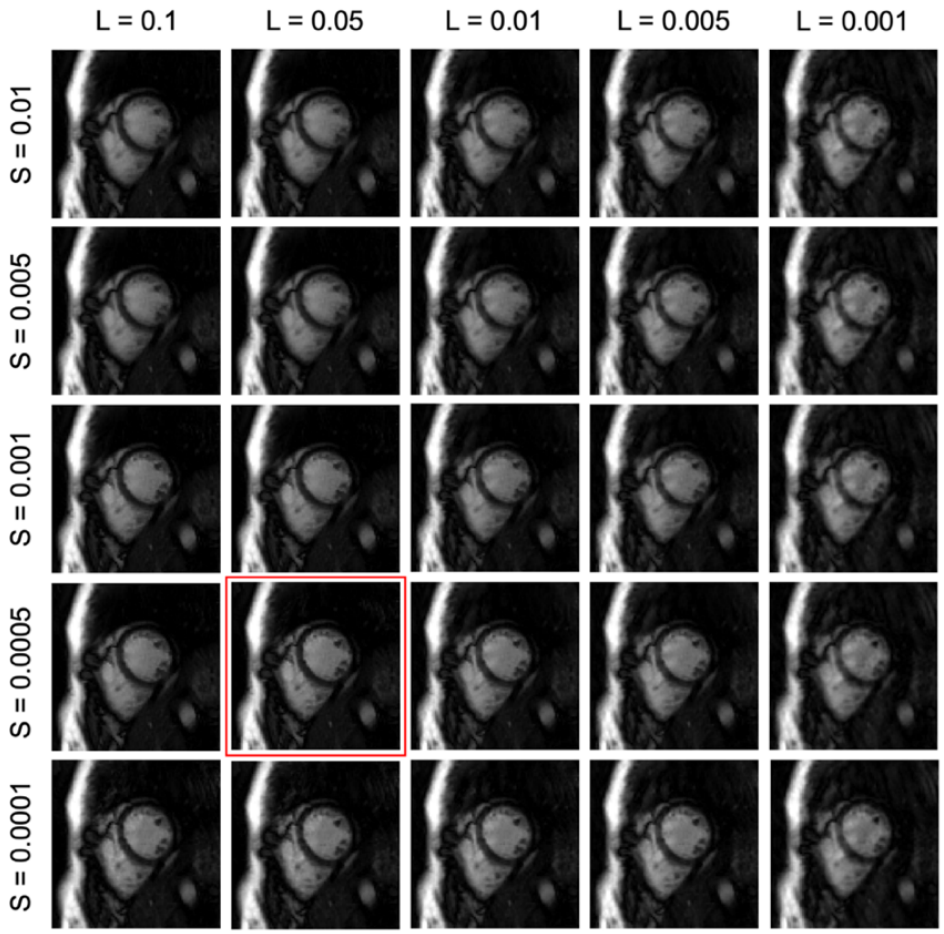

Figure 6-3. Reconstructed images of a given cardiac frame using different values of $\boldsymbol{\lambda_L}$ and $\boldsymbol{\lambda_S}$. The image quality of resulting images is sensitive to the parameter selection, especially when selecting the $\boldsymbol{\lambda_L}$ parameter. At $\boldsymbol{\lambda_L}$ = 0.05 and $\boldsymbol{\lambda_S}$ = 0.0005 (red box), the image has the lowest aliasing and temporal blurring artifacts.

proximal optimized gradient method[36] (POGM) was used for fast L+S iterative convergence. The parameters λ_L of 0.05 and λ_S of 0.0005 were determined for the in vivo L+S images, while a λ_S of 0.0005 was chosen to reconstruct the in vivo CS images.

6.2.5 Simulations

A simulation experiment was performed using the numerical cardiac phantom MRXCAT[37]. Fully sampled Cartesian images were retrospectively undersampled by a factor of eight using two spiral-based undersampling patterns. Image reconstruction was performed using multi-coil CS, and L+S with regularization parameters selected by the aforementioned methodology. NRMSE and SSIM

values were then calculated for both of these two spiral trajectories along with reconstruction methods, to the fully sampled image as a reference.

6.2.6 In vivo experiments

All in vivo studies were performed on a 1.5T scanner (MAGNETOM Avanto, Siemens Healthcare, Erlangen, Germany) with a 32-channel anterior-posterior surface coil array. Seven healthy volunteers (five males and two females) participated in this work with written informed consent prior to the experiment. Whole-heart coverage short-axis views were imaged by these two real-time spiral cine sequences under an ungated, free-breathing condition, and by the standard ECG-gated Cartesian cine sequence during a breath-hold as a reference. For each set of experiments, the three pulse sequences were run consecutively at the same image plane with the same cardiac shimming settings. The relevant parameters for this standard technique can be found in Table S1.

6.2.7 Image assessment

A blind rating of the diagnostic quality of cine datasets (n = 7) was performed by two cardiologists, with a 1 (nondiagnostic) - 5 (excellent) scale. Differences in qualitative image quality ratings for real-time spiral bSSFP cines along with image reconstruction methods were analyzed, followed by pairwise comparisons using the Wilcoxon signed rank test. Furthermore, to validate the proposed two real-time spiral cine sequences with the L+S reconstruction method against the standard breath-hold Cartesian cine sequence, short-axis movies from all the subjects were then rated and compared, as well.

A quantitative calculation of image contrast between the blood pool and the myocardium was performed, and a similar method described in Ref 17 and 21 was used to measure the average blood pool and myocardial signal intensity in the end-diastolic midventricular image for each

subject. Edge sharpness (mm^{-1}) was also calculated in every cardiac phase of the midventricular orientation.[17,21] Differences in image contrast and mean edge sharpness for the two real-time spiral cine techniques with L+S reconstruction and the standard cine sequence were analyzed, and pairwise comparisons were then implemented via the Wilcoxon signed rank test.

6.2.8 Ejection fraction calculation

The left ventricular end-diastolic volume (LV EDV) and end-systolic volume (LV ESV) were measured, and the left ventricular ejection fraction (LV EF) was then calculated for the real-time spiral cines and the standard cine. The agreements in LV EF between the proposed methods and the reference were calculated using a Bland-Altman analysis.

6.3 Results

6.3.1 Simulations

Figure 6-4 shows that for spiral-in/out cine, its maximum aliasing (SPR: 0.074) is lower within a circular region near the PSF peak, compared to that from spiral-out cine (SPR: 0.098). For a fixed TR, a longer spiral-in/out readout shows a higher level of incoherence than the spiral-out readout, which results in improved characteristics for sparse image reconstruction.

Figure 6-5 shows the numerical phantom images and the x-t profiles reconstructed from the spiral-out and spiral-in/out readouts using CS and L+S reconstruction methods, and the fully sampled image as the reference. The results indicate that all methods lead to a high SSIM value (> 0.90) and a low NRMSE value (< 3%). Among these methods, the spiral-in/out cine with L+S method has the lowest-intensity image artifacts (red arrows) and maintains the best temporal information (green arrows).

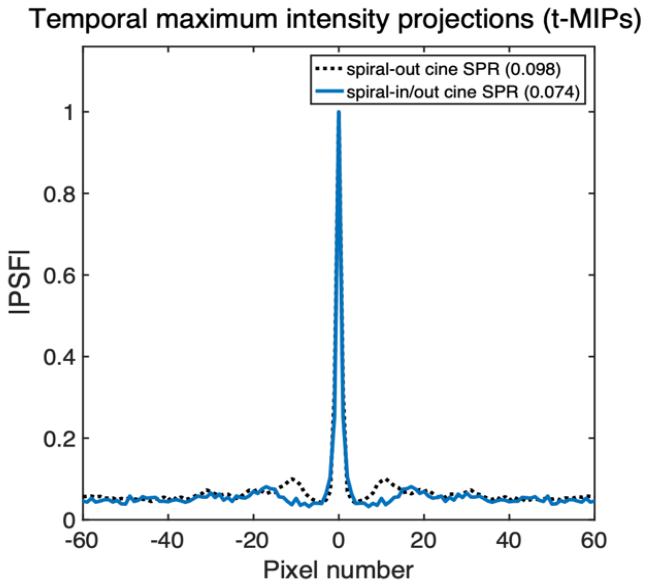

Figure 6-4. Analysis of PSFs over time for the spiral-out and spiral-in/out readouts. The results show the central 120 pixels of signal intensities across a line over the central region of the t-MIPs (each having 220 x 220 pixels) for both spiral trajectories.

6.3.2 In vivo studies

Figure 6-6 shows end-diastolic and end-systolic frames from one short-axis ungated, free-breathing experiment using spiral-out (left) and spiral-in/out (right) bSSFP sequences with VS (top), CS (middle), and L+S (bottom) reconstruction methods. The images use a cropped view containing mainly the heart. The x-t profiles show the reconstructed images along the profile denoted by the dashed line. The results from VS show obvious noise-like aliasing artifacts, while those from CS and L+S both demonstrate clear image quality improvement, and the L+S method performs best, in terms of artifacts (red arrows) and temporal details (green arrows). The corresponding image ratings are shown in Figure 6-7.

Figure 6-8 shows images from one healthy volunteer using spiral-out cine (top) and spiral-in/out cine (middle) with L+S reconstruction, and the standard Cartesian cine (bottom). Fine papillary muscles (red arrows) are clearly visualized in ventricles in images from the real-time spiral cines. Green arrows pointing to x-t profiles demonstrate the preserved temporal fidelity of

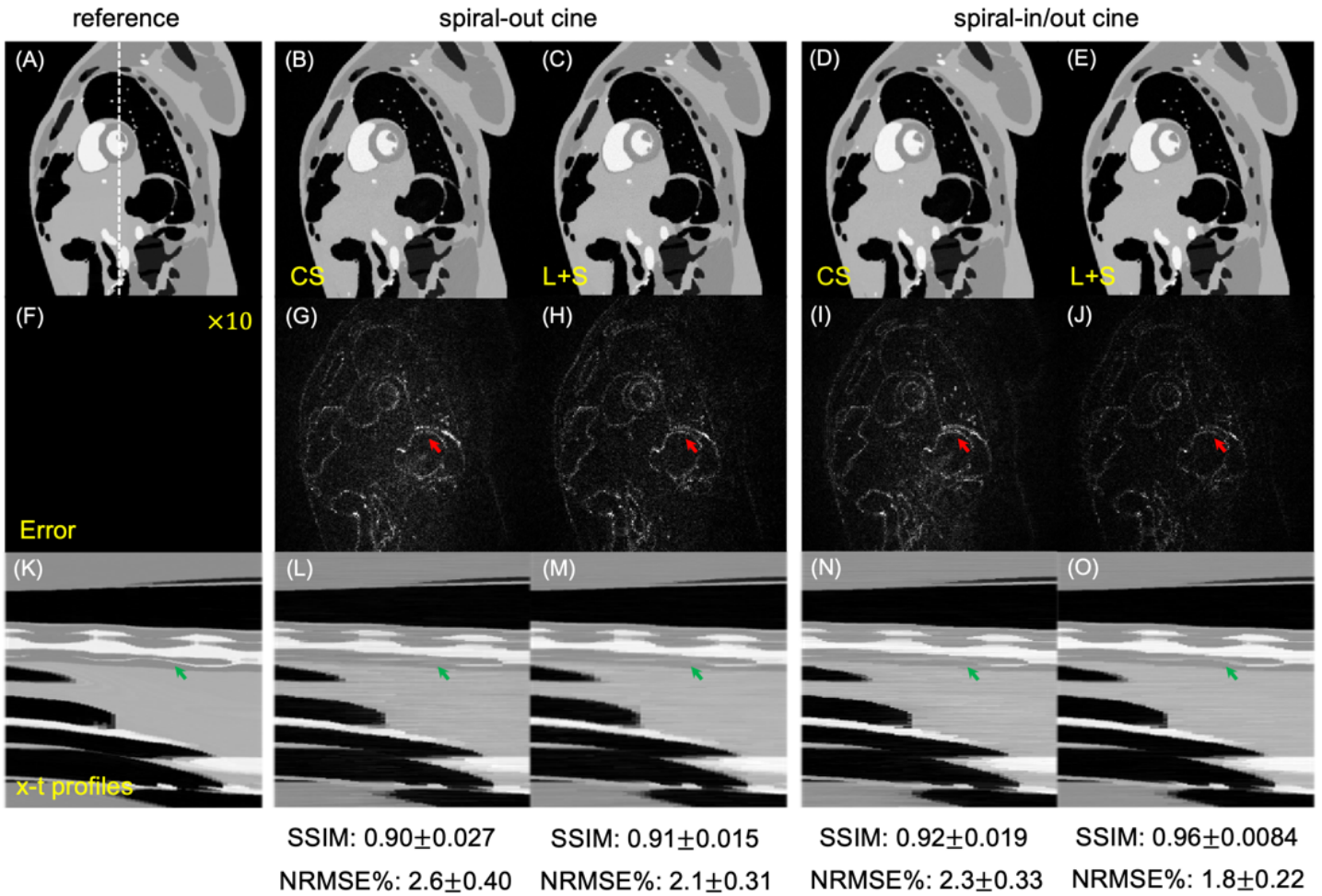

Figure 6-5. Simulation of a numerical cardiac phantom for the spiral-out cine and the spiral-in/out cine with CS and L+S reconstruction methods (A-E). Absolute difference images (F-J) relative to the fully sampled reference (e.g., (G) shows the difference between image (B) and the reference image (A)), and x-t profiles (K-O), as well as the corresponding SSIM and NRMSE values (mean ± standard deviation), are shown for comparison. The error maps are windowed by scaling the image intensity by a factor of ten. Red arrows show the regions with image artifacts, while green arrows show the temporal information.

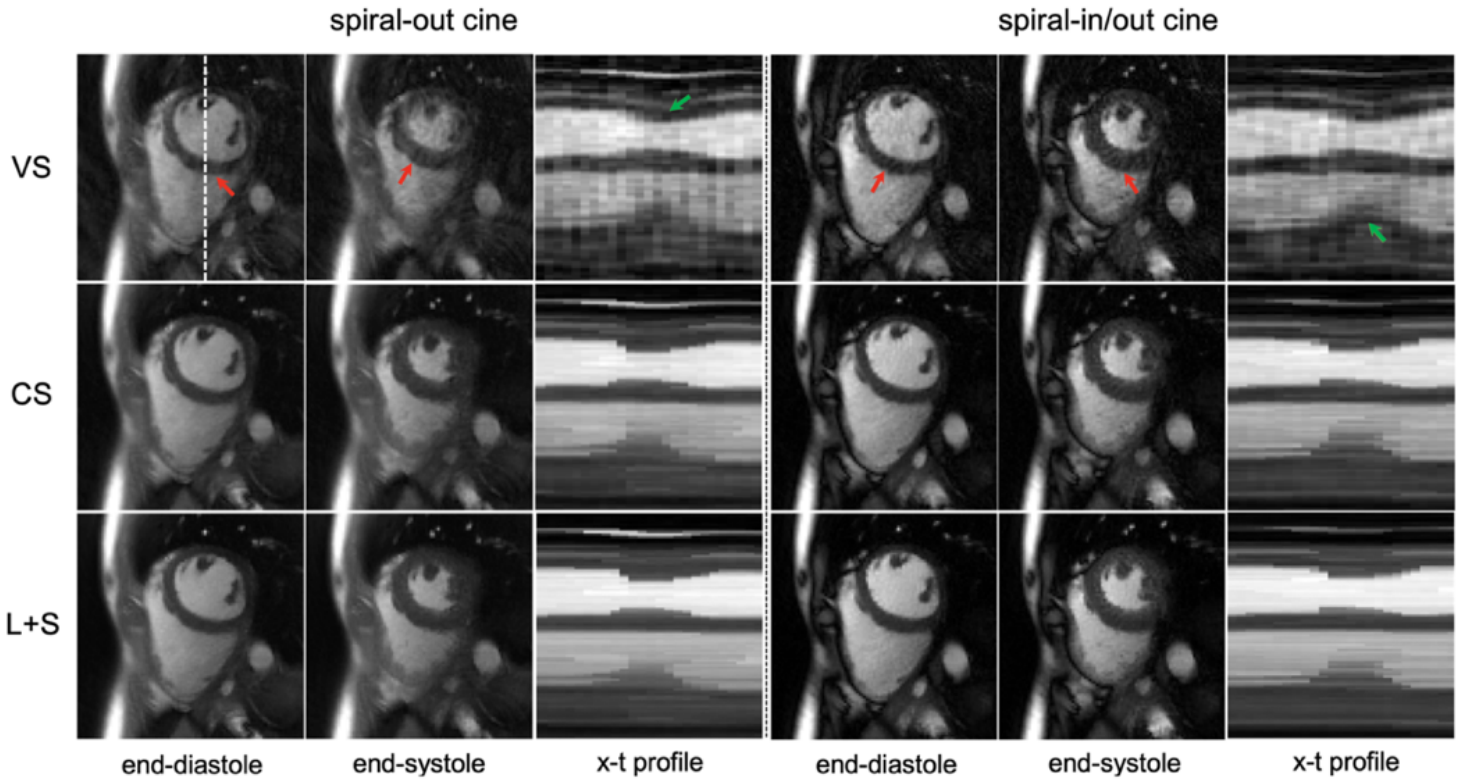

Figure 6-6. Comparison of reconstructed end-diastolic and end-systolic frames from a midventricular short-axis view, using the spiral-out (left) and the spiral-in/out (right) bSSFP sequences with VS (top row), CS (middle row), and L+S (bottom row) reconstruction methods. Images were acquired under ungated, free-breathing conditions. The white dashed line represents the location used to derive the x-t profiles. Red arrows point to the structures that show image artifacts, while green arrows show temporal details. The L+S method performs best in terms of artifacts and temporal details.

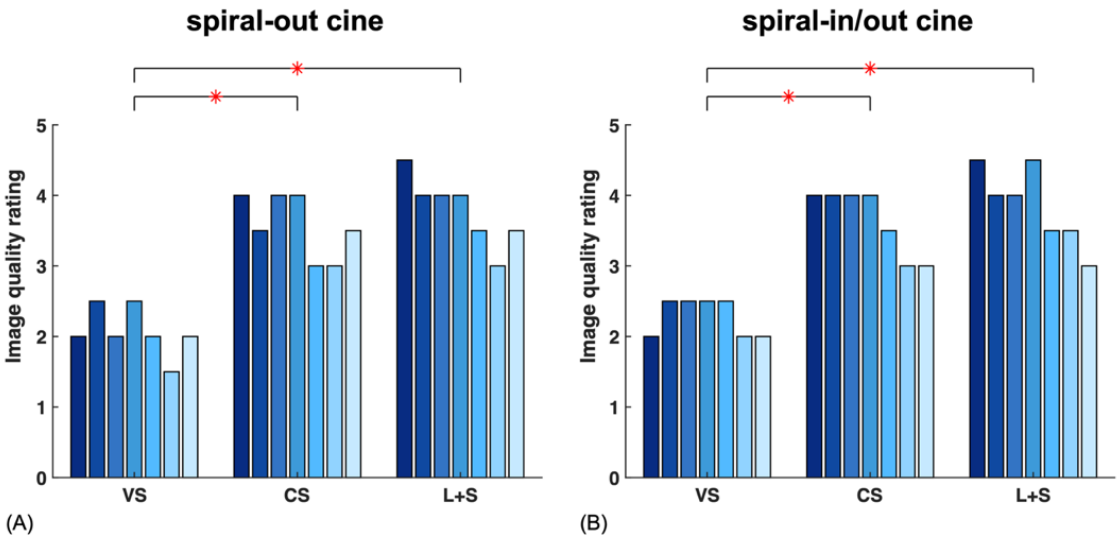

Figure 6-7. Image quality ratings among all subjects (n = 7). The bar plot shows the scores for images from the spiral-out cine (A) and from the spiral-in/out cine (B) using VS, CS, and L+S. All scores were graded in a blinded fashion by two cardiologists, each scored from 1 to 5 (worst to best). Asterisks indicate a significant difference ($p < 0.05$).

these two real-time spiral cine techniques with a slight difference compared to that of the standard Cartesian cine, potentially due to the through-plane respiratory movement in real-time techniques.

Figure 6-9 shows representative sets of short-axis cine images from one healthy volunteer, using real-time spiral-out and spiral-in/out bSSFP sequences with L+S reconstruction, and the breath-hold reference. Both of the spiral-based sequences produce overall good diagnostic image quality (3.8 ± 0.8 for spiral-out cine and 3.9 ± 0.7 for spiral-in/out cine), while the spiral-in/out cine shows a visually better image contrast between the blood pool and the myocardium than the spiral-out cine (3.8 ± 0.6 versus 2.9 ± 0.5). Edges were sharper in standard cine images (0.69 ± 0.14) compared to spiral-out cine images (0.58 ± 0.13) and spiral-in/out cine images (0.59 ± 0.13). The standard breath-hold images (bottom row) show blurring artifacts, potentially because of a poor ECG-trigger signal. The comparison of the global image quality, the measured image contrast, and edge sharpness among techniques can be seen in Figure 6-10.

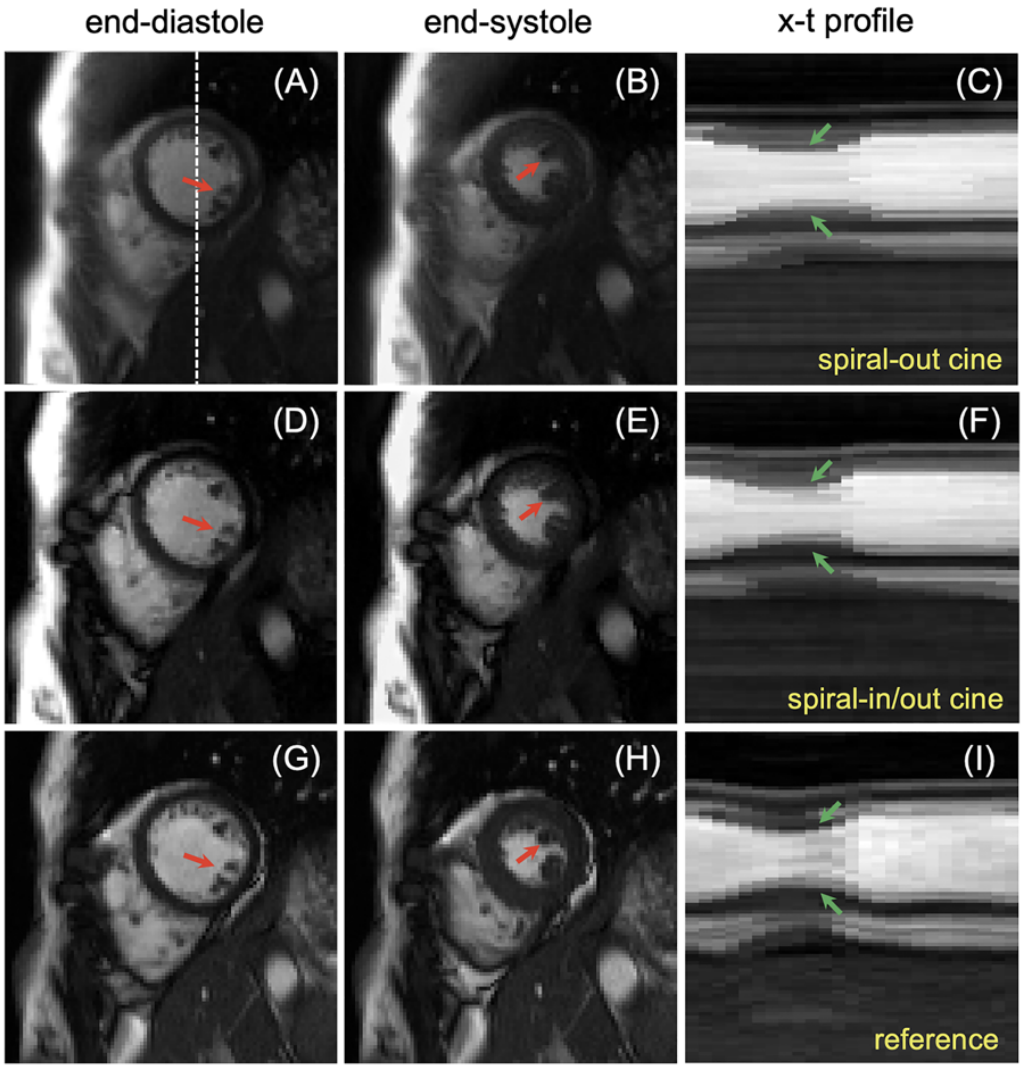

Figure 6-8. Comparison of reconstructed cardiac frames from a healthy volunteer using free-breathing spiral-out cine (A-C), free-breathing spiral-in/out cine (D-F), and standard breath-hold Cartesian cine (G-I). The spiral images were reconstructed using the L+S method. End-diastolic and end-systolic images are shown in the first and second columns, respectively. The white dashed line represents the location used to derive the x-t profile. Red arrows point to structures that show fine papillary muscles in ventricles, while green arrows indicate the preserved temporal fidelity. The spiral-in/out bSSFP images show closer image contrast between the blood pool to myocardium to that of standard Cartesian cine images than the spiral-out bSSFP images.

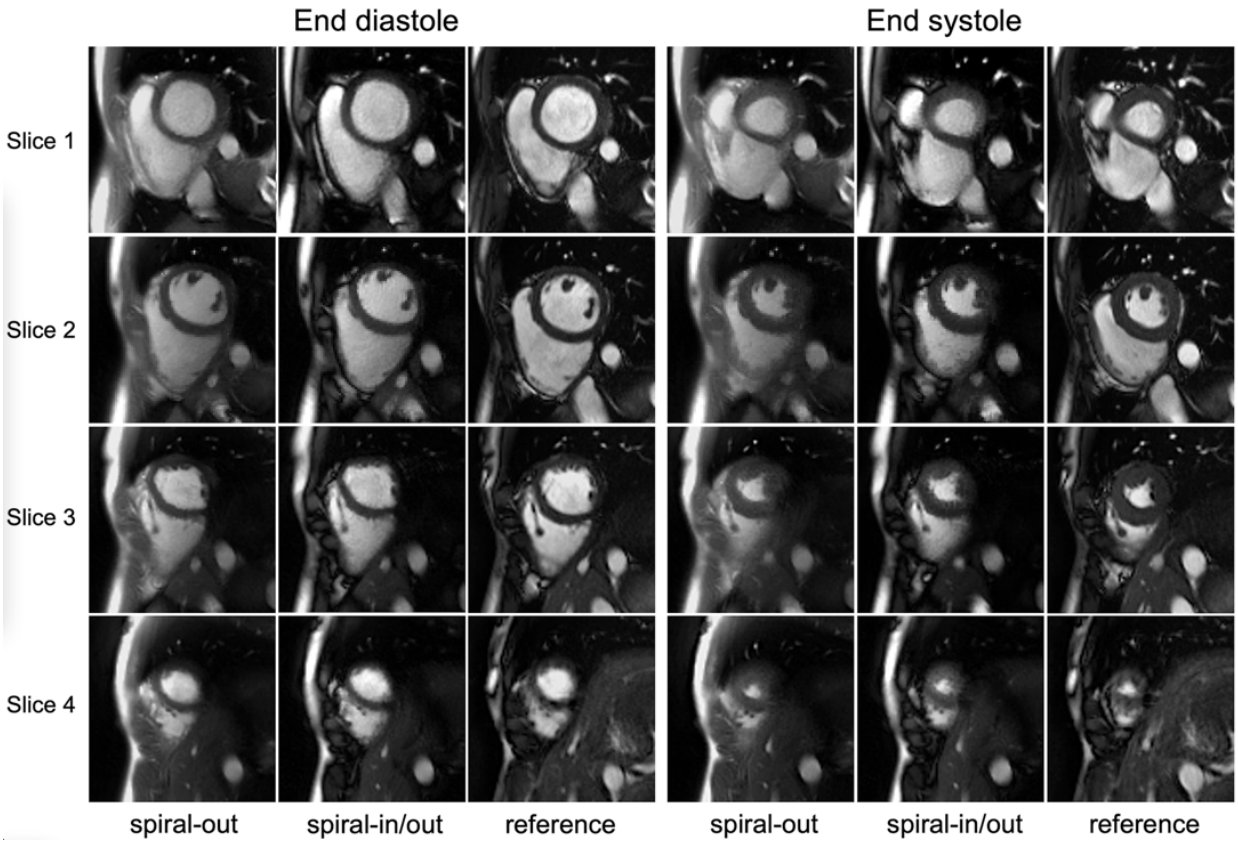

Figure 6-9. Comparison of short-axis cardiac images from free-breathing spiral-out (left column), free-breathing spiral-in/out (middle column), and standard breath-hold Cartesian cine (right column) in one healthy volunteer. For each method, four slices at end diastole (left) and end systole (right), from apex (bottom) to base (top) are shown.

The Bland-Altman plots show the comparison of LV EF between Cartesian cine and the spiral-out cine (Figure 6-11A), and between Cartesian cine and the spiral-in/out cine (Figure 6-11B). The mean differences in LV EF were -1.5% and -1.6% for the spiral-out cine and spiral-in/out cine, respectively, compared to the breath-hold reference. There was no statistical significance among these three methods ($p > 0.1$), establishing the accuracy of estimating LV EF using these two real-time spiral cine techniques. There was no significant difference in mean LV EDV ($p > 0.1$). However, the mean LV ESV was significantly overestimated ($p < 0.05$) using both of the real-time spiral cine techniques compared to those using the conventional breath-hold cine (see Table 6-2).

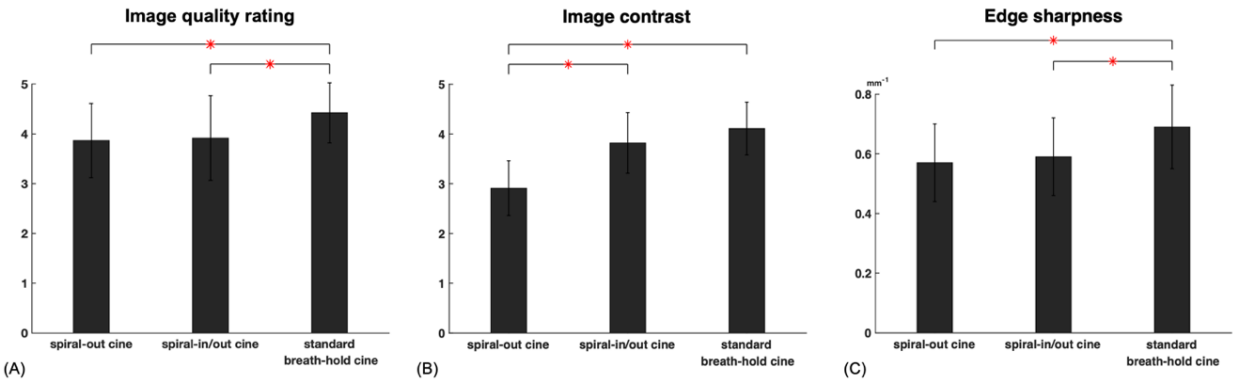

Figure 6-10. Assessment of image quality of real-time spiral-out cine, real-time spiral-in/out cine, and standard breath-hold Cartesian cine images. (A) Subjective assessment of global image quality. (B) Quantitative assessment of measured image contrast. (C) Quantitative assessment of edge sharpness (unit: mm^{-1}). The error bars represent standard deviations. Asterisks indicate a significant difference ($p < 0.05$).

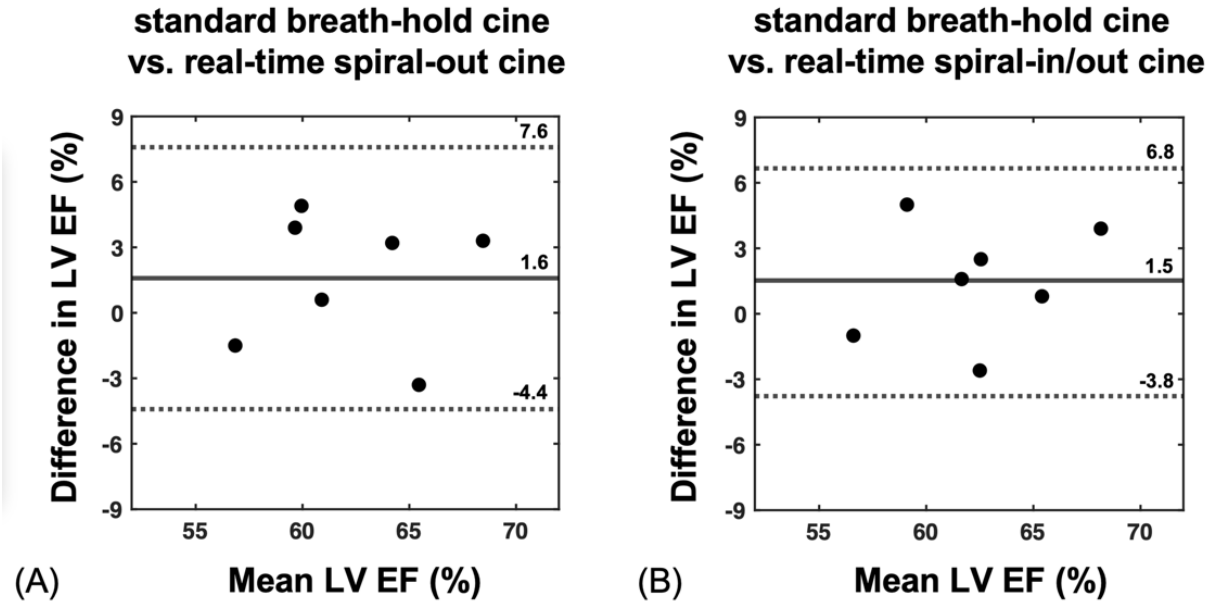

Figure 6-11. Bland-Altman plots of LV EF for the subjects with whole-heart coverage. (A) Bland-Altman plot of EF calculated from the standard Cartesian cine results and the spiral-out cine results. Mean = (Cartesian cine + spiral-out cine)/2, Difference = Cartesian cine - spiral-out cine. (B) Bland-Altman plot of EF calculated from the standard Cartesian cine results and the spiral-in/out cine results. Mean = (Cartesian cine + spiral-in/out cine)/2, Difference = Cartesian cine - spiral-in/out cine. Spiral images were reconstructed using the L+S method.

	spiral-out cine	spiral-in/out cine	standard breath-hold cine
LV EDV (mL)	152 ± 35	154 ± 38	156 ± 31
LV ESV (mL)	57 ± 17*	58 ± 19**	53 ± 14*,**
LV EF (%)	60 ± 6	61 ± 7	63 ± 5

Table 6-2. Comparison of the averaged LV EDV, LV ESV, and LV EF among spiral-out cine, spiral-in/out cine, and the standard breath-hold cine. ± means standard deviation. * and ** mean the matched pairs are statistically significant ($p < 0.05$).

6.4 Discussion

In this chapter, we developed and validated both spiral-out and spiral-in/out bSSFP sequences combined with a L+S reconstruction method to achieve highly accelerated, ungated, free-breathing real-time cine with 1.5 mm in-plane isotropic spatial resolution and 36 ms temporal resolution. The total scan time for whole LV coverage was greatly reduced from approximately 5~6 minutes with multiple breath-holds to 30~45 seconds with continuous scanning during free-breathing. The performance of these two sequences for cardiac function was compared to the standard Cartesian cine using protocols with similar spatiotemporal resolution, demonstrating there was good agreement for LV EF calculation between real-time spiral techniques and the conventional breath-hold Cartesian cine.

k-Space misregistration in spiral imaging due to gradient infidelity affects the image quality of spiral images, especially for cardiac scanning with oblique slice orientations. In our implementation, anisotropic gradient delays for each axis were calculated, along with eddy current coefficients for estimating the actual k-space trajectories. These measured system parameters need to be calibrated once and can then be used for future scans.[19,30] B_0 inhomogeneities degrade spiral images. In this work, short spiral readouts with acquisition windows of less than 2.5 ms resulted in acceptable blurring artifacts which were further reduced by a simple linear off-resonance correction.

Spiral k-space scanning has been previously investigated for accelerating ungated, free-breathing cardiac imaging, either with spoiled gradient echo (GRE) sequences[13,38] or with bSSFP sequences[21]. A GRE strategy may have certain advantages over bSSFP acquisition for its insensitivity to off-resonance effects, allowing a longer spiral readout for a more efficient sampling; however, image contrast of GRE images between the blood pool and the myocardium is inferior compared to that of bSSFP images, which may lead to difficulty and inaccuracy in demarcation of the endocardial surface when calculating LV EF. Steeden et al.[21] used a short uniform density spiral-out (UDS) trajectory with a zeroth order moment rewinder to reduce the off-resonance effects in bSSFP sequences, yet this approach limits its spatial resolution due to a relatively low sampling efficiency within each TR. The unbalanced first moment of the readout gradient may also induce undesirable phase-related in-plane motion and inflow artifacts[20]. In this work, a VDS design instead of the UDS design was used for both spiral-out and spiral-in/out trajectories, which has been demonstrated to suppress udersampling aliasing artifacts[39,40] by sampling more at the center but less at the outer portion of k-space, thus increasing the level of incoherence that is important for CS-related approaches. Furthermore, the spiral-out trajectory was designed with time-optimized first-order moment nulling gradients and the spiral-in/out trajectory has intrinsic first-order compensation via symmetry, with each resulting in better flow artifact suppression than a spiral trajectory with zeroth order compensation only. Comparing these two spiral-based cine sequences, the refocusing mechanism of the spiral-in/out readout, similar to that in the Cartesian readout, may account for a better image contrast compared to the spiral-out readout, because the signal at the middle of TR has more T_2-weighted refocused spins. In this study, the real-time spiral-in/out cine with L+S image reconstruction produced the closest image quality to that of the standard ECG-gated, breath-hold Cartesian cine, in terms of image contrast and spatiotemporal

standard ECG-gated, breath-hold Cartesian cine, in terms of image contrast and spatiotemporal resolution.

This work has several limitations. The main limitation is that no patients were studied, so a patient study is needed for clinical validation of the proposed real-time spiral cine methods. For example, patients with arrhythmia, which may produce inferior image quality associated with irregular ECG signals used in conventional Cartesian cine, can be recruited for clinical evaluation. Second, the comparison of LV EF values among methods validated that these two real-time spiral cine sequences achieved good agreement in the accuracy of LV EF quantification, but a larger study could provide a more reliable analysis of functional parameter quantification. Third, end-diastolic and end-systolic frames from real-time spiral cine scans without ECG gating may not be matched to the same time points from the standard ECG-gated cine scans. The frame mismatch problem becomes more severe when imaging subjects with variable breathing patterns, although in general, free-breathing induced through-plane motion seems to have an acceptable effect on the LV EF quantitative measurements. One simple solution to minimize this discrepancy is to perform real-time cine with 3-4 s short breath-holding, but this study did not explore this. Fourth, the computational cost for offline image reconstruction in MATLAB is currently around 2~3 minutes. Optimizing the code and implementing the pipeline in C++ may enable real-time image reconstruction on commercial scanners.

6.5 Conclusion

In this chapter, two spiral-based (spiral-out, spiral-in/out) bSSFP sequences with low-rank plus sparse image reconstruction were presented for highly accelerated real-time cine to evaluate the cardiac function. These methods demonstrated cardiac cine imaging without ECG gating during

free breathing with diagnostic image quality in normal volunteers, suggesting the potential for clinical real-time cardiac MR imaging.

6.6 References

1. Carr JC, Simonetti O, Bundy J, Li D, Pereles S, Finn JP. Cine MR angiography of the heart with segmented true fast imaging with steady-state precession. *Radiology*. 2001;219:828–834.
2. Setser RM, Fischer SE, Lorenz CH. Quantification of left ventricular function with magnetic resonance images acquired in real time. *J Magn Reson Imaging*. 2000;12:430–438.
3. Barkhausen J, Goyen M, Ruhm SG, Eggebrecht H, Debatin JF, Ladd ME. Assessment of ventricular function with single breath-hold real-time steady-state free precession cine MR imaging. *AJR Am J Roent-genol*. 2002;178:731–735.
4. Nita N, Kersten J, Pott A, Weber F, Tesfay T, Benea M-T, Metze P, Li H, Rottbauer W, Rasche V, Buckert D. Real-Time Spiral CMR Is Superior to Conventional Segmented Cine-Imaging for Left-Ventricular Functional Assessment in Patients with Arrhythmia. *Journal of Clinical Medicine*. 2022; 11(8):2088. https://doi.org/10.3390/jcm11082088
5. Lustig M, Donoho D, Pauly JM. Sparse MRI: The application of compressed sensing for rapid MR imaging. *Magn Reson Med*. 2007;58: 1182–1195.
6. Pruessmann KP, Weiger M, Scheidegger MB, Boesiger P. SENSE: Sensitivity encoding for fast MRI. *Magn Reson Med*. 1999;42:952–962.
7. Griswold MA, Jakob PM, Heidemann RM, Nittka M, Jellus V, Wang J, Kiefer B, Haase A. Generalized auto-calibrating partially parallel acquisitions (GRAPPA). *Magn Reson Med*. 2002;47:1202–1210.
8. Otazo R, Kim D, Axel L, Sodickson DK. Combination of compressed sensing and parallel imaging for highly accelerated first-pass cardiac perfusion MRI. *Magn Reson Med*. 2010;64:767–776.
9. Feng L, Srichai MB, Lim RP, Harrison A, King W, Adluru G, Dibella EV, Sodickson DK, Otazo R, Kim D. Highly accelerated real-time cardiac cine MRI using k-t SPARSE-SENSE. *Magn Reson Med*. 2013;70: 64–74.

10. Feng L, Grimm R, Block KT, Chandarana H, Kim S, Xu J, Axel L, Sodickson DK, Otazo R. Golden-angle radial sparse parallel MRI: combination of compressed sensing, parallel imaging, and golden angle radial sampling for fast and flexible dynamic volumetric MRI. *Magn Reson Med*. 2014;72:707–717.

11. Lingala S, Hu Y, Dibella E, Jacob M. Accelerated dynamic MRI exploiting sparsity and low-rank structure: k-t SLR. *IEEE Trans Med Imag*. 2011;30:1042–1054.

12. Otazo R, Candes E, Sodickson DK. Low-rank plus sparse matrix decomposition for accelerated dynamic MRI with separation of background and dynamic components. *Magn Reson Med*. 2014;73(3):1125-1136.

13. Zhou R, Yang Y, Mathew RC, et al. Free-breathing cine imaging with motion-corrected reconstruction at 3T using SPiral Acquisition with Respiratory correction and Cardiac Self-gating (SPARCS). *Magn Reson Med*. 2019;82:706–720.

14. Feng X, Wang Z, Meyer CH. Real-time dynamic vocal tract imaging using an accelerated spiral GRE sequence and low rank plus sparse reconstruction. *Magn Reson Imaging*. 2021;80:106-112.

15. Cao Z, Gore JC, Grissom WA. Low-rank plus sparse compressed sensing for accelerated proton resonance frequency shift MR temperature imaging. *Magn Reson Med*. 2019;81(6):3555-3566.

16. Bauer RW, Radtke I, Block KT, Larson MC, Kerl JM, Hammerstingl R, Graf TG, Vogl TJ, Zhang S. True real-time cardiac MRI in free breathing without ECG synchronization using a novel sequence with radial k-space sampling and balanced SSFP contrast mode. *Int J Cardiovasc Imaging*. 2013;29:1059–1067.

17. Muthurangu V, Lurz P, Critchely J, Deanfield J, Taylor A, Hansen MS. Real-time assessment of right and left ventricular volumes and function in patients with congenital heart disease by using high spatiotemporal resolution radial k-t SENSE. *Radiology*. 2008;248:782–91.

18. Haji-Valizadeh H, Rahsepar AA, Collins JD, et al. Validation of highly accelerated real-time cardiac cine MRI with radial k-space sampling and compressed sensing in patients at 1.5T and 3T. *Magn Reson Med*. 2018;79:2745–2751.

19. Feng X, Salerno M, Kramer C M, Meyer CH. Non-Cartesian balanced steady-state free precession pulse sequences for real-time cardiac MRI. *Magn Reson Med*. 2016;75:1546-1555.

20. Nayak KS, Hargreaves BA, Hu BS, Nishimura DG, Pauly JM, Meyer CH. Spiral balanced steady-state free precession cardiac imaging. *Magn Reson Med*. 2005;53:1468–1473.

21. Steeden, J.A., Kowalik, G.T., Tann, O. et al. Real-time assessment of right and left ventricular volumes and function in children using high spatiotemporal resolution spiral bSSFP with compressed sensing. *J Cardiovasc Magn Reson.* 2018;20:1-11.

22. Wang Z, Feng X, Dou Q, Meyer CH. Accelerated Spiral imaging for Real-time Cardiac MRI. *Proc Intl Soc Magn Reson Med*. 2018; 26:0935.

23. Wang Z, Feng X, Yang Y, Zhou R, Salerno M, Meyer CH. High Resolution Real-time Spiral Cine with Whole Heart Coverage in Under 30 Seconds. *Proc Intl Soc Magn Reson Med*. 2019; 27:2124.

24. Meyer CH, Pauly JM, Macovski A, Nishimura DG. Simultaneous spatial and spectral selective excitation. *Magn Reson Med*. 1990;15:287–304.

25. Hargreaves BA, Vasanawala SS, Pauly JM, Nishimura DG. Characterization and reduction of the transient response in steady-state MR imaging. *Magn Reson Med*. 2001;46:149–158.

26. Meyer CH, Hu BS, Nishimura DG, Macovski A. Fast spiral coronary artery imaging. *Magn Reson Med*. 1992;28:202–213.

27. Wundrak S, Paul J, Ulrici J, Hell E, Geibel MA, Bernhardt P, Rottbauer W, Rasche V. Golden ratio sparse MRI using tiny golden angles. *Magn Reson Med*. 2016;75:2372–2378.

28. Chan RW, Ramsay EA, Cheung EY, Plewes DB. The influence of radial undersampling schemes on compressed sensing reconstruction in breast MRI. *Magn Reson Med*. 2012;67:363–377.

29. Aldefeld B, Bornert P. Effects of gradient anisotropy in MRI. *Magn Reson Med*. 1998;39:606–614.

30. Tan H, Meyer CH. Estimation of k-space trajectories in spiral MRI. *Magn Reson Med*. 2009;61:1396–1404.

31. Irarrazabal P, Meyer CH, Nishimura DG, Macovski A. Inhomogeneity correction using an estimated linear field map. *Magn Reson Med*. 1996;35:278–282.

32. Uecker M, Lai P, Murphy MJ, Virtue P, Elad M, Pauly JM, Vasanawala SS, Lustig M. ESPIRiT–an eigenvalue approach to auto-calibrating parallel MRI: where SENSE meets GRAPPA. *Magn Reson Med*. 2014;71:990–1001.

33. Wang Z, Bovik AC, Sheikh HR, Simoncelli EP. Image quality assessment: From error visibility to structural similarity. *IEEE Trans Image Proc*. 2004;13:600–612.

34. Fessler JA. On NUFFT-based gridding for non-Cartesian MRI. *J Magn Reson*. 2007;188:191–195.

35. Fessler JA. Michigan image reconstruction toolbox (MIRT). https://web.eecs.umich.edu/~fessler/code/index.html. Accessed September 15, 2018.

36. Lin C. Y. and Fessler J. A., Efficient dynamic parallel MRI reconstruction for the low-rank plus sparse model. *IEEE Trans Computational Imaging*. 2019;5:17-26.

37. Wissmann L, Santelli C, Segars WP, Kozerke S. MRXCAT: realistic numerical phantoms for cardiovascular magnetic resonance. *J Cardiovasc Magn Reson*. 2014;16:2–11.

38. Eirich P, Wech T, Heidenreich JF, et al. Cardiac real-time MRI using a pre-emphasized spiral acquisition based on the gradient system transfer function. *Magn Reson Med*. 2021;85: 2747-2760.

39. Liao J-R, Pauly JM, Brosnan TJ, Pelc NJ. Reduction of motion artifacts in cine MRI using variable-density spiral trajectories. *Magn Reson Med*. 1997;37:569–575.

40. Tsai CM, Nishimura DG. Reduced aliasing artifacts using variable density k-space sampling trajectories. *Magn Reson Med*. 2000;33:452–8.

Chapter 7: Conclusion

7.1 Summary

Rapid MRI is always an active research area as researchers seek to increase the effectiveness of MRI techniques, including efforts to reduce the scan time and to improve patient comfort. As stated in the introduction chapter of this dissertation, we aimed to explore techniques in rapid spiral imaging and applications for fast T_2-weighted imaging and real-time cardiac cine imaging. The work of this dissertation concentrates on novel pulse sequence design, trajectory design, as well as strategies of system imperfection correction and image reconstruction.

The main contributions of this dissertation are summarized as follows:

1. **Design and analysis of 2D TSE with annular spiral-rings and retraced in/out trajectories**. In Chapter 3, a thorough design of 2D TSE with the spiral-ring trajectory was developed and implemented for fast T_2-weighted brain imaging. Key properties of the spiral-rings with retraced in/out trajectories were investigated and compared to the previous annular spiral-ring technique, including T_2 decay effects, off-resonance modulation, trajectory infidelity, and scan/SNR efficiency. Simulation, phantom, and in vivo experiments were performed for validation.
2. **Compensation of B_0 inhomogeneity for 2D TSE with annular spiral-rings.** The retraced in/out design enables self-compensation for modest off-resonance effects from B_0 inhomogeneity. A complete correction of B_0 inhomogeneity was employed by using semi-automatic conjugate phase reconstruction with a maximum energy objective function. Experimental results showed that this approach performed well in most regions of brain, except some areas near air/tissue boundaries.

3. **Design and implementation of 3D TSE/SPACE with spiral-in/out trajectories.** In Chapter 5**,** 3D SPACE with prolonged spiral-in/out readouts was realized at 0.55 T for 1 mm^3 isotropic T_2-weighted brain images. The implementation includes RF series with redesigned variable-flip-angles, echo-reordering for a smooth signal pathway along the echo train direction, and PI/CS for accelerating data acquisition. Phantom and in vivo experiments were performed for validation.
4. **Compensation of concomitant fields for 2D/3D spiral TSE.** Chapter 4 proposed compensation principles which can be extended to correct for trajectories that are time-varying and asymmetric along the echo train in TSE-based imaging, while Chapter 5 depicted a special case for TSE with time symmetric spiral-in/out trajectories. Both of these chapters described the thorough analysis of concomitant field effects on 2D/3D TSE imaging, as well as the approaches of sequence modifications and image reconstruction to correct for the phase errors induced by concomitant fields along the echo train and during the readout.
5. **Design and optimization of accelerated spiral-out and spiral-in/out bSSFP cine sequences.** In Chapter 6, the feasibility of spiral-out and spiral-in/out bSSFP with high acceleration ratio was explored for real-time cardiac function MRI, and the comparison of spiral bSSFP cine against the standard Cartesian cine was performed in in vivo experiments. The results demonstrated that both spiral bSSFP sequences showed clinical acceptable images as well as the accuracy of cardiac function.

7.2 Potential future directions

7.2.1 Rapid and simultaneous acquisition of T_2-weighted and fluid-attenuated inversion recovery (FLAIR) images

T_2-weighted and FLAIR pulse sequences are standard protocols for neuroimaging because of the high sensitivity for many brain lesions. The combination of these two techniques further improves lesion conspicuity, such as for multiple sclerosis[1] and demyelination[2]. However, producing both of these image contrasts with high spatial resolution is time-consuming, typically taking 5-7 minutes, and sequential imaging may also be affected by motion artifacts and may require additional image registration for quantitative analysis.

In Chapter 3, we have demonstrated that SPRING-RIO TSE offers benefits of SNR efficiency and image contrast over the conventional Cartesian counterpart.[3] In this section, we seek to extend this idea to speed up acquisition time for combined T_2-weighted/FLAIR imaging by replacing the Cartesian sampling in FASCINATE[4] with a more efficient spiral-ring acquisition strategy. A simplified timing diagram of the pulse sequence is depicted in Figure 7-1. The boxes with stripes show slices for the T_2-weighted acquisition, while the open boxes show slices for the FLAIR acquisition. The time interval between boxes with the same number is set to TI. A 180°(y)-90°(x) RF pair is applied only at the end of the echo train for boxes with stripes to achieve driven inversion.

Preliminary fully-sampled in vivo images in Figure 7-2 show a comparison between Cartesian TSE and the T_2-weighted acquisition of the proposed method, and between Cartesian FLAIR and the FLAIR acquisition of the proposed method. The T_2-weighted images from the proposed method show good consistency with those from Cartesian TSE, in terms of image quality

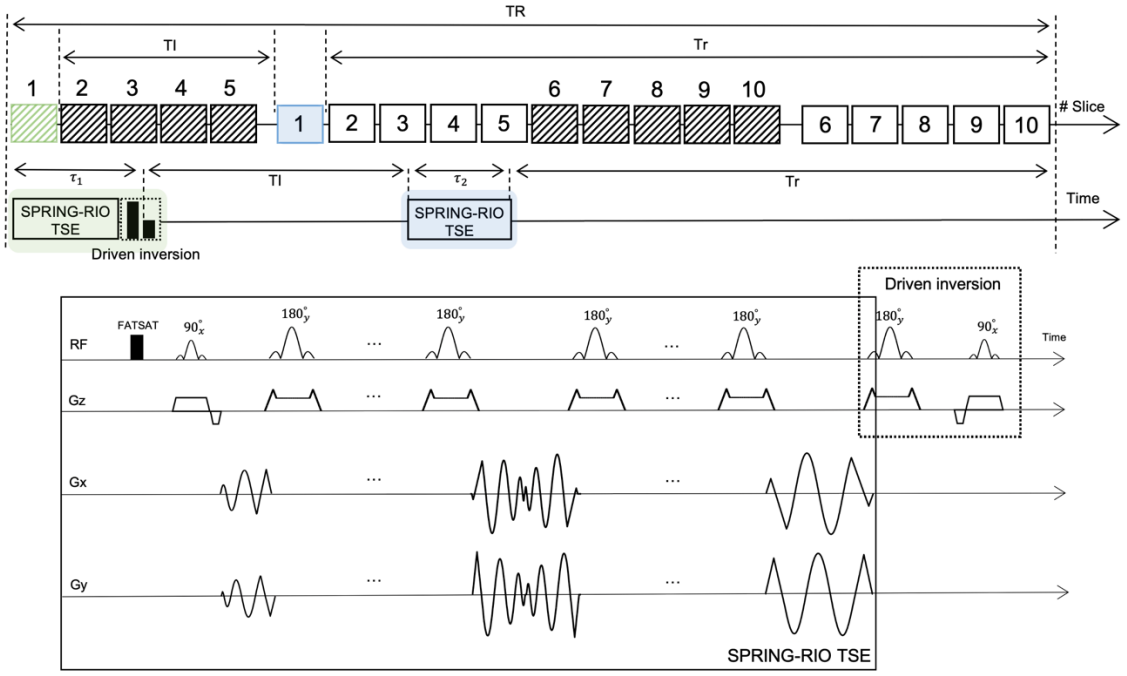

Figure 7-1. Pulse sequence diagram showing the sampling strategy, including the time-multiplexed multi-slice scheme, SPRING-RIO TSE data acquisition, and driven-inversion RF pulses.

and image contrast. The FLAIR images from both of these methods show good CSF suppression and similar image quality, although there is a slight difference in the WM/GM contrast, mainly due to somewhat different imaging parameters used for these two methods, such as the echo time. The total scan time is 1:10 min for Cartesian TSE, 3:55 min for Cartesian FLAIR, and 1:45 min for the proposed method. Overall, the results show that this method achieves T_2-weighted and FLAIR images at 0.7 x 0.7 x 4 mm^3 spatial resolution per slice in a single sequence with a 65% scan time reduction relative to sequential Cartesian acquisitions. Limitations includes:

1. It may fail to nullify the CSF and suffer from flow artifacts in some imaging regions of fast CSF flow, due to the use of a thin slice-selective pulses.
2. The effect of stimulated echoes during the acquisition windows is not considered in the signal model, and increasing the ETL and the use of a reduced refocusing flip angle may

Figure 7-2. Comparison of in vivo images acquired using standard Cartesian TSE for T_2-weighted images, Cartesian FLAIR for fluid-attenuated images, and the proposed method for both the T_2-weighted and fluid-attenuated images.

further increase the contribution of the stimulated echoes. Future work will focus on a more complex signal model and the optimization of scan parameters.

7.2.2 Distortion- and motion artifact-free single-shot diffusion imaging

Diffusion-weighted pulse sequences are routine MRI protocols for neurological and oncological imaging, including, but not limited to, acute stroke and tumors.[5,6] The combination of single-shot spin-echo acquisition and an EPI readout (~100 ms per slice) enables fast diffusion-weighted imaging with minimal motion artifacts. However, the long EPI readout duration presents

challenges for imperfections, such as B_0-inhomogenity induced geometric distortions and ghosting artifacts, thus limiting its use for some clinical applications (e.g., tumor delineation for radiation therapy). Multi-shot (MS) DW-EPI is a means to improve geometric fidelity[3], yet shot-to-shot phase inconsistency caused by physiological motion (e.g., cardiac pulsation) and system imperfections can lead to substantial signal dropouts and artifacts, which require additional motion information to suppress and cannot always be easily corrected by a phase-correction method.[7,8]

TSE acquisition[4] uses a series of refocusing RF pulses that split long sampling trajectories (e.g., a spiral readout) into small portions of k-space coverage to suppress effects of B_0-inhomogenity. However, incorporating diffusion gradients into a TSE acquisition is not straightforward because of the CPMG condition.[9] In this section, we seek to utilize a diffusion-prepared approach[10,11] combined with SPRING-RIO TSE imaging for single-shot diffusion imaging, as well as gradient stabilizers to correct for magnitude inconsistency associated with the preparation module.

A schematic of the SS-DP-SPRING TSE sequence is depicted in Figure 7-3. The diffusion-prepared (DP) module consists of Stejskal–Tanner monopolar diffusion gradients and one magnitude stabilizer (~4π dephasing) along the slice-select direction, followed by a 90 tip-up RF pulse that flips the diffusion-encoded signal back to the longitudinal axis. Large spoiler gradients (~2X larger than stabilizers) are added immediately after the diffusion-prepared module and before the following TSE acquisition. Rephasing and dephasing gradients are inserted before and after each echo during the spiral-ring readout to form the echo and distribute the magnetization, respectively. The added stabilizers offer the benefit of converting the magnitude-modulated signal loss into a phase-modulated problem[9], at the cost of 50% SNR loss. We further adopt a single-shot

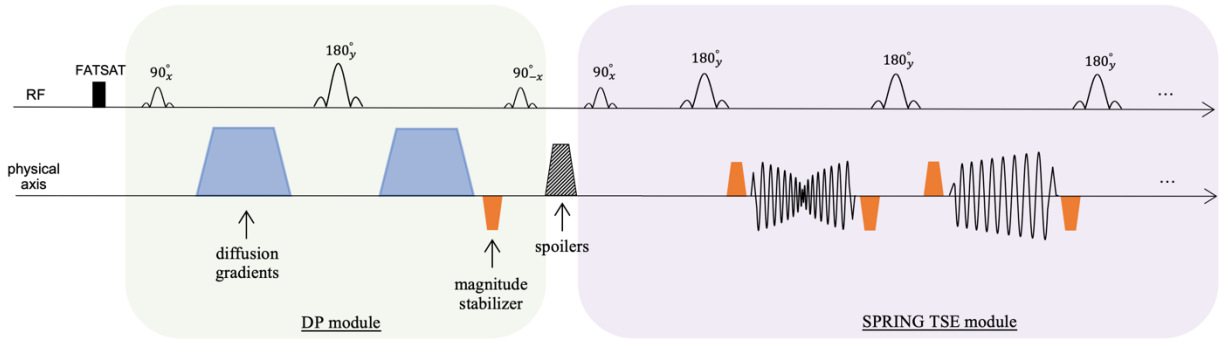

Figure 7-3. Sequence diagram of single-shot diffusion-prepared (DP) spiral-ring (SPRING) TSE with gradient stabilizers (blue trapezoids: diffusion gradients, orange trapezoids: magnitude stabilizers, striped trapezoids: spoiler gradients).

acquisition approach, so there is no need of additional phase correction which may not completely resolve phase inconsistencies among shots.

The central spiral-in-out ring is placed at the first echo of the TSE acquisition to obtain a short TE (~11 ms). Ten spiral-rings with linearly decreasing sampling density, from 1 to 0.2, are designed for 1.25 mm^2 isotropic in-plane resolution, with a total acquisition time of 110 ms. The duration of diffusion gradients is 12 ms with 71 mT/m amplitude for an estimated b-value of 750 s/mm^2, yielding a total duration of 35 ms for the DP module. The slice-thickness of the sinc RF pulses used in the DP module is 1.5X larger than that of the TSE acquisition to mitigate flow-related and cross-talk artifacts. To demonstrate the efficiency of stabilizers combined with the single-shot theme, we test SS-DP-SPRING TSE without stabilizers and with stabilizers and compared it to 2-shot DP-SPRING TSE with stabilizers. For image reconstruction, NUFFT[12] and L1-ESPIRiT[13] were performed on the undersampled datasets.

Figure 7-4 demonstrates the performance improvement for the proposed SS-DP-SPRING TSE with magnitude stabilizers (top) compared to that without stabilizers (middle) and for 2-shot DP-SPRING TSE with stabilizers (bottom). All images were reconstructed using NUFFT.

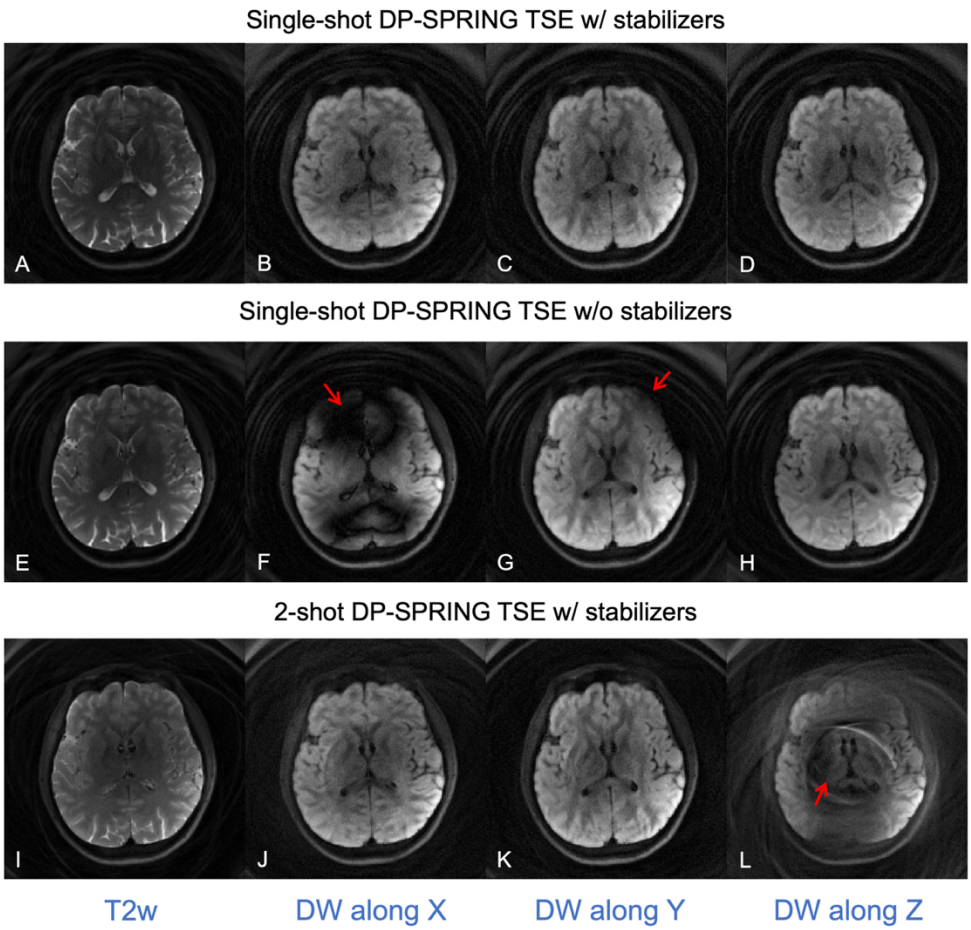

Figure 7-4. In vivo brain images showing the stability of image quality from the proposed single-shot DP-SRPING TSE sequence with magnitude stabilizers (A-D) over single-shot DP-SRPING TSE without stabilizers (E-H) and a 2-shot DP-SRPING TSE sequence with stabilizers (I-L). Note that all images were reconstructed via NUFFT, and images E-H have theoretical 2X SNR higher than other images. (NSA = 1).

Unpredictable severe bands of signal loss can be seen in Figure 7-4F-G from SS-DP-SPRING TSE without stabilizers when the diffusion gradient is on. When using a 2-shot acquisition, artifacts and signal cancellation are obvious as shown in Figure 7-4L, because of cardiac pulsation, when the diffusion gradient is along the head-foot direction. Image degradation attributed to magnitude or phase modulation is substantially reduced when applying magnitude stabilizers with the single-shot.

Figure 7-5 shows examples of estimated ADC maps along three main diffusion directions and the mean ADC values, acquired by SS-DP-SPRING TSE with magnitude stabilizers and L1-

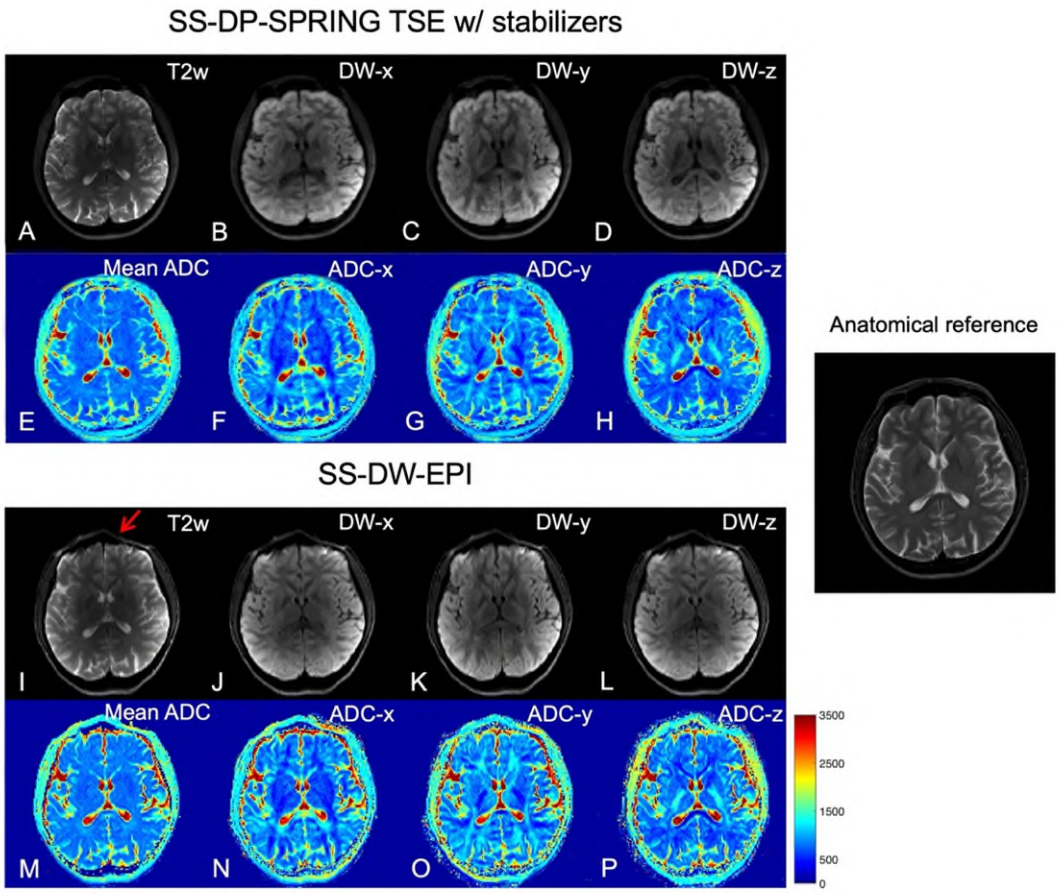

Figure 7-5. Example of single-shot in vivo results showing images at b-values of 0 (A, I) and 750 s/mm^2 (B-D, J-L), ADC maps for three main directions (F-H, N-P), and mean ADC maps (E, M), acquired from SS-DP-SPRING TSE with magnitude stabilizers (A-H) and SS-DW-EPI (I-P). The conventional T2w image on the right is considered the anatomical reference. Red arrow points to distortion and artifacts in SS-DW-EPI. (NSA = 4 for SS-DP-SPRING TSE, 2 for SS-DW-EPI.)

ESPIRiT reconstruction (top) and SS-DW-EPI (bottom). A T_2-weighted Cartesian TSE image is used for anatomical reference. The proposed method shows similar ADC maps compared to the SS-DW-EPI counterpart, while distortion and signal pile-up artifacts are clearly seen in EPI images (e.g., red arrow). Limitations include:

1. Some slices from SS-DP-SPRING TSE show residual image artifacts (not shown here), likely due to the system imperfections such as the slice profile of the slice-select tip-up/down and the refocusing RF pulses used in the DP module; future work is warranted to investigate this issue.

2. Resolution is relatively low; future work may explore approaches for increasing the spatial resolution in DW images.
3. Diffusion tensor imaging (e.g., fractional anisotropy map) will be performed in the future study for validation.

7.2.3 Spiral-in-out bSSFP real-time cine at 0.55 T low-field scanner

Chapter 2 has described that bSSFP is the standard sequence for assessing cardiac function because of its short acquisition time and high blood-myocardium contrast[14]. However, off-resonance phase accrual can produce undesirable banding artifacts in bSSFP, which limits the TR to 3 ~ 4 ms at 1.5 T and even shorter at 3 T. Cardiac MRI at low field has recently gained increasing interest[15-18], due to its more homogeneous B_0 field, which may extend the TR to 6 ~ 8 ms to improve sampling efficiency in bSSFP imaging. Therefore, low field offers great advantages for SNR-efficient acquisitions such as spiral and EPI trajectories with a longer readout in cardiac imaging[17,18].

As discussed in Chapter 6, we introduced and compared spiral-out and spiral-in/out bSSFP sequences[19,20] for accelerated real-time cardiac MRI at 1.5 T. The results demonstrated that a spiral-in/out bSSFP sequence combined with a L+S reconstruction[21] yields ungated cardiac movies with high image quality and minimal temporal blurring and can be an alternative to gated and breath-held CINE for the assessment of cardiac function. In this section, we seek to develop a spiral-in/out sequence with an extended TR to acquire real-time spiral cine at 0.55 T with high temporal resolution (~ 36 ms) and spatial resolution (~ 1.7 mm) within three seconds.

The sequence diagram shown in Figure 6-1 is used for data sampling. TR is set to 6 ms with a prolonged readout length of 4 ms. A total of 384 spiral arms per slice are collected using a tiny golden angle rotation (blue boxes), with six spiral-in/out readouts reconstructed for each

cardiac frame. All of the experiments were performed on a 0.55 T scanner (prototype MAGNETOM Area, Siemens Healthcare, Erlangen, Germany) with high gradient performance (maximum gradient amplitude = 45 mT/m, maximum slew rate = 200 T/m/s). Institutional review board approval and written informed consent were obtained for human studies. For each healthy volunteer, a midventricular short-axis view and a horizontal long-axis view were imaged under breath-held and free-breathing conditions. For each set of experiments, the spiral-in/out bSSFP cine and Cartesian cine were run consecutively at the same image plane.

Figure 7-6 shows systolic and diastolic frames from the free-breathing spiral-in/out bSSFP sequence combined with L+S (right), and from the standard breath-held Cartesian bSSFP cine sequence (left). The result demonstrates that even using longer TR in bSSFP imaging, B_0 inhomogeneity-induced artifacts, such as banding and blurring, are not evident at 0.55 T after good cardiac shimming. Limitations include:

1. The proposed method yields a relatively smooth transition between the end of systole and the end of diastole compared to the standard method.
2. Lengthening the TR to 6.5 ms or more may lead to an increase in pulsatile flow artifacts, especially in slices where the aortic pulsation is strong.
3. Visual assessment and quantitative functional measures such as LV ejection fraction are not performed, and no patient is recruited for clinical validation.

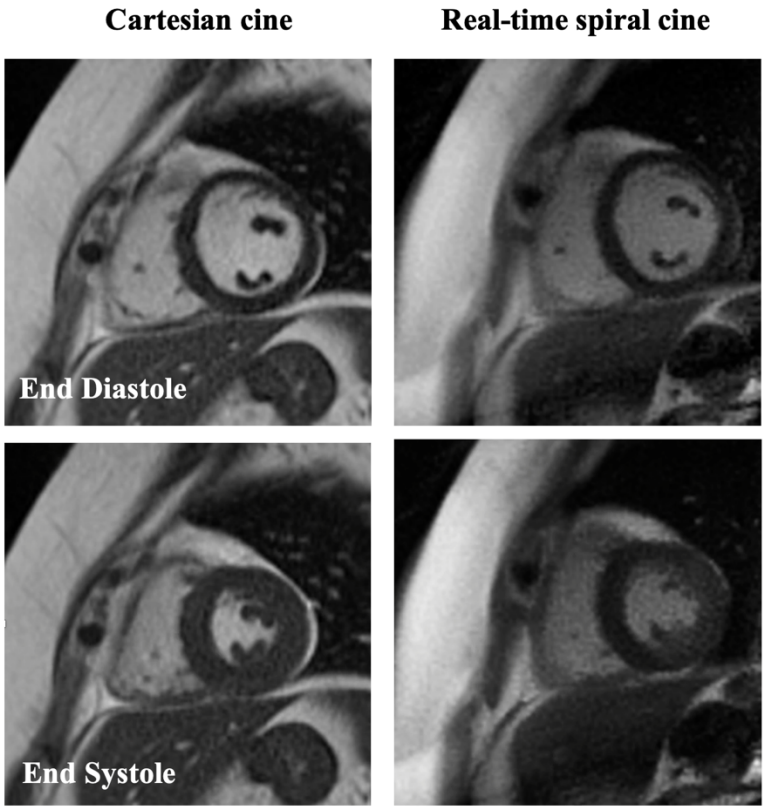

Figure 7-6. Single slice comparison from short-axis orientation between the real-time, free-breathing spiral CINE (right) and the standard breath-held CINE (left) are shown.

7.3 References

1. Wiggermann V, Hernández-Torres E, Traboulsee A, Li D.K.B, Rauscher A. FLAIR2: a combination of FLAIR and T2 for improved MS lesion detection. *AJNR Am J Neuroradiol*. 2016;37:259-65.

2. Haller S, Kovari E, Herrmann FR, Cuvinciuc V, Tomm AM, Zulian GB, Lovblad KO, Giannakopoulos P, Bouras C: Do brain T2/FLAIR white matter hyperintensities correspond to myelin loss in normal aging? A radiologic–neuropathologic correlation study. *Acta Neuropathol Commun*. 2013, 1:14.

3. Wang Z, Allen SP, Feng X, Mugler JP, Meyer CH. SPRING-RIO TSE: 2D T2-Weighted Turbo Spin-Echo Brain Imaging using SPiral RINGs with Retraced In/Out Trajectories. *Magn Reson Med*. 2022;88:601-616.

4. Kazuhiro Takeo, Akihiro Ishikawa, et al. FASCINATE: A Pulse Sequence for Simultaneous Acquisition of T2-Weighted and Fluid-Attenuated Images. *Magn Reson Med*. 51:205-211, 2004.

5. Lövblad KO, Laubach HJ, Baird AE, et al. Clinical experience with diffusion-weighted MR in patients with acute stroke. *AJNR Am J Neuroradiol*. 1998;19:1061–1066.

6. Tsien C, Cao Y, Chenevert T. Clinical applications for diffusion magnetic resonance imaging in radiotherapy. *Semin Radiat Oncol*. 2014;24:218–226.

7. Holdsworth SJ, Skare S, Newbould RD, Guzmann R, Blevins NH, Bammer R. Readout-segmented EPI for rapid high resolution diffusion imaging at 3T. *Eur J Radiol*. 2008;65:36–46.

8. Skare S, Andersson JL. On the effects of gating in diffusion imaging of the brain using single shot EPI. *Magn Reson Imaging*. 2001;19:1125–1128.

9. Alsop DC. Phase insensitive preparation of single-shot RARE: application to diffusion imaging in humans. *Magn Reson Med*. 1997;38:527–533.

10. Gao Y, Han F, Zhou Z, et al. Multishot diffusion-prepared magnitude-stabilized balanced steady-state free precession sequence for distortion-free diffusion imaging. *Magn Reson Med*. 2019;81:2374–2384.

11. Van AT, Cervantes B, Kooijman H, Karampinos DC. Analysis of phase error effects in multishot diffusion-prepared turbo spin echo imaging. *Quant Imaging Med Surg*. 2017;7(2):238-250.

12. Fessler JA. Michigan image reconstruction toolbox (MIRT). https://web.eecs.umich.edu/~fessler/code/index.html. Accessed September 15, 2018.

13. Uecker M, Lai P, Murphy MJ, Virtue P, Elad M, Pauly JM, Vasanawala SS, Lustig M. ESPIRiT–an eigenvalue approach to auto-calibrating parallel MRI: where SENSE meets GRAPPA. *Magn Reson Med*. 2014;71:990–1001.

14. Carr JC, Simonetti O, Bundy J, Li D, Pereles S, Finn JP. Cine MR angiography of the heart with segmented true fast imaging with steady- state precession. Radiology 2001;219:828–834.

15. Simonetti OP. Ahmad R. Low-Field Cardiac Magnetic Resonance Imaging: A Compelling Case for Cardiac Magnetic Resonance's Future. *Circulation*, Cardiovascular Imaging. 2017;10(6).

16. Rashid S, Han F, Gao Y, et al. Cardiac balanced steady-state free precession MRI at 0.35 T: a comparison study with 1.5 T. *Quant Imaging Med Surg*. 2018;8(7):627-636.

17. Campbell-Washburn, A.E. et al, Opportunities in interventional and diagnostic imaging using high-performance low field MRI. *Radiology*, 2019; 293: 384-393.

18. Restivo MC, Ramasawmy R, Bandettini WP, Herzka DA, Campbell-Washburn AE. Efficient spiral in-out and EPI balanced steady-state free precession cine imaging using a high-performance 0.55T MRI. *Magn Reson Med*. 2020;84:2364–2375.

19. Feng X, Salerno M, Kramer C M, Meyer CH. Non-Cartesian balanced steady-state free precession pulse sequences for real-time cardiac MRI. *Magn Reson Med*. 2016, 75(4):1546.

20. Wang Z, Feng X, Dou Q, Meyer CH. Accelerated Spiral imaging for Real-time Cardiac MRI. Proceedings 26th Annual Meeting ISMRM, Paris. 2018:0935.

21. Otazo R, Candes E, Sodickson DK. Low-rank plus sparse matrix decomposition for accelerated dynamic MRI with separation of background and dynamic components. *Magn Reson Med*. 2014. 73(3): 1125-1136.

Appendix - Vita of the Author

EDUCATION

M.S. Biomedical Engineering, *Zhejiang University* June 2017

B.S. Biomedical Engineering, *Yanshan University* July 2014

JOURNAL PUBLICATONS

1. **Wang Z,** Allen SP, Feng X, Mugler JP, Meyer CH. SPRING-RIO TSE: 2D T_2-Weighted Turbo Spin-Echo Brain Imaging using SPiral RINGs with Retraced In/Out Trajectories. *Magn Reson Med*. 2022;88:601-616.
2. **Wang Z,** Ramasawmy R, Feng X, Campbell-Washburn AE, Mugler JP, Meyer CH. Concomitant magnetic-field compensation for 2D spiral-ring turbo spin-echo imaging at 0.55T and 1.5T. *Magn Reson Med*. 2023;1-17.
3. **Wang Z**, Feng X, Salerno M, Kramer CM, Meyer CH. High spatiotemporal real-time cardiac MRI using accelerated spiral-out and spiral-in/out balanced steady-state free precession pulse sequences at 1.5T. *Magn Reson Mater Phy*. (Under review)
4. **Wang Z**, Ramasawmy R, Javed A, Mugler JP, Meyer CH, Campbell-Washburn AE. Variable-flip-angle 3D spiral-in-out TSE/SPACE using echo-reordering and concomitant gradient compensation at 0.55 T. In preparation (Target: *Magn Reson Med*).
5. Ramasawmy R**,** Mugler JP**, Wang Z**, Ahsan J, Herzka DA, Meyer CH, Campbell-Washburn AE. Concomitant field-Compensation of Spiral Turbo Spin-Echo for 0.55T MRI. *Magn Reson Mater Phy*. (Minor revision)
6. Wang J, Awad M, Zhou R, **Wang Z**, Wang X, Feng X, Yang Y, Meyer CH, Kramer CM, Salerno M. High-resolution Spiral Real-time Cardiac Cine Imaging with Deep Learning based Rapid Image Reconstruction and Quantification. *NMR in Biomedicine*. (Under review)
7. Feng X, **Wang Z**, Meyer CH. Real-time Dynamic vocal tract imaging using an accelerated spiral GRE sequence and low rank plus sparse reconstruction. *Magn Reson Imaging*. 2021;80:106-112.

CONFERENCE PROCEEDINGS

1. **Wang Z**, Ramasawmy R, Javed A, Mugler JP, Meyer CH, Campbell-Washburn AE. Variable-flip-angle 3D spiral-in-out TSE/SPACE using echo-reordering and concomitant gradient compensation at 0.55 T. In Proceedings of the 32nd Annual Meeting of ISMRM, Toronto, CA, 2023. (**Oral**)
2. **Wang Z**, Cao X, Qing K, Feng X, Mugler JP, Meyer CH. Distortion-free diffusion imaging using single-shot diffusion-prepared turbo-spin-echo sequence with spiral-ring readouts and magnitude stabilizers. In Proceedings of the 32nd Annual Meeting of ISMRM, Toronto, CA, 2023. (Poster)
3. **Wang Z**, Feng X, Ramasawmy R, Campbell-Washburn AE, Mugler JP, Meyer CH. Maxwell Field Compensation for 2D Spiral-Ring Turbo Spin-Echo Imaging at 0.55 T and 1.5 T. In Proceedings of the 31st Annual Meeting of ISMRM, London, UK, 2022.p.0319. (**Oral, Magna Cum Laude Merit Award**)
4. **Wang Z**, Feng X, Ramasawmy R, Campbell-Washburn AE, Mugler JP, Meyer CH. Concomitant Field Compensation for 2D Spiral-Ring Turbo Spin-Echo Imaging at 0.55 T & 1.5 T. ISMRM Workshop on: Low Field MRI, Online Virtual Workshop, 2022. (**Power Pitch**)

5. Dou Q, **Wang Z**, Feng X, Ramasawmy R, Mugler JP, Campbell-Washburn AE, Meyer CH. Low-field MRI denoising with a deep complex-valued convolutional neural network. ISMRM Workshop on: Low Field MRI, Online Virtual Workshop, 2022. (**Power Pitch**)
6. Dou Q, **Wang Z**, Feng X, Meyer CH. Automatic Off-Resonance Correction for Spiral Imaging with a Convolutional Neural Network. In Proceedings of the 31st Annual Meeting of ISMRM, London, UK, 2022.p.5022. (Poster)
7. Yan K, **Wang Z**, Dou Q, Chen S, Meyer CH. Applying advanced denoisers to enhance highly undersampled MRI reconstruction under plug-and-play ADMM framework. In Proceedings of the 31st Annual Meeting of ISMRM, London, UK, 2022.p.1163. (Poster)
8. **Wang Z**, Allen S, Feng X, Mugler JP, Meyer CH. SPRING-RIO TSE: 2D T_2-Weighted Turbo Spin-Echo Brain Imaging using SPiral RINGs with Retraced In/Out Trajectories. In Proceedings of the 29th Annual Meeting of ISMRM, Virtual Conference, 2021.p.0837. (**Oral, Magna Cum Laude Merit Award**)
9. **Wang Z**, Feng X, Mugler JP, Salerno M, Campbell-Washburn AE, Meyer CH. Spiral-in-out bSSFP Real-Time Cine on a High Performance 0.55T Scanner. In Proceedings of the 29th Annual Meeting of ISMRM, Virtual Conference, 2021.p.0504. (**Oral**)
10. **Wang Z**, Feng X, Mugler JP, Meyer CH. Rapid and Simultaneous Acquisition of T2-weighted and Fluid-attenuated Brain Images using a Spiral-ring Turbo Spin-echo Imaging. In Proceedings of the 29th Annual Meeting of ISMRM, Virtual Conference, 2021.p.1247. (Poster)
11. Dou Q, **Wang Z**, Feng X, Mugler JP, Meyer CH. Retrospective motion compensation for spiral brain imaging with a deep convolutional neural network. In Proceedings of the 29th Annual Meeting of ISMRM, Virtual Conference, 2021.p.1359. (Poster)
12. **Wang Z**, Allen S, Feng X, Mugler JP, Meyer CH. SPRING TSE: 2D T2-Weighted Brain Imaging using SPiral RING Turbo Spin-Echo. In Proceedings of the 28th Annual Meeting of ISMRM, Virtual Conference, 2020.p.3714. (Poster)
13. **Wang Z**, Feng X, Salerno M, Meyer CH. Accelerated Spiral Balanced Steady-State Free Precession Pulse Sequences for Real-Time Cardiac MRI. In Proceedings of the 23rd Annual Meeting of SCMR Scientific Sessions, Orlando, FL, USA, 2020. Abstract 751441. (Poster)
14. **Wang Z**, Feng X, Yang Y, Zhou R, Salerno M, Meyer CH. High Resolution Real-time Spiral Cine with Whole Heart Coverage in Under 30 Seconds. In Proceedings of the 27th Annual Meeting of ISMRM, Montreal, Quebec, Canada, 2019.p.2124. (Poster)
15. **Wang Z**, Cao X, Liao C, Ye H, He H, Zhong J. DP-TSE MRF: Rapid and Accurate T2 and ADC Quantification Using Diffusion-Prepared Turbo Spin-echo Magnetic Resonance Fingerprinting. In Proceedings of the 26th Annual Meeting of ISMRM, Paris, France, 2018.p.0215. (**Power Pitch, Summa Cum Laude Merit Award**)
16. **Wang Z**, Feng X, Dou Q, Meyer CH. Accelerated Spiral imaging for Real-time Cardiac MRI. In Proceedings of the 26th Annual Meeting of ISMRM, Paris, France, 2018.p.0935. (**Oral**)

INVENTION DISCLOSURES

1. **Z Wang,** X Feng, JP Mugler III, M Salerno, AE Campbell-Washburn, CH Meyer. Systems and Methods for Spiral-In-Out Low Field MRI Scans. U.S. Patent 17/733,970, November 3, 2022.
2. **Z Wang**, SP Allen, X Feng, JP Mugler III, CH Meyer. Methods and systems for spin-echo train imaging using spiral rings with retraced trajectories. U.S. Patent 17/732,181, November 24, 2022.

3. JP Mugler III, CH Meyer, AE Campbell-Washburn, R Ramasawmy, J Pfeuffer, **Z Wang**, X Feng. Methods and Systems for Maxwell Compensation for Spin-echo Train Imaging. U.S. Patent 17/732,155, November 10, 2022.
4. Q Dou, **Z Wang**, X Feng, JP Mugler III, CH Meyer. Motion compensation for MRI imaging. U.S. Patent 17/733,967, November 24, 2022.

HONORS & AWARDS

Summa Cum Laude Merit Awards	ISMRM 2018
Magna cum Laude Merit Awards	ISMRM 2021 and 2022
ISMRM Education Stipend	ISMRM 2018, 2019 and 2022
SCMR Travel Award	SCMR 2021